

Forschungszentrum Karlsruhe
Technik und Umwelt

Wissenschaftliche Berichte
FZKA 5663

Numerical Simulation of Unsteady MagnetoHydro- Dynamic Flows in Ducts

L. Leboucher

Institut für Angewandte Thermo- und Fluidodynamik
Projekt Kernfusion

Dezember 1995

FORSCHUNGSZENTRUM KARLSRUHE
Technik und Umwelt
Wissenschaftliche Berichte
FZKA 5663

Numerical Simulation of Unsteady MagnetoHydroDynamic Flows in Ducts

Laurent Leboucher

Institut für Angewandte Thermo- und Fluidodynamik

Forschungszentrum Karlsruhe GmbH, Karlsruhe
1995

**Als Manuskript gedruckt
Für diesen Bericht behalten wir uns alle Rechte vor**

**Forschungszentrum Karlsruhe GmbH
Postfach 3640, 76021 Karlsruhe**

ISSN 0947-8620

Abstract

In order to simulate the flow of liquid metal in blankets for the cooling of thermonuclear fusion reactors, a finite volume code has been developed at IATF/KfK. It is able to compute both velocity field and induced currents in ducts of rectangular cross section.

The full Navier-Stokes equation for incompressible fluids is solved, while the magnetic field is supposed to be constant, the induced magnetic field being neglected. The coupling between the velocity field and the induced current is expressed by the Lorentz force introduced in the Navier-Stokes equation. Most of the computation time consists of solving a Poisson equation for pressure and another Poisson equation for the electric potential. The marching in time is achieved by fractional step. This code is restricted by some numerical instabilities, and by the resolution of the boundary layers. It allows calculations only for very special electrical boundary conditions. It has also never been used for unsteady flow simulation.

In order to overcome these limitations, a numerical stability analysis of the MHD Navier-Stokes equation is developed, and a new finite difference scheme is proposed and successfully tested. Besides, the code is now able to calculate flows in ducts of arbitrary electrical conductivity. An integral treatment of the thin boundary layers perpendicular to the magnetic field is also described and allows to get rid of the resolution limits on the grid size in these layers. As a result, the new version of the code allows to simulate flows at higher Hartmann numbers without increasing the number of grid points, and an example of flow computation at Hartmann number 1000 is shown. Moreover, a scheme of second order in time is now available for unsteady flow simulation.

The code is used to calculate a special kind of unsteady flow in an electrically insulated duct. The instability is initiated by the shear created by a pair of copper strips in the middle of each wall perpendicular the magnetic field, the strips being oriented with the axis of the duct. Such a device has been proposed and studied analytically and numerically in two dimensions and also investigated experimentally. The instabilities do not arise only from the shear layers beside the copper strips but also from the side layers. The instability of the side layers is enhanced by the instability of the shear layers beside the strips and become dominant when the vortices growing from the strips to the side walls reach the side layers. Moreover the same simulation with all walls insulating show that the flow is unstable even without the copper strips. In that case, the instability needs a longer time to develop, but the flow becomes nevertheless very unstable.

The flow is almost 2-D. The small 3-D effects lie in a stretching of the vortices along the strips when one moves from the middle of the duct to the Hartmann walls. The velocity component parallel to the magnetic field remains one or two orders of magnitude smaller than the perturbation perpendicular to this field. It proves however to be antisymmetric with respect to the axis of the duct. It is also antisymmetric with respect to the plane in between the Hartmann walls.

Finally, some informations of practical interest for the use of the code are given.

Numerische Simulation von instationären MHD Strömungen in Kanälen

Zusammenfassung

Um die Strömung eines Flüssigmetalls zur Kühlung des Blankets eines Fusionsreaktors numerisch simulieren zu können, wurde vor einiger Zeit ein Rechenprogramm auf der Basis der Finiten-Volumen-Methode entwickelt. Dieses Programm berechnet sowohl das Geschwindigkeitsfeld als auch die induzierten elektrischen Ströme für Kanalgeometrien mit rechteckigem Querschnitt.

In diesem Rechenprogramm werden die vollständigen Navier-Stokes-Gleichungen gelöst, während das angelegte Magnetfeld als konstant angenommen wird und das induzierte Magnetfeld vernachlässigt wird. Die Kopplung zwischen Geschwindigkeitsfeld und induzierten Strömen wird durch die Lorentzkraft bewirkt, welche in den Navier-Stokes-Gleichungen auftritt. Die meiste Rechenzeit wird damit verbraucht, eine Poissongleichung für den Druck und eine weitere Poissongleichung für das elektrische Potential zu lösen. Die Integration über der Zeit wird mit einer 'Fractional time step'-Methode durchgeführt. Die Anwendbarkeit des Codes wird durch einige numerische Instabilitäten und die numerische Auflösbarkeit von Grenzschichten beschränkt. Es sind nur Rechnungen mit speziellen Randbedingungen für den elektrischen Strom erlaubt. Er wurde bisher nur für stationäre Rechnungen eingesetzt.

Um diese Einschränkungen zu überwinden, wurde eine Analyse der numerischen Stabilität der diskretisierten MHD-Navier-Stokes-Gleichungen durchgeführt und im Anschluß daran ein neues finites Differenzenverfahren vorgeschlagen und erfolgreich getestet. Außerdem ist die neue Version des Codes nunmehr in der Lage, Strömungen in Kanälen mit beliebiger elektrischer Leitfähigkeit der Wände zu berechnen. Eine integrale Modellierung der dünnen Grenzschichten senkrecht zum Magnetfeld ist ebenfalls beschrieben, damit befreit man sich von den Schranken bezüglich der Auflösbarkeit dieser Schichten. So ist man jetzt im Stande, Strömungen bei höherer Hartmannzahl zu berechnen, ohne die Anzahl der Maschenpunkte vergrößern zu müssen. Ein Rechenbeispiel für eine Strömungsberechnung für Hartmannzahl 1000 ist in diesem Bericht enthalten. Außerdem ist nun ein Zeitintegrationsverfahren der Fehlerordnung zwei für transiente Rechnungen verfügbar.

Das Programm wird dazu benützt, eine spezielle Art transienter Strömung in einem isolierten Kanal zu berechnen. Die physikalische Instabilität wird durch die Schubspannung verursacht, welche von einem Paar von Kupferstreifen ausgeht, welche mitten an der Wand senkrecht zum Magnetfeld angebracht sind und in Richtung der Kanalachse orientiert sind. Eine solche Vorrichtung war 1994 von L. Bühler vorgeschlagen und analytisch und numerisch in zwei Raumdimensionen und experimentell von F. Debray untersucht worden. Die Instabilitäten werden sowohl von den Scherschichten

bei den Kupferstreifen als auch von den Seitenschichten erzeugt. Die Instabilität der Seitenschichten wird durch die Instabilität der Scherschichten nahe der Streifen verstärkt und wird dominant, wenn die Wirbel, die an den Streifen entstehen, sich bis zu den Seitenschichten ausdehnen. Außerdem zeigt die Untersuchung, daß die entsprechende Strömung mit vollisolierten Wänden auch ohne Kupferstreifen instabil wird. In diesem Falle benötigt die Instabilität mehr Zeit, um sich auszubilden, dennoch, nach genügend langer Zeit wird die Strömung sehr instabil. Die Strömung ist fast zweidimensional. Die kleinen dreidimensionalen Effekte zeigen sich im Strecken der Wirbel längs der Streifen, wenn sich diese von der Kanalmitte zur Hartmannwand bewegen. Die Geschwindigkeitskomponente parallel zum Magnetfeld bleibt ein oder zwei Größenordnungen kleiner als die Störungen senkrecht dazu. Diese Geschwindigkeitskomponente erweist sich als antisymmetrisch zur Kanalachse. Sie ist auch antisymmetrisch zur Ebene zwischen den Hartmannwänden.

Zum Schluß werden noch einige Informationen und Hinweise zur Benützung des Rechenprogramms gegeben.

Contents

Nomenclature	08
1 — DESCRIPTION OF THE CODE	09
1.1— Algorithm of the code	11
1.2— Temporary velocity	12
1.3— Restrictions of the old version of the code	12
2 — NUMERICAL STABILITY ANALYSIS	15
2.1— Stability of MHD Navier-Stokes equation with Lorentz force $\mathbf{J} \times \mathbf{B}$ discretised on a staggered grid	17
2.2— Improved, stable scheme for the $\mathbf{J} \times \mathbf{B}$ Lorentz force	21
2.3— Accuracy of the scheme for the $\mathbf{J} \times \mathbf{B}$ Lorentz force	23
2.4— Example of computation with the different schemes	25
3 — ARBITRARY WALL CONDUCTIVITY & INTEGRAL TREATMENT OF THE HARTMANN LAYERS	29
3.1— Arbitrary conductivity of the walls	31
3.2— Integral treatment of the Hartmann layer	33
3.3— Boundary condition for the tangential component of the velocity	35
3.4— Boundary condition for the normal component of the velocity	39
3.5— Example of computation at Hartmann number = 1000	39
4 — UNSTABLE FLOW IN A DUCT WITH CONDUCTING STRIPS	43
4.1— Introduction	45
4.2— Flow between two infinite plates with a conducting strip	45
4.3— Slightly unstable flow in a duct with conducting strips	49
4.4— Strongly unstable flow in a duct with conducting strips	55
4.5— Unstable flow in a duct with all walls insulating	66
5 — PRACTICAL INFORMATIONS ON THE CODE	75
5.1— Summary of the code	77
5.2— Input parameters	79
5.3— Where to find & how to run the code	53
5.4— Restrictions of the new version of the code	80
References	81

Nomenclature

a	characteristic length, usually half width of the duct
a_r	aspect ratio = a /half width of electrically conducting strip
B_0	characteristic magnetic field
u_0	characteristic velocity of the fluid
μ	dynamic viscosity
ρ	mass density of the fluid
σ	electrical conductivity of the fluid

dimensionless quantities

Ha	Hartmann number	$Ha^2 = \sigma B_0^2 a^2 / \mu$
\mathbf{J}	electric current density	
\mathbf{n}	vector normal to the wall	
N	Interaction parameter	$N = \sigma B_0^2 a / (\rho u_0)$
Re	Reynolds number	$Re = Ha^2 / N$
\mathbf{U}	velocity vector	
v_x	velocity component in the x-direction. (idem for v_y & v_z)	
\mathbf{B}	magnetic field	
δ	Hartmann layer thickness	$\delta = Ha^{-1}$
Δx	grid spacing in the x-direction. (idem for Δy & Δz)	
Φ	electric potential	

subscripts

n	component normal to the wall
t	component tangential to the wall
w	value at the wall
\perp	components in the plane perpendicular to the magnetic field
HW	Hartmann wall
SW	side wall

superscripts

C	value off the Hartmann layer (in the <u>core</u>)
M	integral value across the Hartmann layer
temp	temporary velocity

1—DESCRIPTION OF THE CODE

1.1—Algorithm of the code

The code is based on a 3-D finite volume discretisation, equally spaced on an orthogonal grid. Both pressure and electric potential are located at the centre of each cell, while the velocity and current density are positioned at the centre of the cell interfaces. In the same way, scalar quantities such as the divergence of vectors are calculated at cell centres, and the vector quantities such as the gradient of scalar quantities are computed on cell interfaces.

Central second order differences are used for all terms with the exception of the advective term $(\mathbf{U} \cdot \nabla) \mathbf{U}$ for which the LECUSSO-C upwind scheme (C. Günther 1992) is used if the mesh Reynolds number exceeds the value of 2. In the new version of the code, this upwind scheme is used in any case where it can be applied. Only at the grid point next to the wall and only when the fluid comes from that wall, the central difference scheme is used for the velocity component normal to the wall, for any mesh Reynolds number. In this case, it is not possible to use a second order upwind scheme which requires 2 points in the upwind direction. Although no first order upwind scheme has been introduced, no numerical instability has been detected at the boundaries.

The magnetic field is known and remains the same during the calculation since the induced field is neglected. The electric potential is computed as the solution of the Poisson equation whose right hand side is known from the velocity at the old time step n

$$\nabla^2 \Phi^n = \nabla \cdot (\mathbf{U}^n \times \mathbf{B}). \quad (1.1)$$

The electric current density can then be directly calculated as

$$\mathbf{J}^n = -\nabla \Phi^n + \mathbf{U}^n \times \mathbf{B}. \quad (1.2)$$

All other terms are evaluated explicitly, with the exception of the pressure. The time dependence of the solution via the so called 'fractional step' method as summarised by the following 3 equations.

First consider the Navier-Stokes equation

$$\frac{1}{N} \left[\frac{\mathbf{U}^{n+1} - \mathbf{U}^n}{\Delta t} + (\mathbf{U}^n \cdot \nabla^*) \mathbf{U}^n \right] = -\nabla^* P + \mathbf{J}^n \times \mathbf{B} + \frac{1}{\text{Ha}^2} \nabla^{*2} \mathbf{U}^n. \quad (1.3)$$

Second, take the divergence of this equation in order to get a Poisson-type equation which can be solved for pressure since its right hand side is known explicitly from the old time step n

$$\nabla^{*2} P = \nabla^* \cdot \left(-\frac{1}{N} (\mathbf{U}^n \cdot \nabla^*) \mathbf{U}^n + \mathbf{J}^n \times \mathbf{B} + \frac{1}{\text{Ha}^2} \nabla^{*2} \mathbf{U}^n \right) \quad (1.4)$$

Third, the velocity at the next time step $n+1$ is then

$$\mathbf{U}^{n+1} = \mathbf{U}^n + N\Delta t \left(-\frac{1}{N} (\mathbf{U}^n \cdot \nabla^*) \mathbf{U}^n - \nabla^* P + \mathbf{J}^n \times \mathbf{B} + \frac{1}{\text{Ha}^2} \nabla^{*2} \mathbf{U}^n \right) \quad (1.5)$$

1.2—Temporary velocity

The literature and the code itself refer to a so called temporary velocity as soon as the fractional step method is used. It is defined as the following

$$\frac{1}{N} \left[\frac{\mathbf{U}^{\text{temp}} - \mathbf{U}^n}{\Delta t} + (\mathbf{U}^n \cdot \nabla^*) \mathbf{U}^n \right] = \mathbf{J}^n \times \mathbf{B} + \frac{1}{\text{Ha}^2} \nabla^{*2} \mathbf{U}^n. \quad (1.6)$$

It's a kind of fictive velocity since it omits the contribution of the pressure gradient to the momentum equation. Then equations (1.4) & (1.5) can be rewritten

$$\nabla^{*2} P = \frac{1}{N\Delta t} \nabla^* \cdot \mathbf{U}^{\text{temp}}, \quad (1.7)$$

$$\mathbf{U}^{n+1} = \mathbf{U}^{\text{temp}} - N\Delta t \nabla^* P. \quad (1.8)$$

Note that the incompressibility is automatically satisfied by this fractional step method:

$$\nabla^* \cdot \mathbf{U}^{n+1} = -N\Delta t \nabla \cdot \nabla P + \nabla^* \cdot \mathbf{U}^{\text{temp}} = 0 \quad (1.9)$$

Furthermore the finite volumes ensures that the discretised form of the continuity equation is a good approximation of its continuous form.

A clear analysis of the fractional step method and its required boundary conditions is available in the journal of computational physics (J.Blair Perot, 92)

1.3—Restrictions of the old version of the code

- The code suffers from two kinds of numerical instabilities:

1) *Time dependant instabilities*: these oscillations give rise to an overflow if the time step is not much smaller than the theoretical diffusion limit for numerical stability $\Delta t \leq 1/2 \text{Re} / (\Delta x^{-2} + \Delta y^{-2} + \Delta z^{-2})$. Much smaller means about 10 to 50 times smaller for typical calculations found in the thesis report (L. Lenhart, 1994).

2) *Spatial oscillations*: they do not give any overflow but some strong unphysical oscillations at the corners of the duct in case of perfectly electrically conducting walls. For an equal grid spacing in both directions perpendicular to the flow, they appear as soon as the Hartmann layer is not resolved. The following chapter will show that this is pure coincidence and that these instabilities have nothing to do with the resolution of the Hartmann layers.

- The electrical boundary conditions are limited to two ideal cases: perfectly conducting walls (Dirichlet condition on Φ), or perfectly insulating walls (Neumann condition on Φ). Therefore, flows in real ducts without insulating coating cannot be modeled.

- The lack of resolution of the thin Hartmann layers gives wrong quantitative results even at low Hartmann numbers. The figures 1.1 and 1.2 shows how much the calculated pressure drop changes with the resolution for insulating and conducting walls.

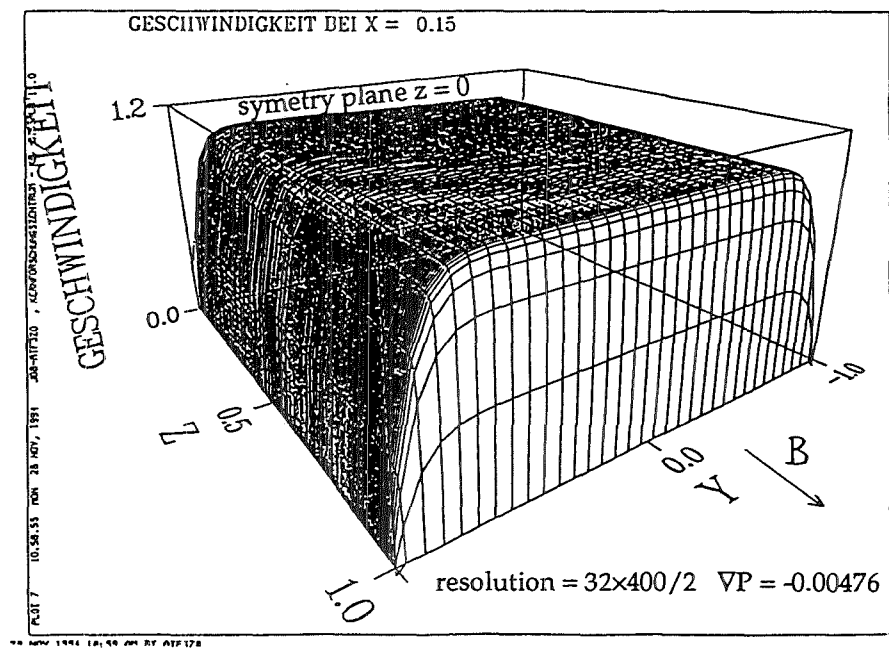
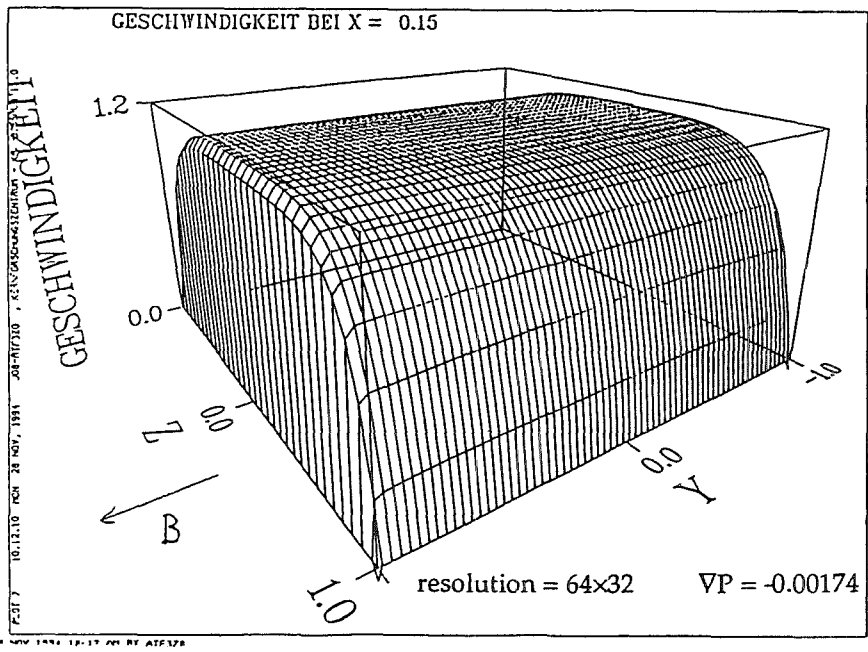
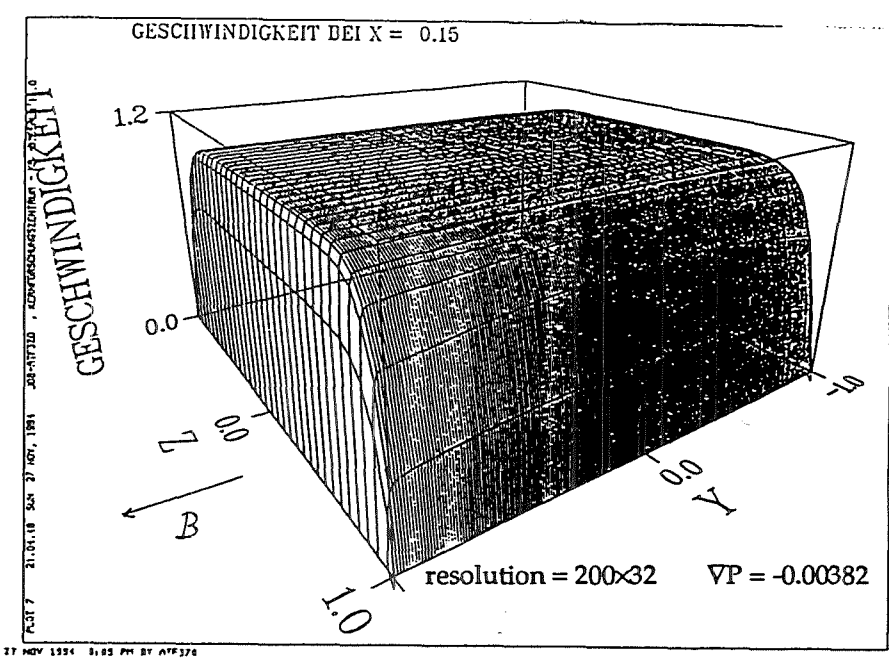
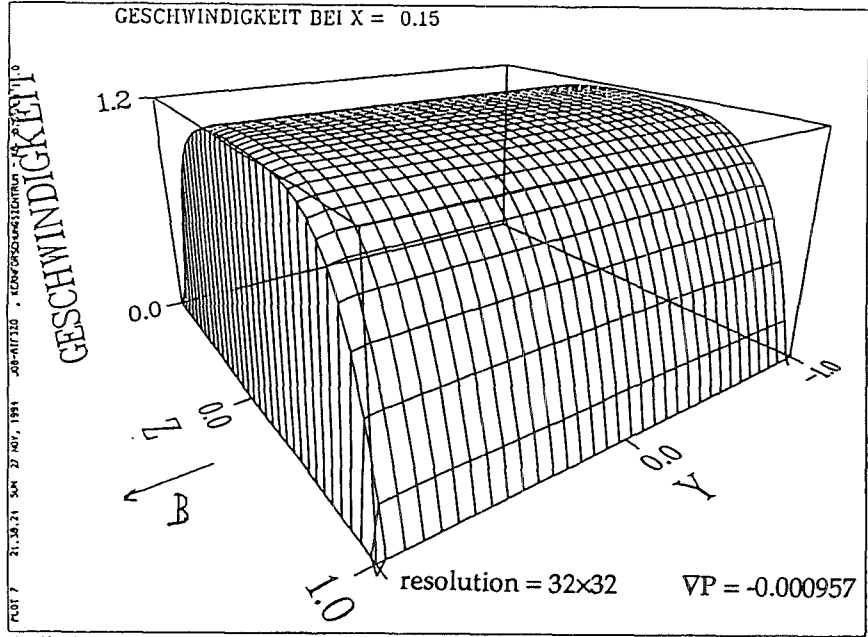


Fig 1.1: calculated pressure drop for different resolutions and insulating walls.
 $Ha = 200$. $VP = -0.00468$ from analytic solution.

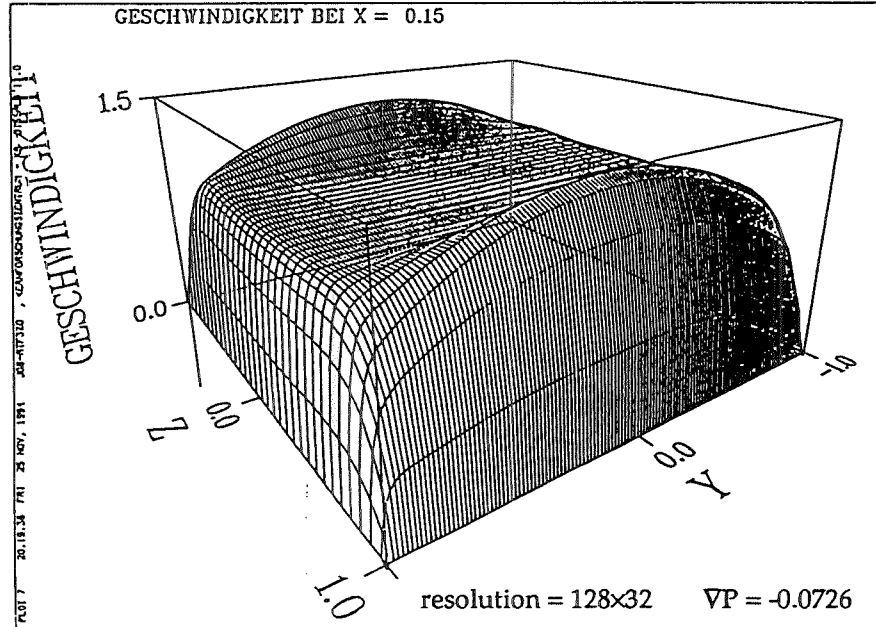
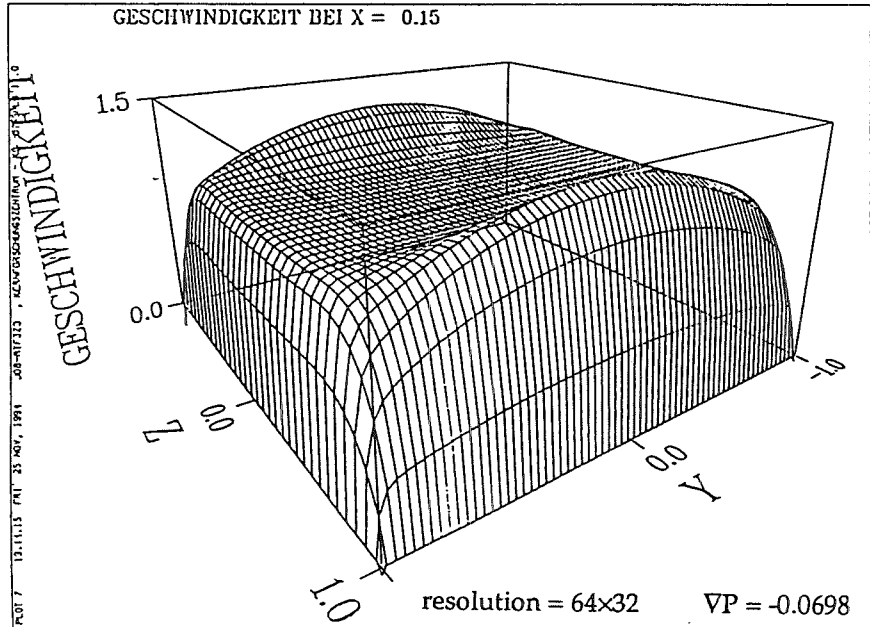
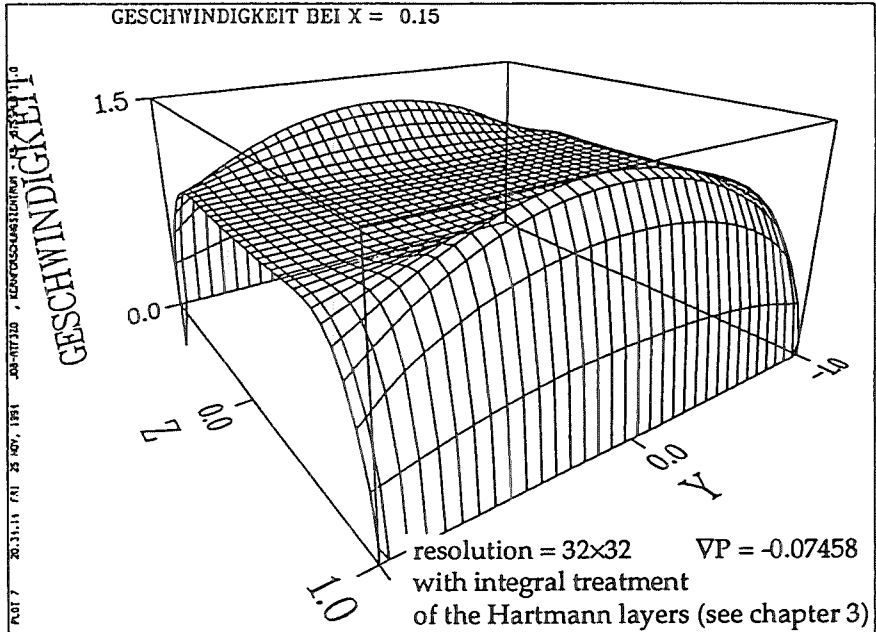
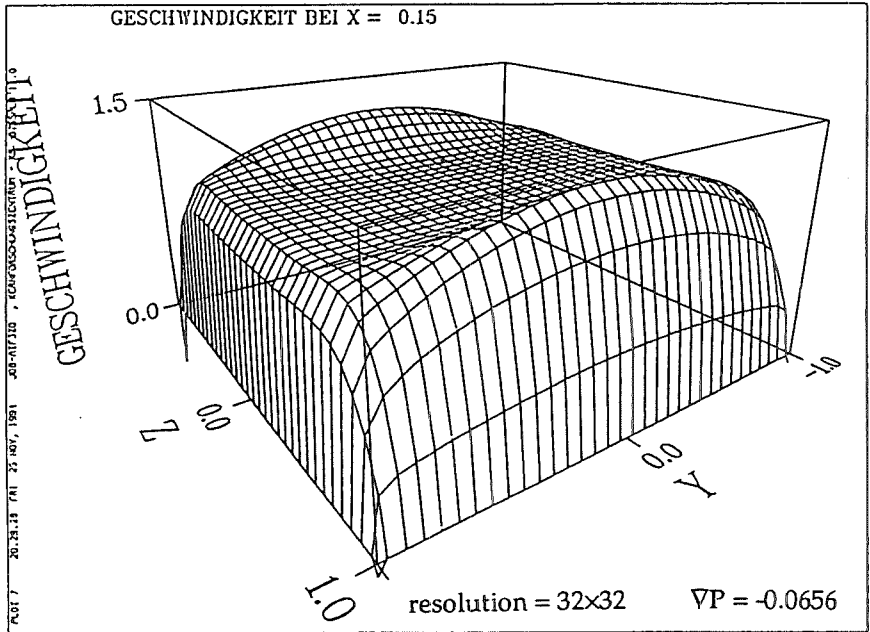


Fig 1.2: calculated pressure drop for different resolutions and conducting walls (see chap 3) : $c = 0.05$, $Ha = 50$.

2—NUMERICAL STABILITY ANALYSIS

2.1—Stability of MHD Navier-Stokes equation with Lorentz force $\mathbf{J} \times \mathbf{B}$ discretised on a staggered grid

The case of central differences and transverse magnetic field in the y-direction $\mathbf{B} = B_y$ is analysed. For simplicity, the magnetic field is supposed to vary only slightly within the scale of a grid cell, so that its value is B_y for all neighbouring points of the central point (i, j, k) .

In case where B_y is constant in the whole domain, its value should be 1 so that the dimensionless quantities Ha and N defined in the code are really significant. For shorter notations, the 3 components v_x, v_y, v_z of the velocity \mathbf{U} are written just like in the code itself, the 1/2 indices being dropped:

$$\begin{aligned} v_{x_{i+1/2}, j, k} &\rightarrow v_{x_{i, j, k}} \\ v_{y_{i, j+1/2}, k} &\rightarrow v_{y_{i, j, k}} \\ v_{z_{i, j, k+1/2}} &\rightarrow v_{z_{i, j, k}} \end{aligned}$$

The expression of the x-component of the temporary velocity as defined by the equation $\mathbf{U}^{\text{new}} = \mathbf{U}^{\text{temp}} - N \Delta t \nabla P$ is:

$$\begin{aligned} v_{x_{i, j, k}}^{\text{temp}} &= v_{x_{i, j, k}} \\ &+ \Delta t \{ \\ &- \frac{1}{4\Delta x} [(v_{x_{i+1}, j, k} + v_{x_{i, j, k}}) (v_{x_{i+1}, j, k} + v_{x_{i, j, k}}) \\ &\quad - (v_{x_{i, j, k}} + v_{x_{i-1}, j, k}) (v_{x_{i, j, k}} + v_{x_{i-1}, j, k})] \\ &- \frac{1}{4\Delta y} [(v_{y_{i+1}, j, k} + v_{y_{i, j, k}}) (v_{x_{i, j+1}, k} + v_{x_{i, j, k}}) \\ &\quad - (v_{y_{i+1}, j-1, k} + v_{y_{i, j-1, k}}) (v_{x_{i, j, k}} + v_{x_{i, j-1, k}})] \\ &- \frac{1}{4\Delta z} [(v_{z_{i+1}, j, k} + v_{z_{i, j, k}}) (v_{x_{i, j, k+1}} + v_{x_{i, j, k}}) \\ &\quad - (v_{z_{i+1}, j, k-1} + v_{z_{i, j, k-1}}) (v_{x_{i, j, k}} + v_{x_{i, j, k-1}})] \\ &+ N \{ \\ &- \frac{B_y}{4} (j_{z_{i+1}, j, k} + j_{z_{i+1}, j, k-1} + j_{z_{i, j, k}} + j_{z_{i, j, k-1}}) \\ &+ \frac{1}{Ha^2} \{ \\ &+ \frac{1}{\Delta x^2} (v_{x_{i+1}, j, k} + v_{x_{i-1}, j, k}) \\ &+ \frac{1}{\Delta y^2} (v_{x_{i, j+1}, k} + v_{x_{i, j-1}, k}) \\ &+ \frac{1}{\Delta z^2} (v_{x_{i, j, k+1}} + v_{x_{i, j, k-1}}) \\ &- 2 \left(\frac{1}{\Delta x^2} + \frac{1}{\Delta y^2} + \frac{1}{\Delta z^2} \right) v_{x_{i, j, k}} \\ &\} \} \} \end{aligned}$$

The current density is defined by Ohm's law:

$$\mathbf{J} = -\nabla \Phi + \mathbf{U} \times \mathbf{B}.$$

Due to the staggered grid, the cross product of two vectors has to be calculated as an average of several neighbouring vectors since \mathbf{U} , \mathbf{B} and $\mathbf{U} \times \mathbf{B}$ have different direction and are defined on different points.

Let us first consider the $\mathbf{U} \times \mathbf{B}$ term only which contains explicitly the velocity. Then the z-component of $\mathbf{U} \times \mathbf{B}$ for 4 positions appearing below is:

$$\begin{aligned} (\mathbf{U} \times \mathbf{B})_{z i, j, k} &= -\frac{By}{4} (vx_{i, j, k+1} + vx_{i-1, j, k+1} + vx_{i, j, k} + vx_{i-1, j, k}) \\ (\mathbf{U} \times \mathbf{B})_{z i+1, j, k} &= -\frac{By}{4} (vx_{i+1, j, k+1} + vx_{i, j, k+1} + vx_{i+1, j, k} + vx_{i, j, k}) \\ (\mathbf{U} \times \mathbf{B})_{z i+1, j, k-1} &= -\frac{By}{4} (vx_{i+1, j, k} + vx_{i, j, k} + vx_{i+1, j, k-1} + vx_{i, j, k-1}) \\ (\mathbf{U} \times \mathbf{B})_{z i, j, k-1} &= -\frac{By}{4} (vx_{i, j, k} + vx_{i-1, j, k} + vx_{i, j, k-1} + vx_{i-1, j, k-1}). \end{aligned}$$

Then the x-component of the Lorentz force due to $\mathbf{U} \times \mathbf{B}$, $[(\mathbf{U} \times \mathbf{B}) \times \mathbf{B}]_x$ is:

$$\begin{aligned} [(\mathbf{U} \times \mathbf{B}) \times \mathbf{B}]_{x i, j, k} &= -\frac{By}{4} [(\mathbf{U} \times \mathbf{B})_{z i+1, j, k} + (\mathbf{U} \times \mathbf{B})_{z i+1, j, k-1} \\ &\quad + (\mathbf{U} \times \mathbf{B})_{z i, j, k} + (\mathbf{U} \times \mathbf{B})_{z i, j, k-1}] \\ &= -\frac{By}{4} \frac{By}{4} (4 vx_{i, j, k} + 2 vx_{i+1, j, k} + 2 vx_{i-1, j, k} + 2 vx_{i, j, k+1} + 2 vx_{i, j, k-1} \\ &\quad + vx_{i+1, j, k+1} + vx_{i+1, j, k-1} + vx_{i-1, j, k+1} + vx_{i-1, j, k-1}). \end{aligned}$$

Suppose that $v_y = v_z = 0$ (fully developed flow). The temporary velocity can then be expressed explicitly in terms of the old velocity field in the neighbouring of the central point (i, j, k) , the $\nabla \Phi \times \mathbf{B}$ term being omitted:

$$\begin{aligned} vx_{i, j, k}^{\text{temp}} &= \\ vx_{i, j, k} &\left(1 - \frac{\Delta t}{4 \Delta x} vx_{i+1, j, k} + \frac{\Delta t}{4 \Delta x} vx_{i-1, j, k} - \Delta t N \frac{By^2}{4} - 2 \frac{\Delta t N}{Ha^2} (\Delta x^2 + \Delta y^2 + \Delta z^2) \right) 1^{\text{st}} \\ &+ vx_{i+1, j, k} \left(-\frac{\Delta t}{4 \Delta x} vx_{i+1, j, k} - \frac{\Delta t}{4 \Delta x} vx_{i, j, k} - \Delta t N \frac{By^2}{8} + \frac{\Delta t N}{\Delta x^2 Ha^2} \right) 2^{\text{nd}} \\ &+ vx_{i-1, j, k} \left(+\frac{\Delta t}{4 \Delta x} vx_{i, j, k} + \frac{\Delta t}{4 \Delta x} vx_{i-1, j, k} - \Delta t N \frac{By^2}{8} + \frac{\Delta t N}{\Delta x^2 Ha^2} \right) 3^{\text{rd}} \\ &+ vx_{i, j+1, k} \left(\frac{\Delta t N}{\Delta y^2 Ha^2} \right) + vx_{i, j-1, k} \left(\frac{\Delta t N}{\Delta y^2 Ha^2} \right) 4^{\text{th}} \& 5^{\text{th}} \\ &+ vx_{i, j, k+1} \left(-\Delta t N \frac{By^2}{8} + \frac{\Delta t N}{\Delta z^2 Ha^2} \right) 6^{\text{th}} \\ &+ vx_{i, j, k-1} \left(-\Delta t N \frac{By^2}{8} + \frac{\Delta t N}{\Delta z^2 Ha^2} \right) 7^{\text{th}} \end{aligned}$$

$$+ vx_{i+1,j,k+1} \left(-\Delta t N \frac{By^2}{16} \right) + vx_{i+1,j,k-1} \left(-\Delta t N \frac{By^2}{16} \right) \quad 8^{th} \& 9^{th}$$

$$+ vx_{i-1,j,k+1} \left(-\Delta t N \frac{By^2}{16} \right) + vx_{i-1,j,k-1} \left(-\Delta t N \frac{By^2}{16} \right) \quad 10^{th} \& 11^{th}$$

This scheme involves 10 neighbouring points around the point (i, j, k) and is stable if all coefficients are positive (C. Günther, 1994), except the diagonal points $(i+1, j, k+1)$, $(i+1, j, k-1)$, $(i-1, j, k+1)$, $(i-1, j, k-1)$ whose coefficient may be negative to some extent (see below).

1) *The diffusion limit for the time step comes out of the 1st coefficient*

$$\left(1 - \frac{\Delta t}{4 \Delta x} vx_{i+1,j,k} + \frac{\Delta t}{4 \Delta x} vx_{i-1,j,k} - \Delta t N \frac{By^2}{4} - 2 \frac{\Delta t N}{Ha^2} (\Delta x^2 + \Delta y^2 + \Delta z^2) \right) \geq 0.$$

Suppose that $vx_{i+1,j,k}$ and $vx_{i-1,j,k}$ are of the same order of magnitude, then they cancel out and the condition simplifies to

$$1 - \Delta t N \frac{By^2}{4} - 2 \frac{\Delta t N}{Ha^2} (\Delta x^2 + \Delta y^2 + \Delta z^2) \geq 0,$$

which is just the usual time step criteria for a convection diffusion problem, but it is now modified by the 2nd term due to 1/4 of the Lorentz force in the x-direction. This term gives a stronger limit for the maximum time step allowed for stable computation, especially at high Hartmann numbers:

$$\Delta t \leq \frac{Re}{2 (\Delta x^2 + \Delta y^2 + \Delta z^2) + \frac{Ha^2 By^2}{4}}, \quad \text{where } Re = \frac{Ha^2}{N}.$$

2) *The mesh-Reynolds number limit comes out of the 2nd and 3rd coefficients*

$$\left(-\frac{\Delta t}{4 \Delta x} vx_{i+1,j,k} - \frac{\Delta t}{4 \Delta x} vx_{i,j,k} - \Delta t N \frac{By^2}{8} + \frac{\Delta t N}{\Delta x^2 Ha^2} \right) \geq 0.$$

Suppose again that $vx_{i+1,j,k} \approx vx_{i,j,k} = vx$, then

$$-\frac{\Delta t}{2 \Delta x} vx - \Delta t N \frac{By^2}{8} + \frac{\Delta t}{\Delta x^2 Re} \geq 0.$$

Due to the electromagnetic term, the mesh-Reynolds number $Re \, vx \, \Delta x$ is then limited to a lower value than 2

$$Re \, vx \, \Delta x \leq \frac{2}{1 + By^2 \frac{N \Delta x}{4 vx}}.$$

This condition can be rewritten in terms of a limitation to the grid spacing in the flow direction:

$$\Delta x \leq -\frac{2 v_x}{N B y^2} + \sqrt{\left(\frac{2 v_x}{N B y^2}\right)^2 + \frac{8}{Ha^2 B y^2}} \stackrel{\text{if } v_x \geq 0}{\leq} \frac{\sqrt{8}}{Ha |B y|}.$$

3) *An additional limitation which has no equivalent in computation of ordinary fluid dynamics has to be considered and is due to the 6th and 7th coefficients.*

$$\left(-\Delta t N \frac{B y^2}{8} + \frac{\Delta t N}{\Delta z^2 Ha^2}\right) \geq 0.$$

This limitation is independent of the time step and the mesh-Reynolds number and is responsible for strong spatial oscillation (but no overflow) near the four corners of a square duct for flows at high Hartmann numbers. It implies a restriction to the grid spacing in the direction perpendicular to both magnetic field and flow direction:

$$\Delta z \leq \frac{\sqrt{8}}{Ha |B y|}.$$

For example, if one uses a 32×32 grid in the cross section of the duct of half width $a = 1$, and a normalised magnetic field $B y = 1$, then the maximum Hartmann number that can be reached without oscillation is:

$$Ha = \sqrt{8} / (\Delta z B y) = \sqrt{8} / (2/32 \times 1) = 45.$$

This analyse does not take into account the effect of the electric potential gradient on the Lorentz force since it does not contain explicitly the velocity. In fact, this term is coupled to the velocity field via the Poisson-type equation on electric potential $\nabla^2 \Phi = \nabla \cdot (\mathbf{U} \times \mathbf{B})$. But the gradient of potential usually counterbalances the $\mathbf{U} \times \mathbf{B}$ part of the current and therefore reduces the total current density \mathbf{J} as well as the Lorentz force itself. This could explain why no oscillations appear for computation at Hartmann number higher than 45 in case of perfectly insulating walls where the potential gradient is maximum. But as soon as the walls are electrically conducting, the oscillations occur and become stronger as the wall conductivity increases. The oscillations are maximum for perfectly conducting walls in which case the Hartmann number cannot be more than 50 for the above parameters. This is actually the highest value chosen for which L. Lenhart could find good results for MHD flow in perfectly conducting ducts (L. Lenhart pp 64-72).

4) *Finally the last 4 coefficients which are negative in any case should not be larger in absolute value than the product of the coefficients of the neighbouring points, e.g. the 8th coefficient should be less in absolute value than the product of the 2nd and 6th coefficients:*

$$\left| -\Delta t N \frac{B y^2}{16} \right| \leq \left(-\frac{\Delta t}{2 \Delta x} v_x - \Delta t N \frac{B y^2}{8} + \frac{\Delta t N}{\Delta x^2 Ha^2} \right) \left(-\Delta t N \frac{B y^2}{8} + \frac{\Delta t N}{\Delta z^2 Ha^2} \right)$$

This relation can be satisfied if one chooses the largest value allowed for Δz , i.e. $\sqrt{8} / (Ha By)$ in which case the 6th coefficient is zero.

2.2—Improved, stable scheme for the $\mathbf{J} \times \mathbf{B}$ Lorentz force

As a conclusion to the previous section, the MHD numerical oscillations are due to the distribution of the weight of the Lorentz force on several neighbouring grid points. These oscillations can be suppressed if a new scheme is chosen for this electromagnetic force.

The Lorentz force can be written:

$$\mathbf{J} \times \mathbf{B} = (-\nabla \Phi + \mathbf{U} \times \mathbf{B}) \times \mathbf{B} = -\nabla \Phi \times \mathbf{B} + (\mathbf{U} \times \mathbf{B}) \times \mathbf{B} = -\nabla \Phi \times \mathbf{B} - |\mathbf{B}|^2 \mathbf{U}_\perp$$

where \mathbf{U}_\perp stands for the velocity components perpendicular to \mathbf{B} . $(\mathbf{U} \times \mathbf{B}) \times \mathbf{B}$ is the electromagnetic braking, while $-\nabla \Phi \times \mathbf{B}$ is more often accelerating the fluid. In the vicinity of an insulating side wall, the $\nabla \Phi$ term forces the current to an opposite direction of the $(\mathbf{U} \times \mathbf{B})$ -part of the current.

Then the x-component of $(\mathbf{U} \times \mathbf{B}) \times \mathbf{B}$ is discretized as:

$$[(\mathbf{U} \times \mathbf{B}) \times \mathbf{B}]_{x_{i,j,k}} = -By^2 vx_{i,j,k}$$

The temporary velocity can now be expressed easier as:

$$\begin{aligned} vx_{i,j,k}^{\text{temp}} = & \\ vx_{i,j,k} \left(1 - \frac{\Delta t}{4 \Delta x} vx_{i+1,j,k} + \frac{\Delta t}{4 \Delta x} vx_{i-1,j,k} - \Delta t N By^2 - 2 \frac{\Delta t N}{Ha^2} (\Delta x^{-2} + \Delta y^{-2} + \Delta z^{-2}) \right) & \\ + vx_{i+1,j,k} \left(-\frac{\Delta t}{4 \Delta x} vx_{i+1,j,k} - \frac{\Delta t}{4 \Delta x} vx_{i,j,k} + \frac{\Delta t N}{\Delta x^2 Ha^2} \right) & \\ + vx_{i-1,j,k} \left(+\frac{\Delta t}{4 \Delta x} vx_{i,j,k} + \frac{\Delta t}{4 \Delta x} vx_{i-1,j,k} + \frac{\Delta t N}{\Delta x^2 Ha^2} \right) & \\ + vx_{i,j+1,k} \left(\frac{\Delta t N}{\Delta y^2 Ha^2} \right) + vx_{i,j-1,k} \left(\frac{\Delta t N}{\Delta y^2 Ha^2} \right) & \\ + vx_{i,j,k+1} \left(\frac{\Delta t N}{\Delta z^2 Ha^2} \right) + vx_{i,j,k-1} \left(\frac{\Delta t N}{\Delta z^2 Ha^2} \right) & \end{aligned}$$

This new scheme involves only 6 neighbouring points around the point (i, j, k) . With this new expression for the $(\mathbf{U} \times \mathbf{B}) \times \mathbf{B}$ term, all the numerical oscillations are suppressed, and all the weight of the Lorentz force is concentrated on a single grid point. Moreover, this scheme gives an exact value, while the old scheme with subsequent cross-product computation gives an approximate value created by several averaging steps.

1) *diffusion limit for the time step*: the only numerical stability limitation which is modified by the Lorentz force, compared to ordinary hydrodynamics is the diffusion limit. This limitation is now:

$$\Delta t \leq \frac{\text{Re}}{2(\Delta x^{-2} + \Delta y^{-2} + \Delta z^{-2}) + \text{Ha}^2 \text{By}^2}.$$

It appears to be stronger than the limitation of the old scheme, since it involves the whole electromagnetic braking which is not splitted any more on the coefficients of several grid points. The electromagnetic contribution $\text{Ha}^2 \text{By}^2$ is not divided by 4 any more. In the worse case, the time step would be 4 times smaller with the new scheme than it was with the old scheme.

This limitation would be overcome if the $(\mathbf{U} \times \mathbf{B}) \times \mathbf{B}$ term was treated implicitly. This is done most easily by expressing the temporary velocity without this term and taking it into account in the final velocity \mathbf{U}^{new} as

$$\mathbf{U}^{\text{new}} = \mathbf{U}^{\text{temp}} - \Delta t N \nabla P - \Delta t N |\mathbf{B}|^2 \mathbf{U}_{\perp}^{\text{new}},$$

\mathbf{U}^{temp} being now expressed without the $(\mathbf{U} \times \mathbf{B}) \times \mathbf{B}$ term. Then, the diffusion limit is exactly the same as in ordinary computational fluid dynamics:

$$\Delta t \leq \frac{1}{2} \text{Re} \left(\frac{1}{\Delta x^2} + \frac{1}{\Delta y^2} + \frac{1}{\Delta z^2} \right)^{-1}.$$

Unfortunately this implicit scheme for the $(\mathbf{U} \times \mathbf{B}) \times \mathbf{B}$ term fails because it breaks the law of mass conservation. Indeed,

$$\nabla^* \cdot \mathbf{U}^{\text{new}} = \frac{\Delta t N |\mathbf{B}|^2}{1 + \Delta t N |\mathbf{B}|^2} \nabla^* \cdot \mathbf{U}_{\parallel}^{\text{new}}$$

is zero only if $\mathbf{U}_{\parallel}^{\text{new}}$, the component of velocity parallel to the B field, is constant in the whole space, i.e. if $\mathbf{U}_{\parallel}^{\text{new}} = 0$. Then this implicit scheme can only be used to compute a fully developed laminar flow in a straight duct. It is nevertheless of some interest when one wants to set up the initial conditions for an unsteady flow. The initial velocity field is reached faster with this scheme.

2) *mesh Reynolds number limitation*: on the other hand, the mesh Reynolds number limitation is not affected any more by the electromagnetic braking. It is now the same as in ordinary hydrodynamics:

$$\text{Re} \nu x \Delta x \leq 2.$$

If this limit does not hold, standard upwind schemes can be used in the same form as in ordinary fluid dynamics.

3) *no other limitations*: finally, the limitation that was responsible for strong oscillations at the corners of the duct, and that has no equivalent in ordinary fluid dynamics, is now removed. Therefore, there is no limitation any more on the grid spacing in the direction perpendicular to both, magnetic field and velocity, and no stronger limitation on the time step than without the Lorentz force. Finally, the only difference of the new scheme compared to a pure fluid dynamic code lies in the stronger diffusion limit for the time step. However, this limitation is more acceptable for an unsteady flow simulation, since the Reynolds number is larger than that of a laminar steady flow.

2.3—Accuracy of the scheme for the $\mathbf{J} \times \mathbf{B}$ Lorentz force

- Error on $(\mathbf{U} \times \mathbf{B}) \times \mathbf{B}$

The new scheme for $(\mathbf{U} \times \mathbf{B}) \times \mathbf{B}$ is more accurate since it requires no averaging approximation. It is exact as far as the velocity has a correct value. The error of the old scheme for this term is of the order

$$\frac{By}{4} \left(\left| \frac{\partial^2 vx}{\partial x^2} \right| \Delta x^2 + \left| \frac{\partial^2 vx}{\partial z^2} \right| \Delta z^2 \right) \approx O(\Delta x^2, \Delta z^2)$$

- Error on $-\nabla \Phi \times \mathbf{B}$

What about the other term of the Lorentz force? Since it contains only one cross product, there is no way to avoid the averaging calculation due to the staggered grid. This averaging procedure gives rise to an error.

The same problem occurs for the computation of Φ itself. Indeed, the right hand side of the Poisson equation $\nabla^2 \Phi = \nabla \cdot (\mathbf{U} \times \mathbf{B})$ involves the cross product $\mathbf{U} \times \mathbf{B}$. Although this term is computed as

$$\nabla \cdot (\mathbf{U} \times \mathbf{B}) = \mathbf{B} \cdot (\nabla \times \mathbf{U}) - \mathbf{U} \cdot (\nabla \times \mathbf{B}),$$

it is still ill-adapted to the staggered grid since any simple finite difference scheme for the scalar quantity $\mathbf{B} \cdot (\nabla \times \mathbf{U})$ will give a value at a position different from the cell centres. Therefore an average calculation of neighbouring points is needed again.

In the old scheme, the errors on both terms of the Lorentz force partly cancel each other since they are similar and of opposite sign. In the new scheme, only the $-\nabla \Phi \times \mathbf{B}$ term contains an error. Then this error is not counterbalanced by the $(\mathbf{U} \times \mathbf{B}) \times \mathbf{B}$ term which is now exact. Unless a new scheme is chosen for the $-\nabla \Phi \times \mathbf{B}$ term, the new scheme is on the whole less accurate than the old one, although it is stable. The velocity profile calculated with the new scheme at a given Hartmann number looks like the velocity profile at a lower Hartmann number, i.e. the side layers have a larger thickness and a lower velocity than they should have.

Accurate scheme for the $-\nabla \Phi \times \mathbf{B}$ term of the Lorentz force and fully staggered grid

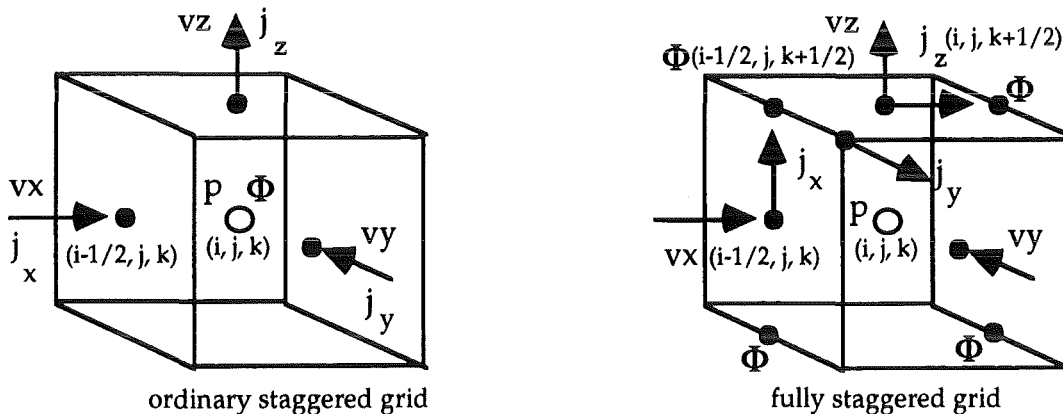


Fig. 2.1

In order to have both, accuracy and stability, a more accurate scheme for $-\nabla \Phi \times \mathbf{B}$ should be chosen. Several schemes have been tried and as a result, the grid itself has been modified. Other attempts to modify the scheme on the ordinary staggered grid have failed. In particular higher order central difference schemes gave some oscillations. When applied to both $\nabla \cdot (\mathbf{U} \times \mathbf{B})$ and $-\nabla \Phi \times \mathbf{B}$ terms, they gave accurate results just before the code started to diverge after a few hundreds of time iterations. The use of higher order central differences applied to only one of the $\nabla \cdot (\mathbf{U} \times \mathbf{B})$ and $-\nabla \Phi \times \mathbf{B}$ terms was found to be stable but helpless since it almost did not improve the accuracy.

The only way to avoid the averaging procedure of cross products is to use a different grid. The electric potential should not be calculated at the cell centres but on the edges of the cells. This type of mesh is referred as a 'fully staggered grid' (Y. Shimomura, 1991). This new grid is better than the old one because it allows to calculate the cross product without averaging since the two vectors $-\nabla \Phi$ and \mathbf{B} are defined at the same point. The first order derivatives are then calculated with central differences of the form:

$$\left. \frac{\partial u}{\partial z} \right|_{k+1/2} = \frac{u_{k+1} - u_k}{\Delta z},$$

instead of an average of several central differences of the form

$$\left. \frac{\partial u}{\partial z} \right|_k = \frac{u_{k+1} - u_{k-1}}{2\Delta z},$$

where u represents both v_x for the computation of $\nabla \cdot (\mathbf{U} \times \mathbf{B})$, and Φ for the computation of $-\nabla \Phi \times \mathbf{B}$. The new scheme has the accuracy of a grid of size Δz , while the old scheme has the accuracy of a grid of size $2\Delta z$.

Note that this new grid allows a \mathbf{B} -field in the y -direction only. If more than one component for this field was needed, then one should try a fully staggered grid with the electric potential defined at the 8 corners of the cell.

Divergence of the Lorentz force

Although not zero, the divergence of the Lorentz force should have a correct value when it is discretised on a staggered grid. This non zero divergence is due to the variations of the velocity in the \mathbf{B} field direction only as shown below. Let us split the divergence of $\mathbf{J} \times \mathbf{B}$ into two terms:

$$\nabla \cdot (\mathbf{J} \times \mathbf{B}) = -\nabla \cdot (\nabla \Phi \times \mathbf{B}) + \nabla \cdot [(\mathbf{U} \times \mathbf{B}) \times \mathbf{B}]$$

Then, the first term is zero as far as $\nabla \times \mathbf{B} = 0$ which is verified when \mathbf{B} is chosen to be constant:

$$\nabla \cdot (\nabla \Phi \times \mathbf{B}) = \mathbf{B} \cdot (\nabla \times \nabla \Phi) - \nabla \Phi \cdot (\nabla \times \mathbf{B}) = 0$$

The second term is responsible for the non zero divergence. Split it again into two terms:

$$\nabla \cdot [(\mathbf{U} \times \mathbf{B}) \times \mathbf{B}] = \mathbf{B} \cdot [\nabla \times (\mathbf{U} \times \mathbf{B})] - (\mathbf{U} \times \mathbf{B}) \cdot (\nabla \times \mathbf{B}),$$

and the 2nd term vanishes since we suppose that $\nabla \times \mathbf{B} = 0$. Write $\nabla \times (\mathbf{U} \times \mathbf{B})$ in the following form:

$$\nabla \times (\mathbf{U} \times \mathbf{B}) = \mathbf{U} (\nabla \cdot \mathbf{B}) - \mathbf{B} (\nabla \cdot \mathbf{U}) + (\mathbf{B} \cdot \nabla) \mathbf{U} - (\mathbf{U} \cdot \nabla) \mathbf{B} = (\mathbf{B} \cdot \nabla) \mathbf{U}$$

Note that $\nabla \cdot \mathbf{B} = \nabla \cdot \mathbf{U} = 0$, and that $(\mathbf{U} \cdot \nabla) \mathbf{B} = 0$ since \mathbf{B} is constant. Then,

$$\mathbf{B} \cdot [\nabla \times (\mathbf{U} \times \mathbf{B})] = \mathbf{B} \cdot [(\mathbf{B} \cdot \nabla) \mathbf{U}] = B_y \frac{\partial v_y}{\partial y} \text{ if } \mathbf{B} = B_y = \text{Cst}$$

Finally the divergence of the Lorentz force in case of constant magnetic field $\mathbf{B} = B_y = \text{Cst}$ is proportional to the first derivative of the velocity aligned with \mathbf{B} in the direction of \mathbf{B} :

$$\nabla \cdot (\mathbf{J} \times \mathbf{B}) = B_y \frac{\partial v_y}{\partial y}.$$

2.4—Examples of computation with the different schemes

The following pages show two examples of computation:

- one with the old scheme and the ordinary staggered grid (top)
- and one with the new scheme and the fully staggered grid (bottom).

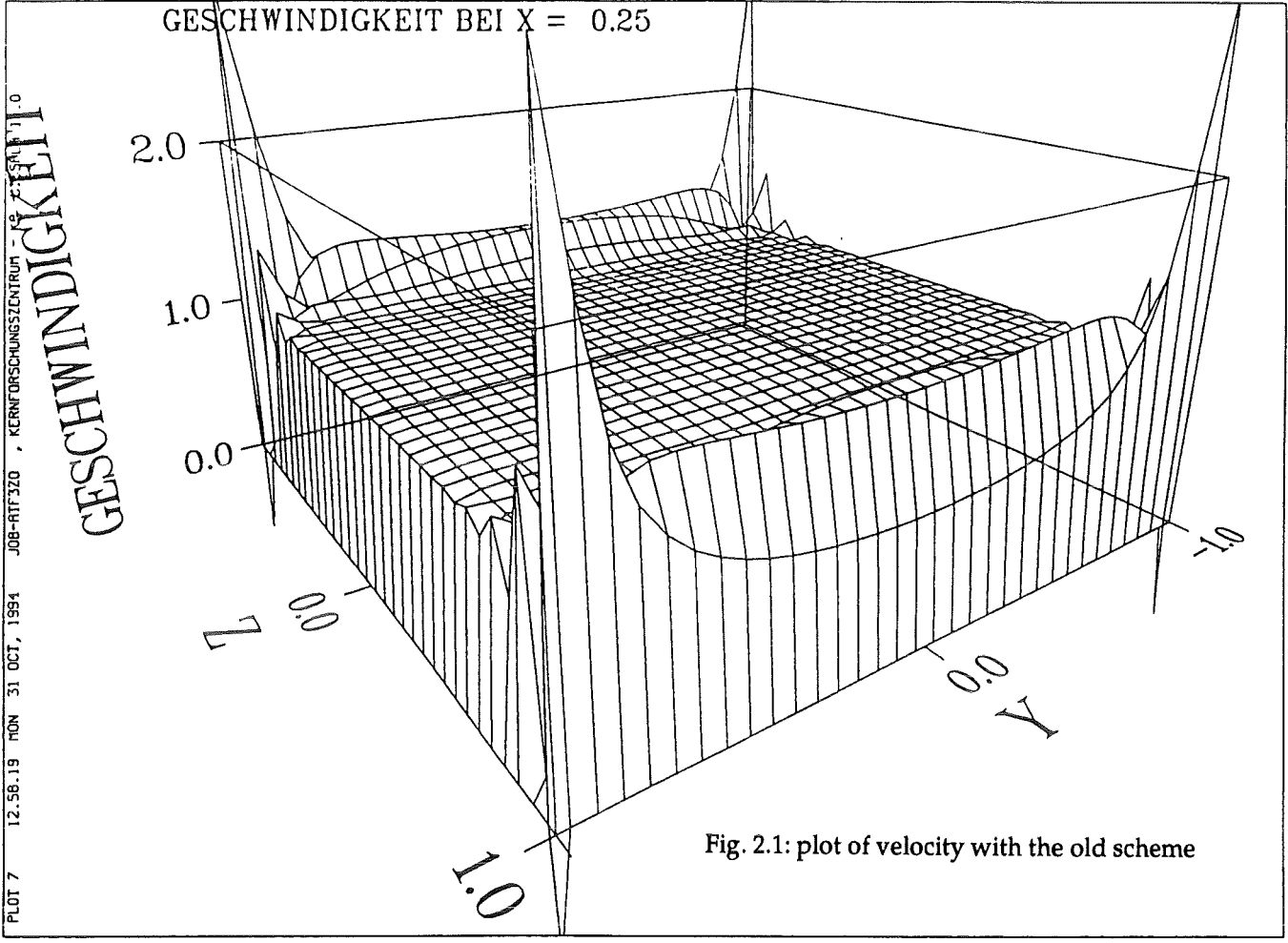
Both examples are made with a grid size of 32×32 cells in the cross section of the duct. The Hartmann number is 200 and the interaction parameter is 5000, i.e. the same as often used in the report of L. Lenhart (1994). All walls are perfectly conducting. One can see the oscillations of the old scheme and the stable solution of the new scheme. Moreover, the stable solution shows that for such a Hartmann number, not only the Hartmann layers are not resolved but also the side layers have a very poor resolution.

```

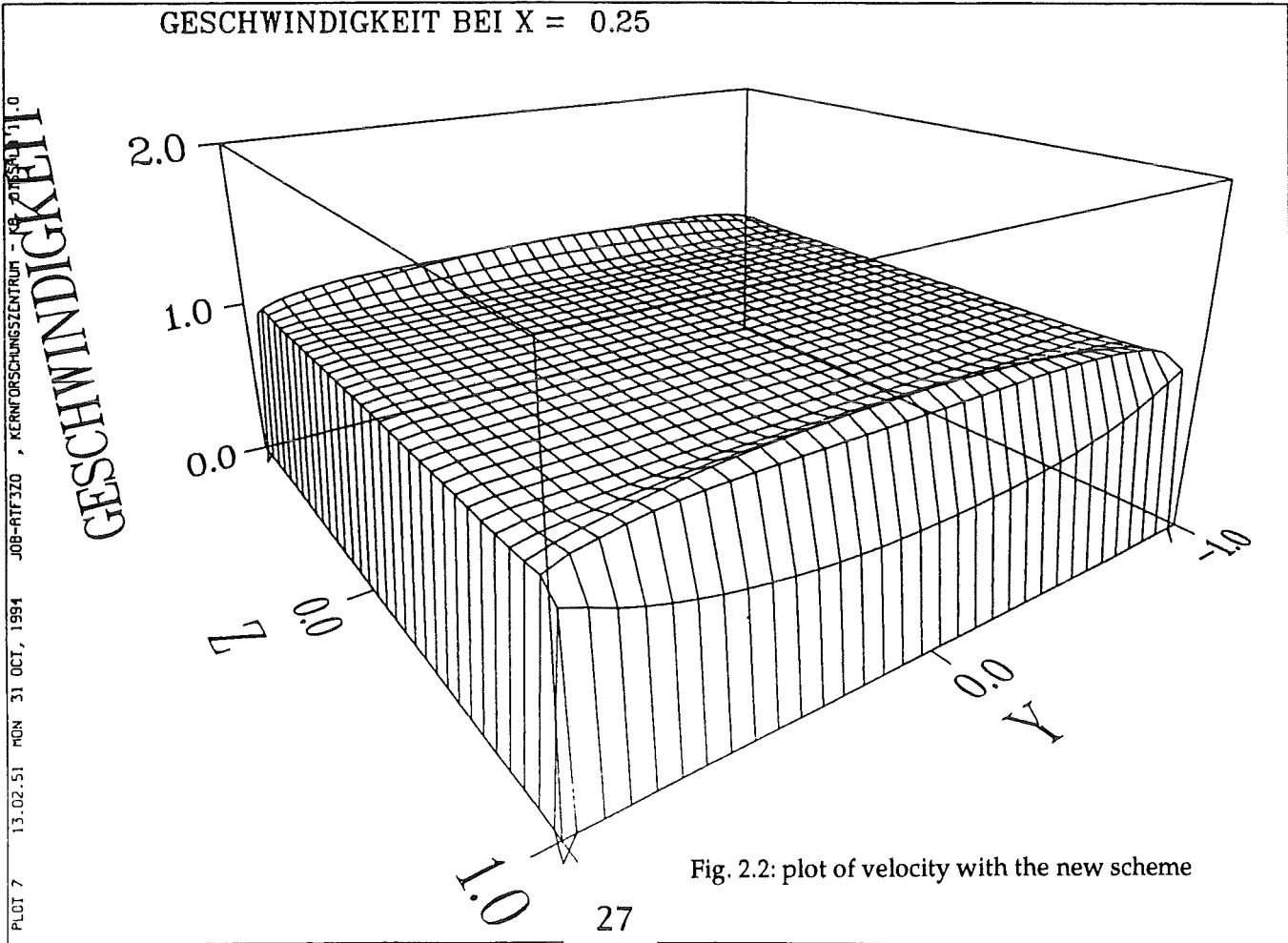
&INNEW      CYU = 1.00D-1, CYO = 1.00D-1, CZU = 1.D-1,  CZO = 1.D-1,
            IRAND = 0,      ISUPR = 0,      ISYMS = 0,      IADBA = 0,
            IJBLF = 0,      IMPLIC = 0,      MINUTE = 03,      ISECON = 00
&END
&INALL      HA      = 2.0D+2,      ST      = 5.0D+3,      DT      = 1.0D-4,
            ALFA    = 9.0D1,      X0      = 0.0D0,      TOL    = 1.0D-9,
            DX      = 0.10000D0,  DY      = 0.06250D0,  DZ      = 0.06250D0,
            ISTOP   = 1,          JSTOP   = 1,          KSTOP   = 1,
            MSTP    =9999,        ICOMP   = 001,        IPRINT=9999,
            START   ='N',        IPARTS  = 1,
            INFO    =' MHD BEI KONSTANTEM MAGNETFELD  BY=1  '
&END
&INPUT      XL      = 0.0D0,      2.0D-1,  1.0D0,  -0.5D0,  -1.5D0,
            XH      = 0.4D0,      4.0D-1,  2.0D0,  0.5D0,  -0.5D0,
            YL      = -1.0D0,     -1.0D-1,  0.5D0,  0.5D0,  0.5D0,
            YH      = 1.0D0,      1.0D-1,  1.5D0,  1.5D0,  1.5D0,
            ZL      = -1.0D0,     -1.0D-1, -0.5D0, -0.5D0, -0.5D0,
            ZH      = 1.0D0,      1.0D-1,  0.5D0,  0.5D0,  0.5D0,
            IBCXL   = 3,          5,          5,          2,          4,
            IBCXH   = 4,          4,          4,          2,          5,
            IBCYL   = 1,          1,          1,          5,          1,
            IBCYH   = 1,          1,          1,          4,          1,
            IBCZL   = 1,          1,          2,          2,          2,
            IBCZH   = 1,          1,          2,          2,          2,
            ICROSS  = 1,          1,          4,          3,          1,
            VXWERT  = 1.0D0,      1.0D0,      0.0D0,      0.0D0,      -1.0D0,
            VYWERT  = 0.0D0,      0.0D0,      1.0D0,      1.0D0,      0.0D0,
            VZWERT  = 0.0D0,      0.0D0,      0.0D0,      0.0D0,      0.0D0
&END

```

Table 2.1: copy of namelists



31 OCT 1994 12:58 PM BY ATF320



PLOT 7 13.02.51 MON 31 OCT, 1994 JOB-ATF320 , KERNFORSCHUNGSZENTRUM - KARLSRUHE - 1.0

POTENTIAL AT X = 0.25

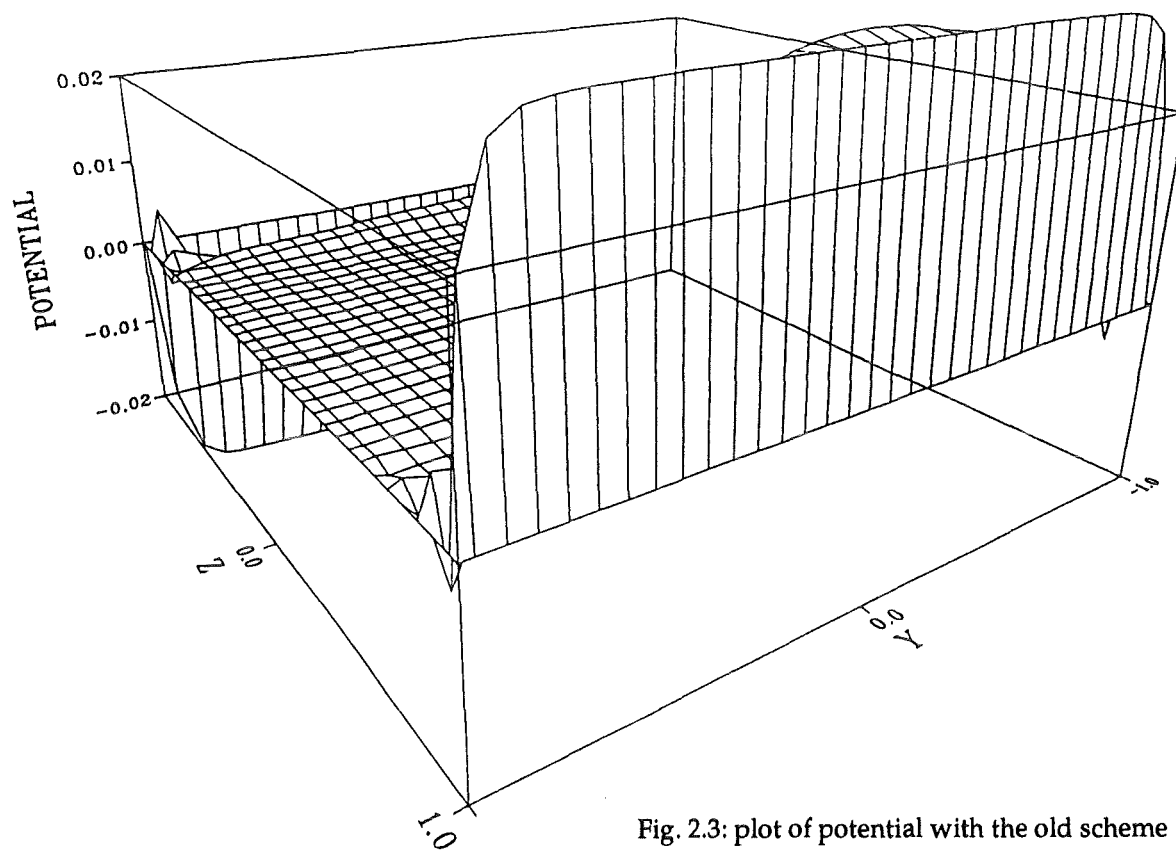


Fig. 2.3: plot of potential with the old scheme

PLOT 7 20.24.52 MON 31 OCT, 1994 JOB-RTF320 , KERNFORSCHUNGSZENTRUM - KR DISSPLA 11.0

31 OCT 1994 8:25 PM BY ATF328

POTENTIAL AT X = 0.25

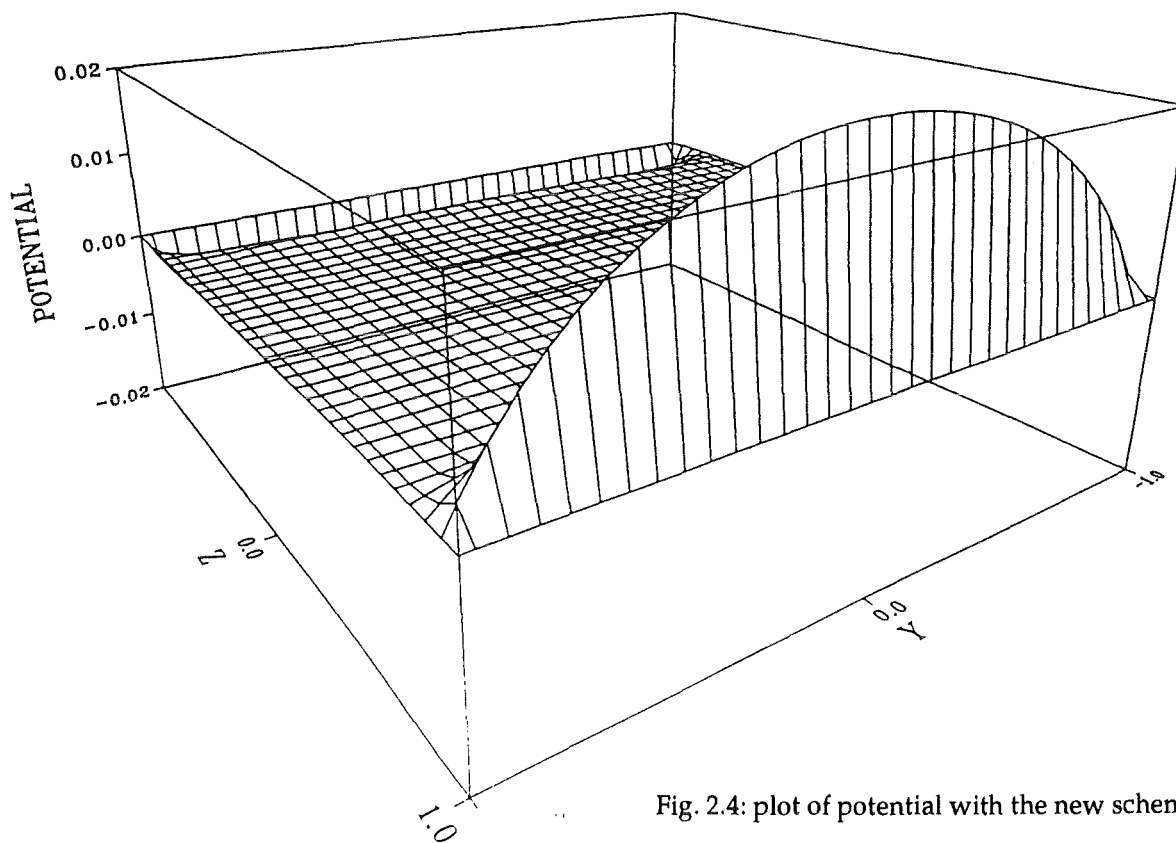


Fig. 2.4: plot of potential with the new scheme

PLOT 7 20.20.11 MON 31 OCT, 1994 JOB-RTF320 , KERNFORSCHUNGSZENTRUM - KR DISSPLA 11.0

**3—ARBITRARY WALL CONDUCTIVITY
& INTEGRAL TREATMENT OF THE HARTMANN LAYERS**

3.1—Arbitrary conductivity of the walls

If the walls of the duct have an arbitrary electrical conductivity, then the currents inside the walls have to be computed since they modify the currents in the fluid itself. In such a case, the thin wall condition (Walker 1981) is used. The thickness ϵ of the walls is supposed to be much smaller than the width of the duct ($\epsilon \ll a$) so that the currents in the walls are modelled as a sheet of current.

The normal component of current coming from the fluid is a source for the current in the wall. Therefore it gives rise to a non zero divergence of the 2-dimensional current tangential to the wall:

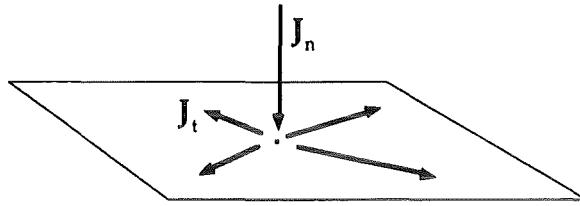


Fig. 3.1

$$J_n = \nabla_t \cdot J_t,$$

or in terms of electric potential,

$$\nabla_n \Phi = \nabla_t \cdot (c \nabla_t \Phi) \quad (3.2)$$

where the wall conductance ratio c is defined as the ratio of the apparent conductivity of the wall σ_{ap} to the conductivity of the fluid σ

$$c = \frac{\sigma_{ap}}{\sigma},$$

and the apparent conductivity of the wall σ_{ap} is the conductivity of the wall σ_w times its relative thickness ϵ/a :

$$\sigma_{ap} = \frac{\epsilon}{a} \sigma_w.$$

Iterative computation of the electric potential at the wall

The potential at the wall has been computed in the past with a 2-D Poisson-solver (A. Sterl, 1990). The iterative method that was used is the following.

One starts with arbitrary Dirichlet boundary conditions at the wall for the 3-D Poisson solver that gives a solution for the potential in the fluid. This 3D solution also gives the normal derivative of the potential at the walls. Then equation (3.2) can be solved for the potential at the walls using a 2-D Poisson solver that gives a new value of the wall potential. This new value of the wall potential is then used as a Dirichlet boundary condition for the 3-D Poisson

solver. This process is repeated until the potential converges to some value. This algorithm has been used in the new code but only for the ordinary staggered grid and the old finite difference scheme.

An easier algorithm is used in the new code for the fully staggered grid and the new finite difference scheme. It does the same iteration procedure, but in the other way round. One starts with arbitrary Neumann boundary conditions at the wall for the 3-D Poisson solver that gives a solution for the potential in the fluid. This 3-D solution also gives the wall potential itself. Then eq. (3.4) gives directly the normal derivative of the potential at the wall, without the need to solve a 2-D Poisson equation. This new value of the normal derivative of the wall potential is then used as a Neumann boundary condition for the 3-D poisson solver. This process is also repeated until it converges.

In the new code, the convergence is accelerated by an initial guess of the solution at each time step. This guess $\nabla_n \Phi^{\text{new}}$ is first order in time; it is estimated from the solution at the two previous iteration steps $\nabla_n \Phi^{\text{old}}$ and $\nabla_n \Phi^{\text{older}}$. It is defined in such a way that

$$\nabla_n \Phi^{\text{new}} - \nabla_n \Phi^{\text{old}} = \nabla_n \Phi^{\text{old}} - \nabla_n \Phi^{\text{older}}$$

Both old and new iteration algorithm between the volume and its boundaries requires a stabilising under-relaxation; the wall potential or its derivative at the new step is set to an average value between the last step and the new step. The relaxation coefficient is set to the highest value as possible in order to converge as fast as possible. This value depends on the different parameters of the run and is set empirically by starting the execution for a few time steps only. If the relaxation coefficient is too high, the code diverges usually at the first time step. For the most unstable calculation given at the end of this report, the code needs on average 12 iterations steps on the potential per time step.

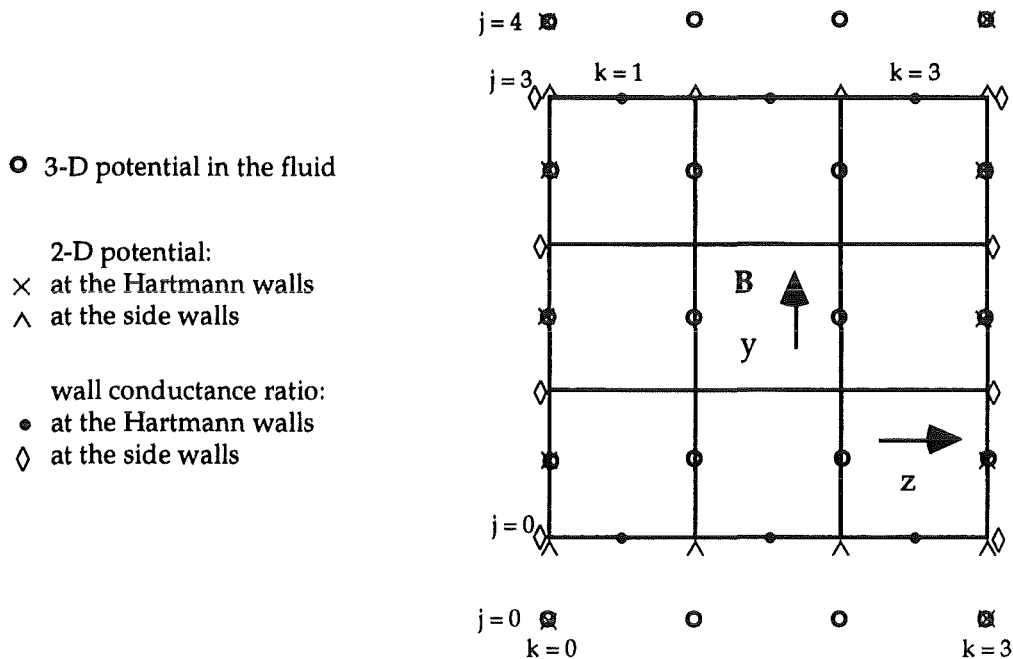


Fig. 3.2: discretisation of the electric potential in the fluid and on the walls

The computation of the potential at the corners of the duct needs some care. On the ordinary staggered grid, the treatment has already been described (A. Sterl, 1989). On the fully staggered grid, the potential at the wall occupies the following positions shown in Fig. 3.2.

On the side walls., the potential at the wall and the potential in the fluid are just the same, and $\nabla_{\tau} \cdot (c\nabla_{\tau}\Phi)$ is computed as:

$$\frac{c_{swj, k} [\Phi_{j+1, k} - \Phi_{j, k}] - c_{swj-1, k} [\Phi_{j, k} - \Phi_{j-1, k}]}{\Delta y^2} \quad (1 \leq j \leq 3, k = 0 \text{ or } 3, \text{ see fig. 3.2})$$

On the Hartmann walls, the potential at the wall is the average value of two values of the potential in the fluid, and $\nabla_{\tau} \cdot (c\nabla_{\tau}\Phi)$ is computed as:

$$\frac{c_{hwj, k+1} [\Phi_{j, k+1} - \Phi_{j, k}] - c_{hwj, k} [\Phi_{j, k} - \Phi_{j, k-1}]}{\Delta z^2} \quad (j = 0 \text{ or } 3, 0 \leq k \leq 3) \quad (3.4)$$

The value of the potential standing in the neighbourhood of the Hartmann walls, and out of the duct, is given by the Neumann boundary conditions that are used in the 3-D Poisson solver.

Therefore, on the Hartmann walls $\nabla_n \Phi$ is expressed as

$$\nabla_n \Phi = \frac{\Phi_{j+1, k} - \Phi_{j, k}}{\Delta y} \quad (j = 0 \text{ or } 3, 0 \leq k \leq 3, \text{ see fig. 3.2})$$

The treatment of the corners is done when computing the potential at the Hartmann walls and not at the side walls since the potential at the corners is only defined on the Hartmann walls as one can see from the last figure. In the corners, the conservation law $\nabla_n \Phi = \nabla_{\tau} \cdot (c\nabla_{\tau}\Phi)$ should be written in a different way. Indeed, $\nabla_n \Phi = \nabla_y \Phi$ does not only create a current leaving the Hartmann wall in direction of the fluid, but it also create a current leaving this wall and entering the side wall. The y-component of the current density at the corner is written $-c_{sw} \nabla_y \Phi - 1/2 \Delta z \nabla_y \Phi$. The term $-c_{sw} \nabla_y \Phi$ is the current leaving the Hartmann wall and entering the side wall. The term $-1/2 \Delta z \nabla_y \Phi$ is the current leaving the Hartmann wall and entering the fluid. The 1/2 coefficient comes from the absence of fluid on that side out of the duct. The current leaving the Hartmann wall and entering the fluid in the neighbourhood of the corner, can only do so from that side inside the duct. Finally the conservation law at the corner should be written:

$$c_{sw} \nabla_y \Phi + \frac{1}{2} \Delta z \nabla_y \Phi = c_{hw} \nabla_z \Phi$$

3.2—Integral treatment of the Hartmann layer

For high values of the Hartmann number, the Hartmann layers are so thin that they become impossible to be modelled with numerical codes based on a constant grid spacing. Moreover, if one wants to implement a non regular mesh, the diffusive viscous term should be treated implicitly. Otherwise the time step which is limited at least to $1/2 \text{ Re} / (\Delta x^{-2} + \Delta y^{-2} + \Delta z^{-2})$ by the explicit

scheme of the code would tend to zero as $\Delta x, \Delta y, \Delta z \rightarrow 0$. Furthermore, a non regular spacing would increase the computation time when solving the two Poisson equations for pressure and potential.

As already pointed out (L. Bühler 1994), the Hartmann layer can be removed from the model, with the use of the electric potential boundary conditions that we have defined for walls of arbitrary conductivity. The electric currents in the Hartmann layer are then included in the theory in the same way as the currents in the walls. The boundary condition for potential becomes

$$\nabla_n \Phi = \nabla_t \cdot ((c + \delta) \nabla_t \Phi). \quad (3.5)$$

Indeed, let us write the actual velocity U_t which decreases exponentially across the Hartmann layer, from the velocity U_t^C in the core to $U_t = 0$ at the wall.

$$U_t = U_t^C (1 - e^{-n/\delta}). \quad (3.6)$$

U_t^C is the velocity in the core which is reached when n is big enough. Let us compare the actual current density J_t to the current density J_t^C outside the Hartmann layer

$$J_t = -\nabla_t \Phi + U_t \times B, \quad (3.7)$$

$$J_t^C = -\nabla_t \Phi^C + U_t^C \times B. \quad (3.8)$$

Since the potential is continuous between the wall and the Hartmann layer, $\Phi^C \sim \Phi$, the contribution of the Hartmann layer to the tangential current is

$$J_t^\delta = J_t - J_t^C = -(\nabla_t \Phi^C + J_t^C) e^{-n/\delta}$$

and should be divergence free

$$\nabla \cdot J^\delta = 0 = \nabla_t \cdot J_t^\delta + \nabla_n \cdot J_n^\delta.$$

Integrating this relation in the normal direction from 0 to ∞ gives an expression for the jump in the normal component of this current over the Hartmann layer.

$$\begin{aligned} \Delta J_n^\delta &= J_n^\delta|_\infty - J_n^\delta|_0 = \int_0^\infty \nabla_n \cdot J_n^\delta \, dn = - \int_0^\infty \nabla_t \cdot J_t^\delta \, dn \\ &= - \int_0^\infty \nabla_t \cdot (\nabla_t \Phi^C + J_t^C) e^{-n/\delta} \, dn = -\nabla_t \cdot (\delta \nabla_t \Phi^C + \delta J_t^C). \end{aligned}$$

Then the jump ΔJ_n of the normal component J_n of the total current is

$$\Delta J_n = \Delta J_n^\delta + \Delta J_n^C = -\nabla_t \cdot (\delta \nabla_t \Phi^C).$$

Therefore the Hartmann layer can be modelled in the same way as a thin wall of arbitrary conductivity. It can be replaced by an infinitely thin sheet of current where the normal current entering this sheet gives rise to a divergence in its plane. Both wall and Hartmann layer can be superposed as a single sheet of current. The boundary condition for the electric potential is then (3.5).

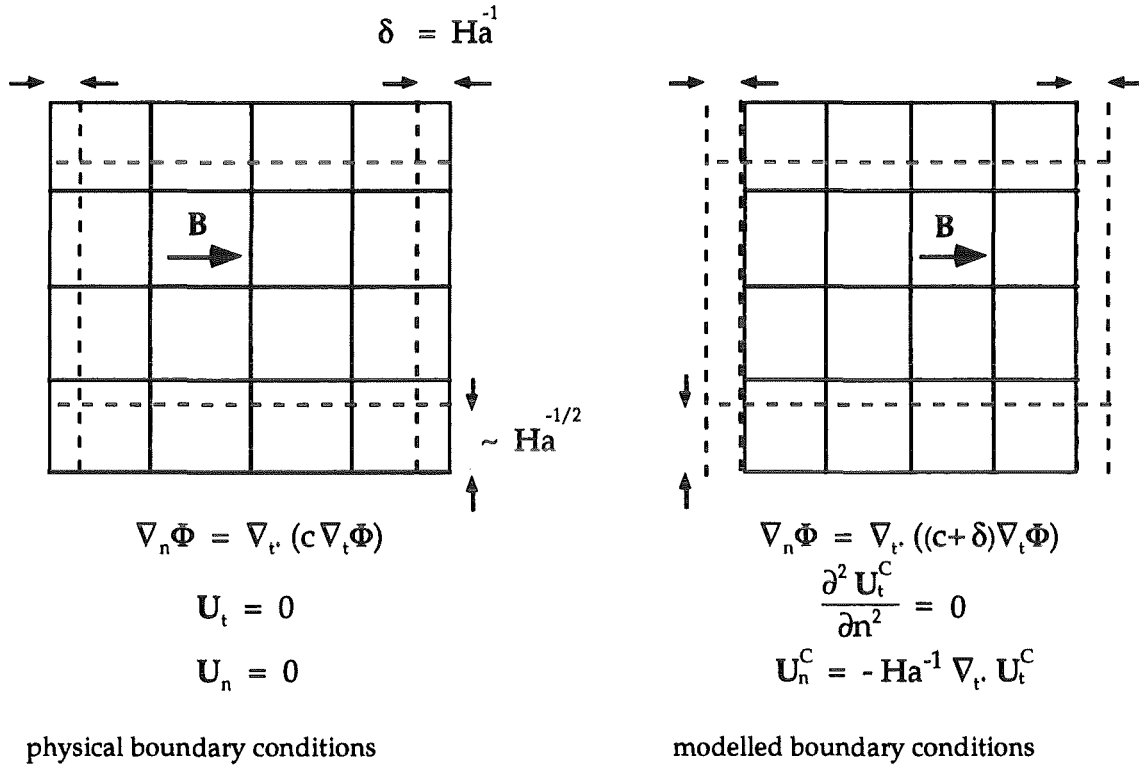


Fig. 3.3: treatment of the Hartmann layers

3.3—Boundary condition for the tangential component of the velocity

If the Hartmann layers are removed from the mesh, then modified boundary conditions for the tangential and normal components of the velocity are needed. Subtract equation (3.7) from equation (3.8), then the contribution of the Hartmann layer to the current density can be written

$$J_t^\delta = J_t - J_t^C = \nabla_t \cdot (\Phi^C - \Phi) - (U_t^C - U_t) \times B \sim - (U_t^C - U_t) \times B$$

One can then integrate the last relation in the normal direction, from the wall to the core, and express the current in the Hartmann layer as a function of the velocity in the core:

$$\int_0^\infty J_t^\delta dn = -U_t^C \times B \int_0^\infty e^{-n/\delta} dn = -\delta U_t^C \times B.$$

Therefore, even for a non parallel flow, the electric current in the Hartmann layer is proportional to the velocity of the fluid out of the layer. Note that $\delta=Ha^{-1}$, multiply both sides of the above equation by $B \times$, and define J_t^M as the whole current in the Hartmann layer

$$\mathbf{J}_t^M = \int_0^\infty (\mathbf{J}_t - \mathbf{J}_t^C) \, dn,$$

then

$$\mathbf{U}_t^C = \text{Ha} \mathbf{J}_t^M \times \mathbf{B}$$

Therefore, even for a non parallel flow, the electric current in the Hartmann layer is proportional to the velocity of the fluid out of the layer.

It is hard to derive a practical boundary condition from this relation, since it requires in advance the knowledge of the current density which can only be calculated once the velocity field is known.

The practical boundary condition used in the code when the Hartmann layer are removed from the discretised computational domain is to suppress the viscous braking at the Hartmann walls, i.e. the second derivative in the direction normal to the walls of the component of velocity parallel to the walls is set to zero.

$$\frac{\partial^2 \mathbf{U}_t^C}{\partial n^2} = 0.$$

Such a condition neglects viscous braking in the core, near the wall, an obvious assumption, since viscous braking is already taken into account by adding the thickness of the Hartmann layer to the wall conductance ratio. Indeed, this modified electrical boundary condition allows more electric current to flow at the boundary. This additional current closes then in the core where the interaction with the magnetic field causes the required braking effect due to the modelled Hartmann layers.

But it can be that the core itself, even in a region far from the Hartmann layers is submitted to some small viscous effect. This is the case when the velocity profile in the core has some curvature. Usually, the core is a 'quiet' region with a flat velocity profile. Things are different in the side layers showing a parabolic velocity profile along the magnetic field. This parabolic profile implies that the second derivative of the velocity in the direction parallel to the B-field is constant. Then one may prefer the following boundary condition at the Hartmann walls:

$$\frac{\partial^3 \mathbf{U}_t^C}{\partial n^3} = 0.$$

Furthermore, if the flow is 3-dimensional, as it is the case when it is unstable or when it passes through a non uniform B-field, the core velocity can have any profile. There is then no better thing to do than to extrapolate the velocity in the core onto the Hartmann walls. This can be done for instance by setting to zero higher order normal derivatives. The higher the order is, the better the extrapolation is. The code is actually using a zero fourth order normal derivative.

As a summary, there is no satisfactory boundary condition available for the tangential core velocity at the Hartmann walls. But one can easily show that this boundary condition has a very small influence on the result. Even if this condition is chosen as a first order derivative, which is a completely wrong in

the vicinity of the side layers, the results in terms of velocity profile or pressure drop show a slight difference compared to the results obtained with higher order derivatives. This fact is consistent with the small effect of the viscosity in the core flow at high Reynolds numbers.

An example of computation with Hartmann number = 100 with two completely different boundary conditions for U_i^C is given on the following page. The figure 3.4 show the core velocities. The side walls are insulating while the Hartmann walls have a wall conductance ratio $c = 0.07$. Such parameters generate jets at the side layers and a non constant $\partial v_x / \partial n$ at the Hartmann walls. The upper plot correspond to the 4th order normal derivative of v_x set to zero at the Hartmann walls. The lower plot has the 1st order normal derivative of v_x set to zero so that the velocity profile becomes suddenly horizontal at the Hartmann walls.

In spite of this drastic difference, the maximum velocity in the jet, the minimum velocity in the core, and the pressure drops are almost the same:

- boundary condition	$\frac{\partial^4 v_x}{\partial y^4} = 0$	$\frac{\partial v_x}{\partial y} = 0$
- v_x maximum in the jet	2.076	2.077
- v_x minimum in the core	0.872	0.871
- pressure gradient	0.0645	0.0644

PLOT 7 10.35.51 THUR 3 AUG, 1995 JOB-RIF320 , KERNFORSCHUNGSZENTRUM - KA DISSPLA 11.0

X-VELOCITY

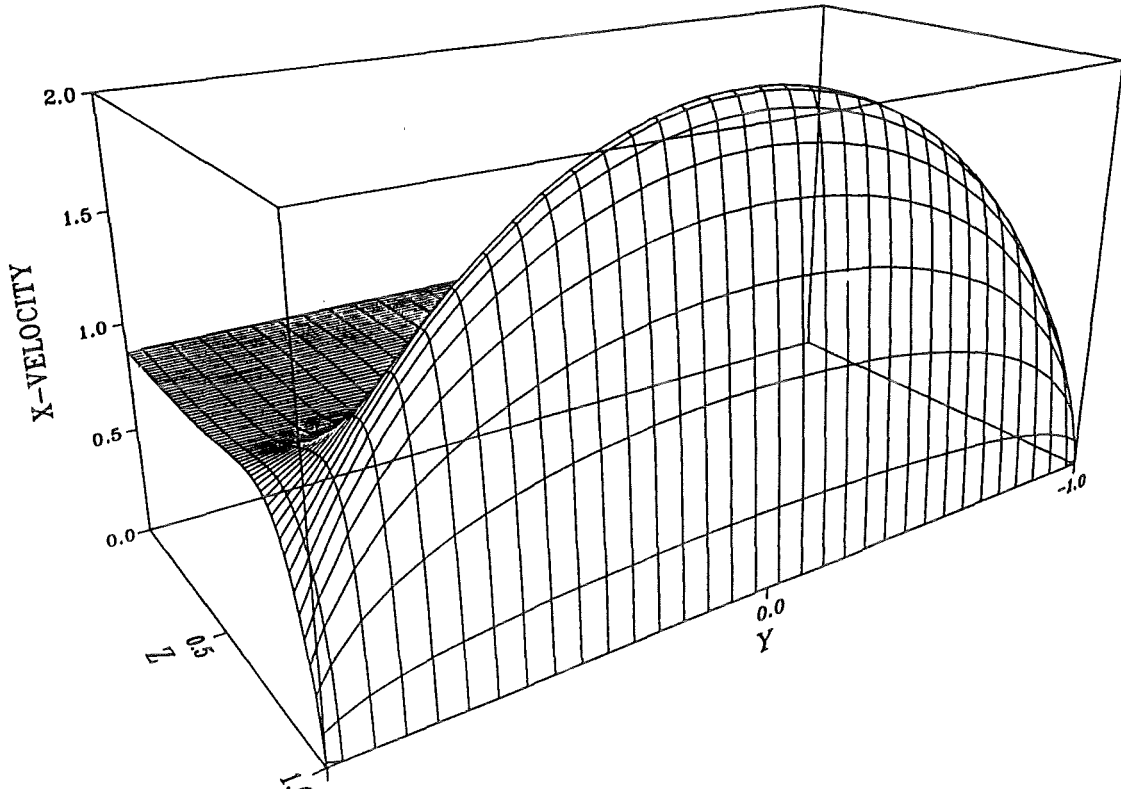


Fig. 3.4: velocity plot — $Ha = 100$, $c_{HW} = 0.07$, $c_{SW} = 0$, $\partial^4 v_x / \partial y^4 = 0$ at the Hartmann walls, calculated pressure gradient = 0.0645

PLOT 7 10.37.38 THUR 3 AUG, 1995 JOB-RIF320 , KERNFORSCHUNGSZENTRUM - KA DISSPLA 11.0

X-VELOCITY

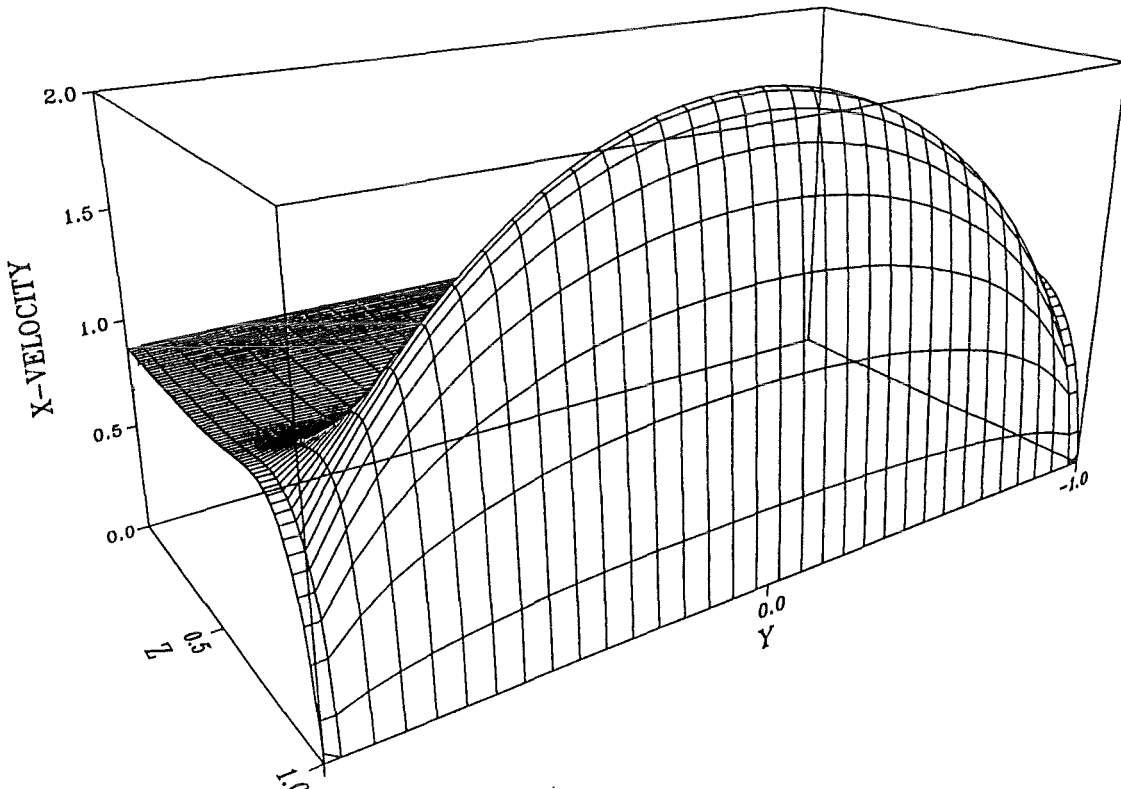


Fig. 3.5: velocity plot — $Ha = 100$, $c_{HW} = 0.07$, $c_{SW} = 0$, $\partial v_x / \partial y = 0$ at the Hartmann walls, calculated pressure gradient = 0.0644

3.4—Boundary condition for the normal component of the velocity

Consider the continuity equation,

$$\nabla_n U_n = -\nabla_t \cdot U_t.$$

If n is the direction normal to the Hartmann wall, integrating this equation in the normal direction from the wall ($n=0$) to the core ($n \rightarrow \infty$), with the use of equation (3.6) leads to

$$U_n^C = -[n - \delta(1 - e^{-n/\delta})] \nabla_t \cdot U_t^C.$$

Then, if $n/\delta \gg 1$,

$$U_n^C = -(n - \delta) \nabla_t \cdot U_t^C$$

as if the wall was shifted by a distance δ , and the Hartmann layer suppressed (R. Moreau, 1990). Let then the Hartmann layer be removed and replaced by the appropriate analytical boundary condition. In the dimensionless form, this equation becomes at the boundary ($n = 0$):

$$U_n^C = Ha^{-1} \nabla_t \cdot U_t^C$$

Therefore $U_n^C \rightarrow 0$, as $Ha \rightarrow \infty$.

3.5—Example of computation at Hartmann number = 1000

The following pages show an example of computation at a high Hartmann number with the integral treatment of the Hartmann layer. The most numerically unstable case is chosen, i.e. all walls perfectly conducting. The grid size is 8×128 cells in the cross section of the duct. It has the same number of grid points as in the examples of section 2.4 since $8 \times 128 = 32 \times 32$. The integral treatment of the Hartmann layers allows to use few grid point in the direction of the magnetic field and therefore, more grid points to resolve the side layers. Moreover, and in spite the high value of the Hartmann number, one can see that the new scheme with the fully staggered grid provide numerically stable calculation.

```

&INFC      CYU = 1.00D-1, CYO = 1.00D-1, CZU = 1.D-1,  CZO = 1.D-1,
IRAND = 0,  ISUPR = 1,  ISYMS = 0,  IADBA = 0,
ICYCL = 0,  MINUTE = 00,  ISECON = 30,  IJBLF = 2
&END
&INALL     HA   = 1.0D+3,   ST   = 1.0D+3,   DT   = 5.0D-4,
ALFA = 9.0D1,   X0   = 0.0D0,   TOL  = 1.0D-4,
DX   = 0.1000D0, DY   = 0.2500D0, DZ   = 0.015625D0,
ISTP = 1,      JSTP = 1,      KSTP = 1,
MSTP =9999,    ICOMP = 001,    IPRINT=9999,
START = 'Y',   IPARTS= 1,
INFO  = ' MHD BEI KONSTANTEM MAGNETFELD  BY=1  '
&END
&INPUT     XL   = 0.0D0,  2.0D-1,  1.0D0,  -0.5D0,  -1.5D0,
XH   = 0.4D0,  4.0D-1,  2.0D0,  0.5D0,  -0.5D0,
YL   = -1.0D0, -1.0D-1,  0.5D0,  0.5D0,  0.5D0,
YH   = 1.0D0,  1.0D-1,  1.5D0,  1.5D0,  1.5D0,
ZL   = -1.0D0, -1.0D-1, -0.5D0, -0.5D0, -0.5D0,
ZH   = 1.0D0,  1.0D-1,  0.5D0,  0.5D0,  0.5D0,
IBCXL = 3,     5,     5,     2,     4,
IBCXH = 4,     4,     4,     2,     5,
IBCYL = 1,     1,     1,     5,     1,
IBCYH = 1,     1,     1,     4,     1,
IBCZL = 1,     1,     2,     2,     2,
IBCZH = 1,     1,     2,     2,     2,
ICROSS = 1,    1,     4,     3,     1,
VXWERT = 1.0D0, 1.0D0, 0.0D0, 0.0D0, -1.0D0,
VYWERT = 0.0D0, 0.0D0, 1.0D0, 1.0D0, 0.0D0,
VZWERT = 0.0D0, 0.0D0, 0.0D0, 0.0D0, 0.0D0
&END

```

Table 3.1: copy of namelists

GESCHWINDIGKEIT

GESCHWINDIGKEIT BEI X = 0.25

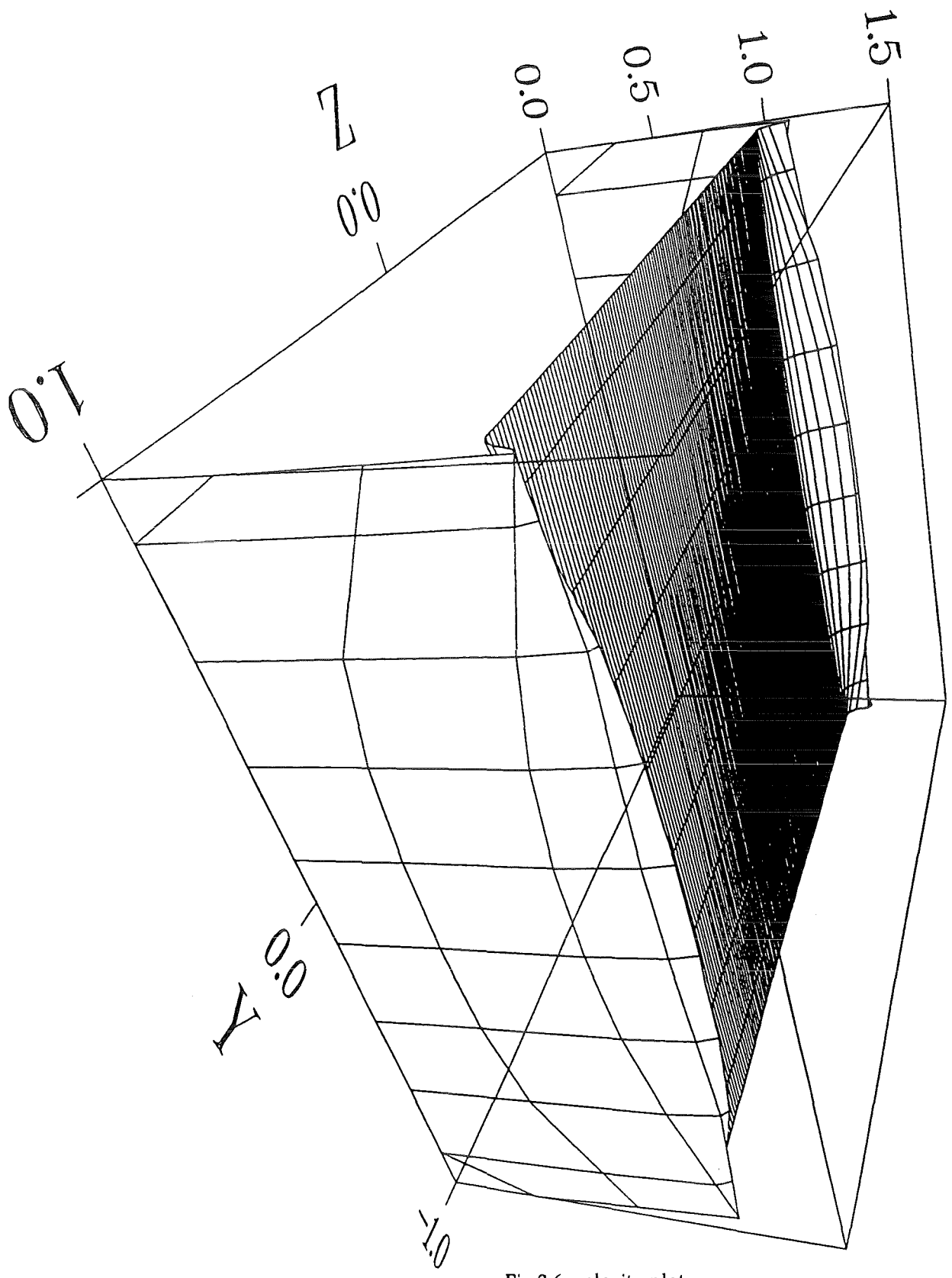


Fig.3.6: velocity plot

4—UNSTABLE FLOW IN A DUCT WITH CONDUCTING STRIPS

4.1—Introduction

In connection with the thermonuclear fusion project the cooling of reactors such as tokamaks by a liquid metal coolant is investigated in various ways. In order to enhance the heat transfer in insulating ducts, a coating of the walls perpendicular to the magnetic field by a pair of electrically conducting strips has been proposed as a turbulence promotor device (Kolesnikov, 1972).

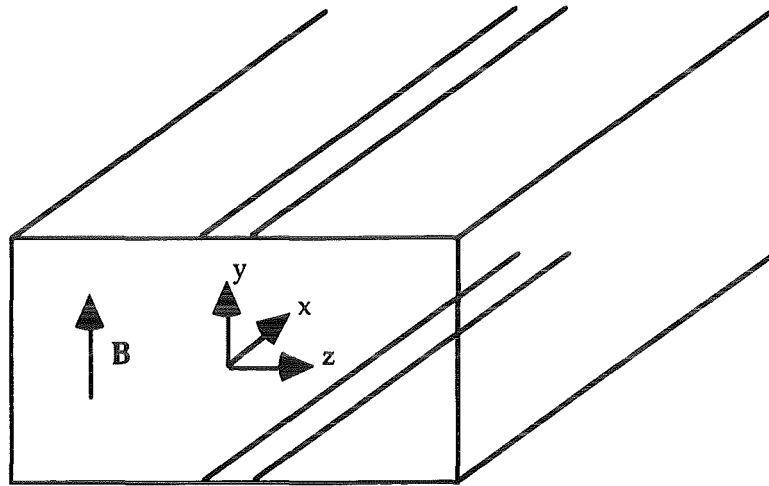


Fig. 4.1

This device has been modelled analytically and numerically as a 2-dimensional system (L. Bühler), and was also investigated experimentally (F. Debray, 1995). The experience was successfully compared with the theory.

This previous work is used to test the 3-D code described in this report. Then, informations about the possible 3-D effects and the influence of the walls parallel to the magnetic field are obtained.

4.2—Flow between two infinite plates with a conducting strip

The 3-D code is first tested for a flow between two plates (no walls parallel to B) and with periodic boundary conditions in the direction of the flow (inlet = outlet). This configuration corresponds to the linear stability analysis and also to some results of the 2-D finite difference code.

The parameters used in the 3-D code are the following:

- Hartmann number based on the channel's half height: 1000
- Hartmann number based on the strip's half width: 100
- aspect ratio = channel's half height/strip's half width: $a_r = 10$
- conductivity of the strip $c_0 = 10^2$ and width $a_r^{-1} = 0.1$.
- insulating Hartmann walls
- size of the grid in x, y, z -directions: $27 \times 16 \times 64$ cells
- computational domain: $0 < x < (\lambda = 0.802)$
 $-1 < y < +1$
 $-1 < z < +1$

A smooth function is actually chosen to resolve the transition between the insulating and conducting parts:

$$c = \frac{c_0}{1 + \left(\frac{\sinh(z)}{\sinh(a_r^{-1})}\right)^6}, \text{ so that } c \rightarrow c_0 = 10^2 \text{ near } z = 0, c \rightarrow 0 \text{ as } z \rightarrow \pm\infty$$

dimensionless numbers are based on the velocity far from the conducting strip and on the half width between the Hartmann walls

Boundary conditions:

- periodic boundary conditions at the inlet $x = 0$ and outlet $x = \lambda$:

v_x, v_y, v_z, Φ at the inlet = v_x, v_y, v_z, Φ at the outlet
 pressure P at inlet = pressure $P - Cst$ at the outlet

- integral treatment of the Hartmann layers at $y = \pm 1$:

$$\frac{\partial^2 v_x}{\partial y^2} = \frac{\partial^2 v_z}{\partial y^2} = 0$$

$$v_y = 0$$

$$\nabla_n \Phi = \nabla_t \cdot ((c + \delta) \nabla_t \Phi)$$

- Neumann boundary conditions at $z = \pm 1$

$$\frac{\partial v_x}{\partial z} = \frac{\partial v_y}{\partial z} = \frac{\partial v_z}{\partial z} = 0$$

$$\frac{\partial \Phi}{\partial z} = \frac{1 + \delta}{1 + c} v_x \approx v_x \text{ so that } \int_{y=-1}^{y=+1} j_z dy = 0$$

These last conditions at $z = \pm 1$ are chosen to give some freedom to the fluid so that the effect of these boundaries is minimum.

The parameters used in the 2-D code are the same except that the computational domain extends to a distance twice as wide in the direction perpendicular to the B-field and to the main flow. The boundary conditions are the same as far as only two directions are concerned with the exception of that of the component of velocity parallel to the side wall.

- Dirichlet & Neumann boundary conditions at $z = \pm 2$: $v_x = 1, \partial v_z / \partial z = 0$
- size of the grid in x, z -directions: 30×80 or 40×100 cells
- computational domain: $0 < x < (\lambda = 0.802)$
 $-2 < z < +2$

profile, and at half way between the Hartmann plates. The two vortices have 3 components. Both sine wave and vortices have a maximum velocity of 10^3 .

Various Reynolds numbers are tried and the flow becomes unstable in the 3-D code at a critical value between 2000 and 2100 if scaled on the half width of the channel (200 and 210 if based on the half width of the strip). In the linear stability analysis and in the 2-D code the critical Reynolds number is 1800 if based on the half width of the channel (180 if based on the half width of the strip).

The following next page shows the flow at a Reynolds number of 4000 scaled on the half width of the channel. The wave length used in this calculation is the same as that of the critical Reynolds number. The instability is not fully developed and the vortices were still growing at that time of the simulation. The vorticity lines are plotted in 2 different planes perpendicular to the magnetic field, the first plane being at half way between the Hartmann plates, the second being close to the lower Hartmann plate. The flow is almost two dimensional although the amplitude of the oscillations is reduced as one moves from the middle to the Hartmann plates, and in the vicinity of these plates, when ones moves from the sides to the strip. The velocity component parallel to the magnetic field remains of the order 10^3 .

10.19.12 FRI 2 JUN, 1995 JOB=ATF320 , KERNFORSCHUNGSZENTRUM - KA DISSPLA 11.0
PLOT 7

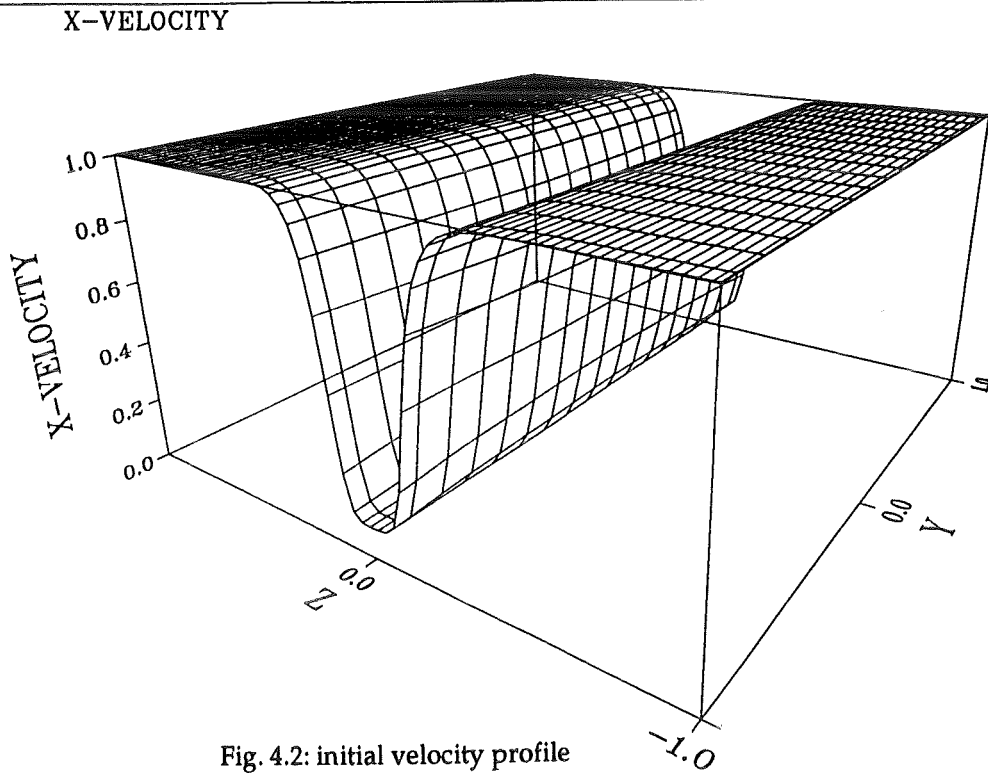
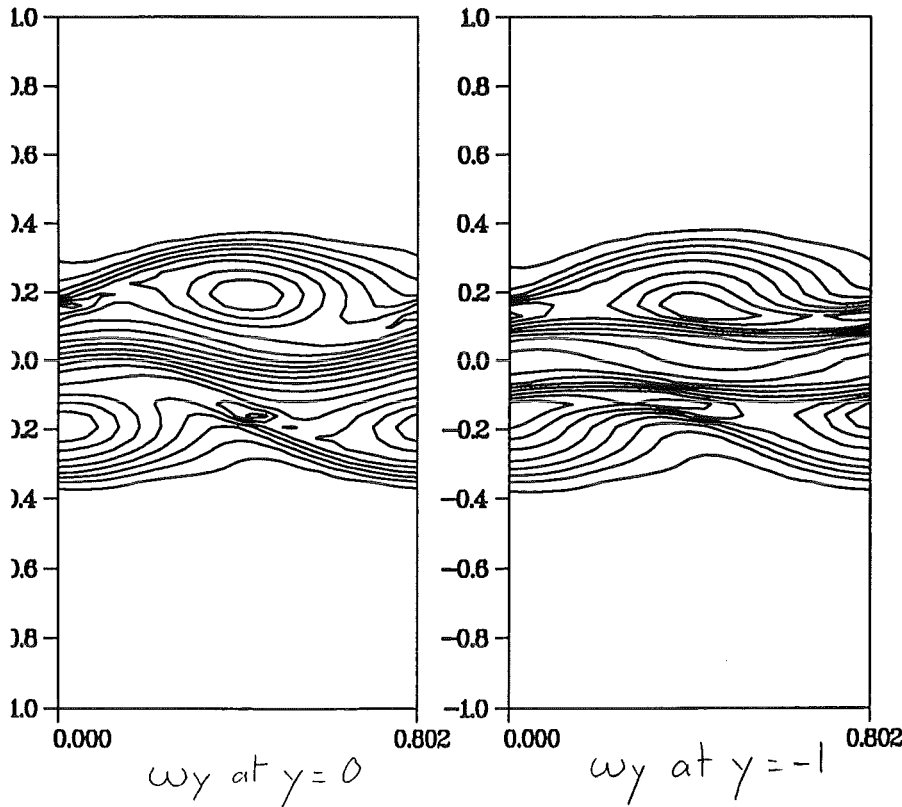


Fig. 4.2: initial velocity profile

02 JUN 1995 10:18 AM BY ATF320

Fig. 4.3: vorticity



21 JUN 1995 2:46 PM BY ATF320

4.3—Slightly unstable flow in a duct with conducting strips

This section and the next one present the results obtained for the same parameter as the experiment performed by F. Debray (1995). It exhibits the interaction of the vortices with the side walls parallel to the B-field.

The parameters of the experiment and its numerical simulation:

- Hartmann number based on the channel's half height: 300
- Interaction parameter based on the channel's half height: 60
- Reynolds number based on the channel's half height: 1500
- Hartmann number based on the strip's half width: 50
- Interaction parameter based on the strip's half width: 10
- Reynolds number based on the strip's half width: 250
- aspect ratio = channel's half height/strip's half width: $a_r = 6$
- conductivity of the strip $c_0 = 4.2 \times 10^{-2}$ and width $a_r^{-1} = 0.167$.
- insulating Hartmann walls and insulating side walls
- size of the grid in x, y, z-directions: $27 \times 16 \times 128$ cells
- computational domain: $0 < x < (\lambda = 1.51)$
 $-2 < y < +2$
 $-1 < z < +1$

Again a smooth function is chosen to resolve the transition between the insulating and conducting parts:

$$c = \frac{c_0}{1 + \left(\frac{\sinh(z)}{\sinh(a_r^{-1})}\right)^6}, \text{ so that } c \rightarrow c_0 = 4.2 \times 10^{-2} \text{ if } z \rightarrow 0, \text{ } c \rightarrow 0 \text{ if } z \rightarrow \pm\infty$$

Boundary conditions:

- periodic boundary conditions at the inlet $x = 0$ and outlet $x = \lambda$:
 v_x, v_y, v_z, Φ at the inlet = v_x, v_y, v_z, Φ at the outlet
 pressure P at inlet = pressure P - Cst at the outlet

- integral treatment of the Hartmann layers at $y = \pm 1$:

$$\frac{\partial^2 v_x}{\partial y^2} = \frac{\partial^2 v_z}{\partial y^2} = v_y = 0, \quad \nabla_n \Phi = \nabla_t \cdot ((c + \delta) \nabla_t \Phi)$$

- No slip conditions and insulating walls at $z = \pm 1$

$$v_x = v_y = v_z = \frac{\partial \Phi}{\partial z} = 0$$

The computation is run until the flow reaches a constant oscillatory regime, i.e. the small instability is fully developed and will not grow further in time. The amplitudes of the oscillation are the following:

v_x max.	v_y max. $\times 10^3$	v_z max. $\times 10^1$
1.00	1.24	0.88

Although the y-component of velocity, i.e. the component parallel to the B-field, remains very small, it is been plotted on the next figures because it is

organised in the following way. It is anti-symmetric with respect to the plane $y=0$, i.e. the mid plane between the Hartmann walls. It is also anti-symmetric with respect to the central x -axis of the duct. This structure has been found as well in all other runs described in this chapter.

The figure 4.7 shows that the perturbation for the y -component of velocity remains in the region of the strong shear layer in between the conducting strips. Although not represented in the next sections, this perturbation arises also in the shear layers of the side walls for the runs described in sections 4.4 and 4.5.

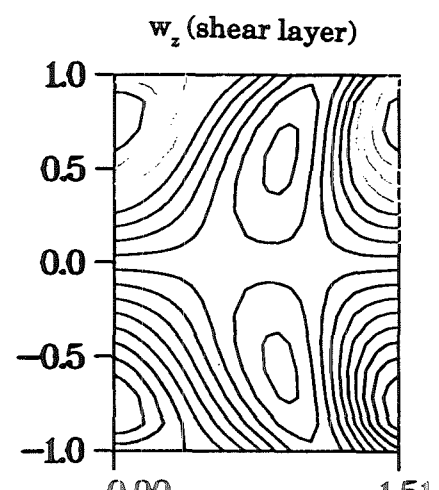
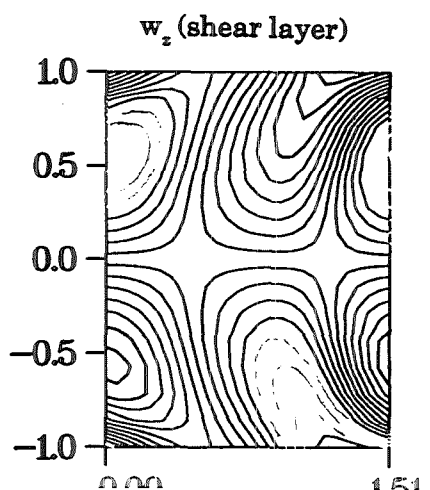
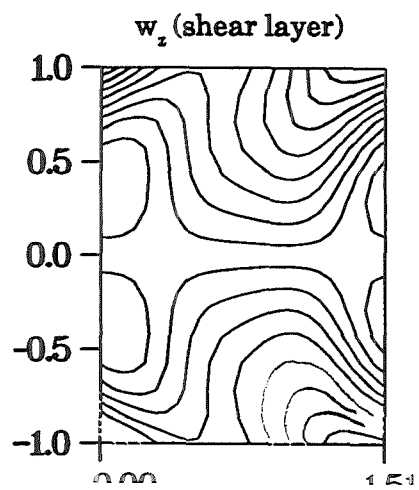
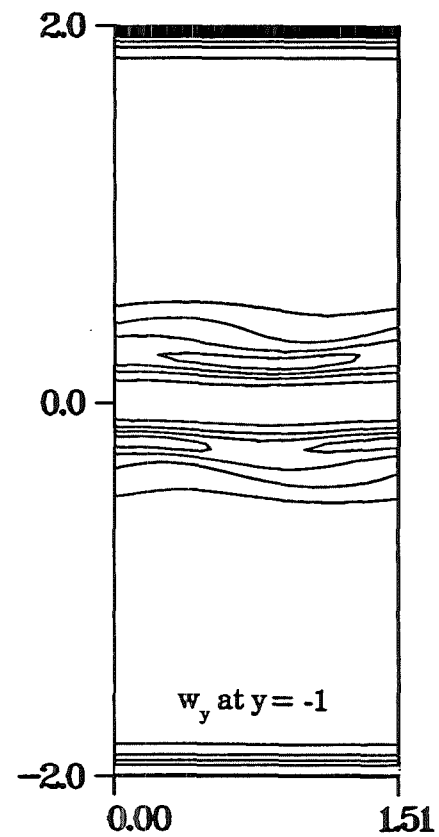
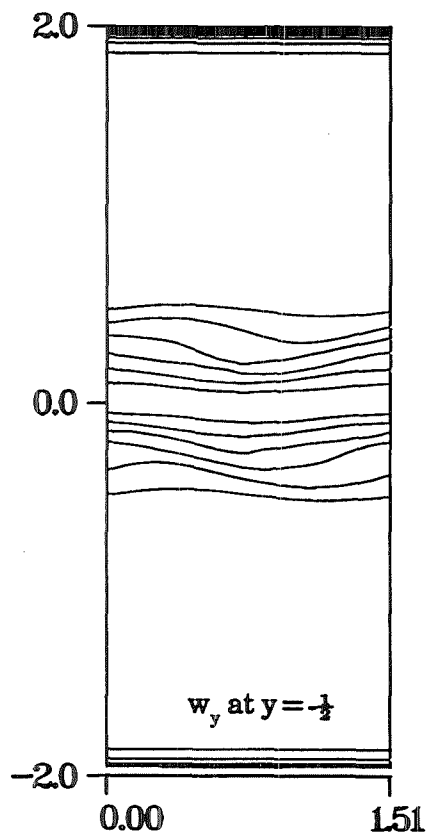
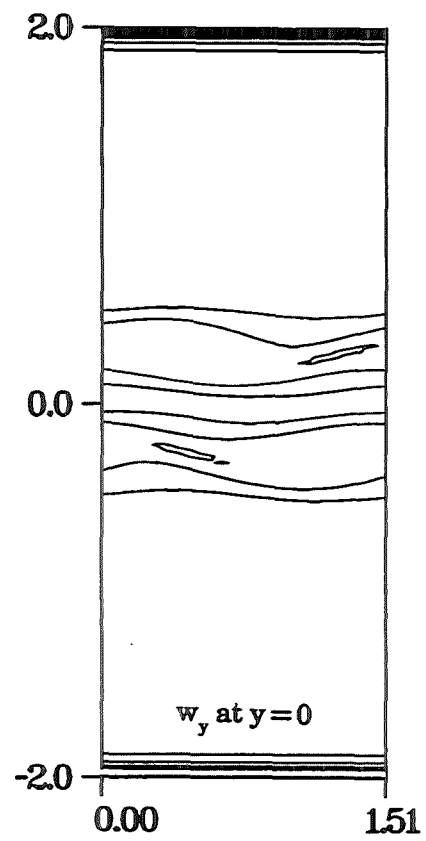


Fig. 4.4: y- and z-components of vorticity

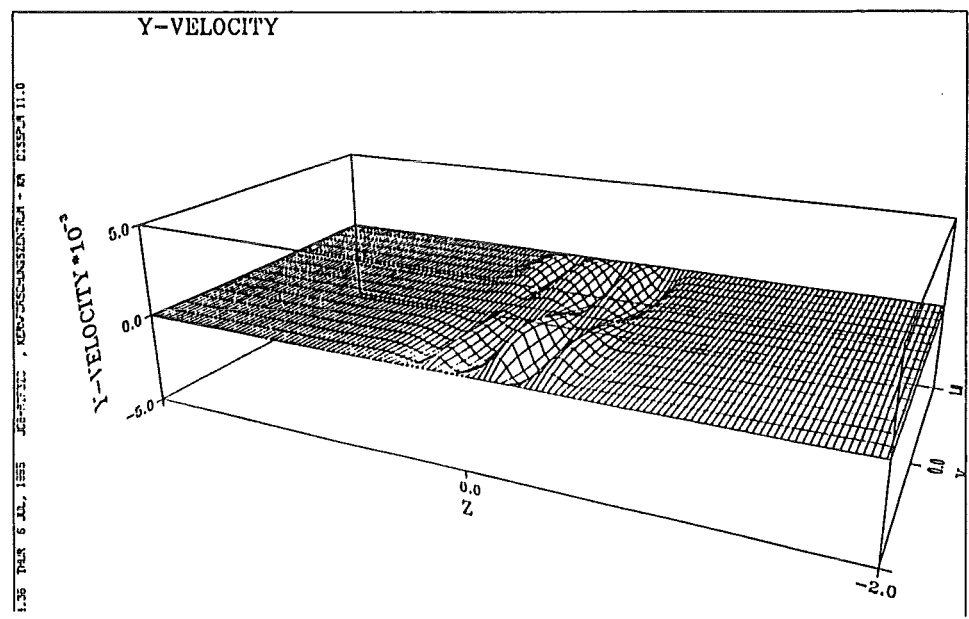
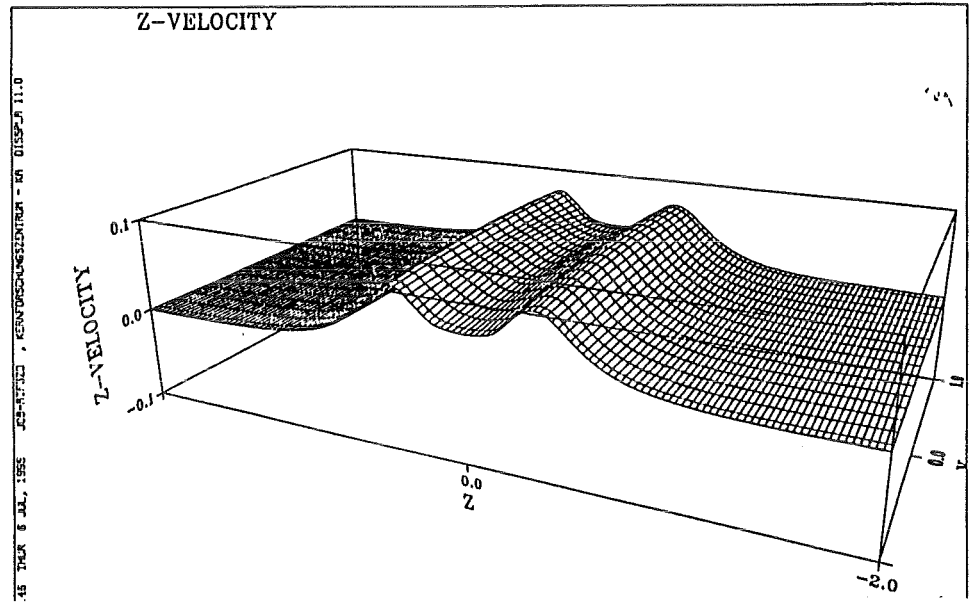
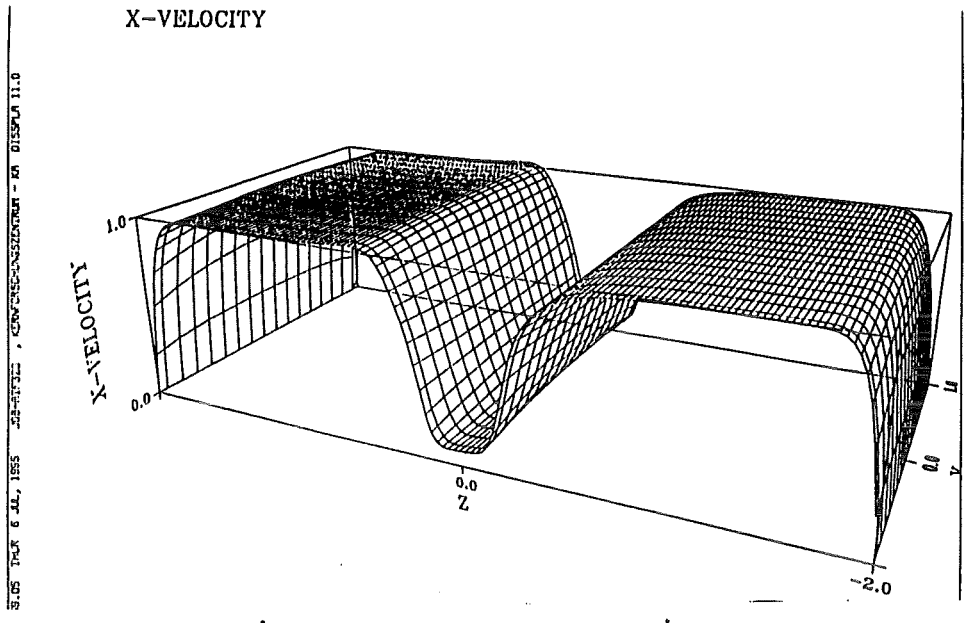
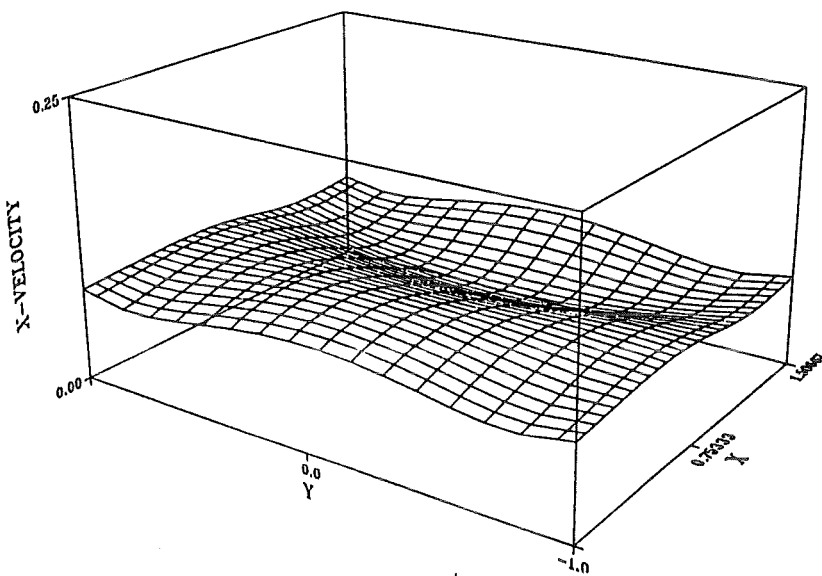


Fig. 4.5: the 3 components of velocity in a cross section of the duct (plane $x = Cst$)

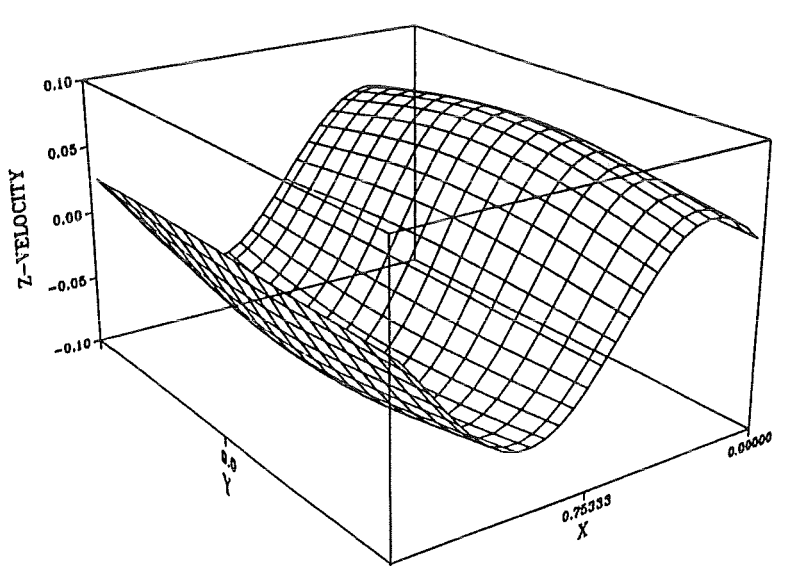
14.05.09 TMR 6 JUL 1955 JOB=PT22 , KENWISCONSIZENTUR - ER DISPLA 11.0

X-VELOCITY



17.05.48 MCD 5 JUL 1955 JOB=PT22 , KENWISCONSIZENTUR - ER DISPLA 11.0

Z-VELOCITY



13.52.31 TMR 6 JUL 1955 JOB=PT22 , KENWISCONSIZENTUR - ER DISPLA 11.0

Y-VELOCITY

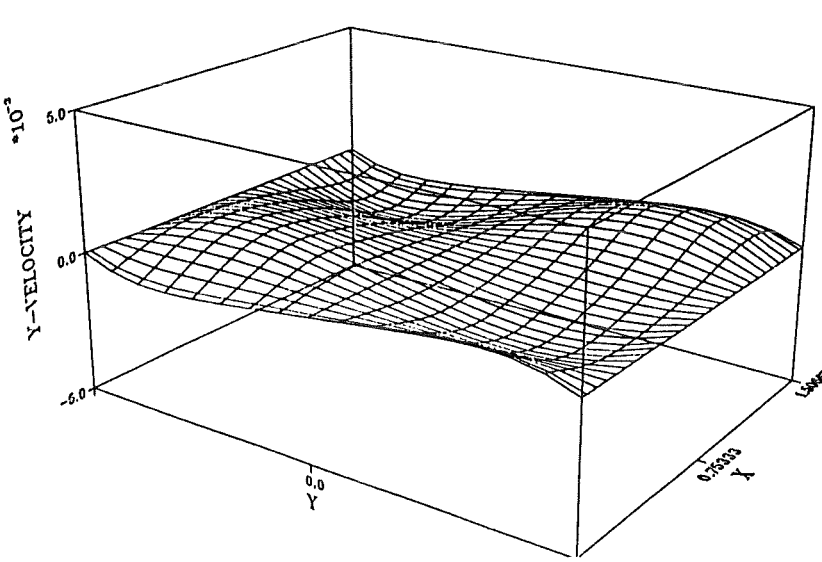


Fig. 4.6: the 3 components of velocity in a plane $z = Cst$

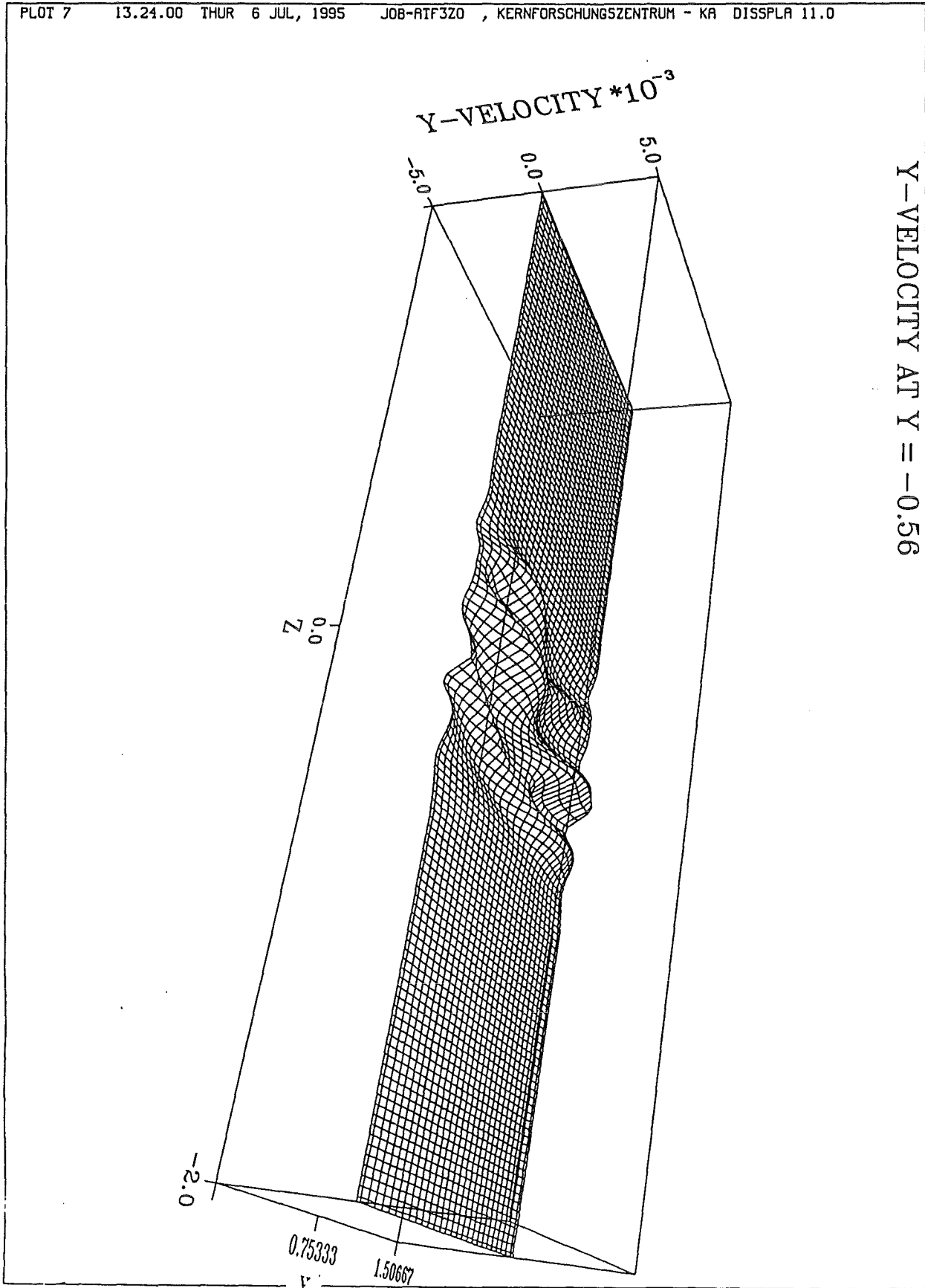


Fig. 4.7: y-component of velocity in a plane $y = Cst$
This component is parallel to the magnetic field and is none zero only in the shear layer

4.4—Strongly unstable flow in a duct with conducting strips

This section uses the same parameters and boundary conditions as those of the previous section describing the experiment. But the Reynolds number is now about twice its previous value, the corresponding interaction parameter being twice as low as before.

- Hartmann number based on the channel's half height: 300
- Interaction parameter based on the channel's half height: 28.96
- Reynolds number based on the channel's half height: 3108
- Hartmann number based on the strip's half width: 50
- Interaction parameter based on the strip's half width: 4.83
- Reynolds number based on the strip's half width: 518
- computational domain: $0 < x < (\lambda = 2.79)$

The dimensionless numbers are now based on the mean velocity that can be deduced from the flow rate. The flow rate is kept constant throughout the simulation. For this purpose, the pressure drop is adapted continuously during the execution of the program.

The following figures show the evolution in time of the flow. The y-vorticity is plotted at $y=0$, $y=-0.5$, $y=-1$. The z-vorticity is plotted in the region of strong shear at $z=-0.39$, $z=-0.45$, $z=-0.51$. This z-vorticity is smaller than the y-vorticity. The y-velocity is of the order 10^2 , while the z-velocity is of the order 1. However the y-velocity is growing as the instability occurring from the strip reaches the side walls. The evolution of the maximum value of each component of the velocity is shown on table 4.1.

time	vx max.	vy max. $\times 10^2$	vz max.
2.5	1.13	0.008	0.01
5.0	1.26	0.44	0.23
7.5	1.45	0.79	0.52
10.0	1.47	0.80	0.46
12.5	1.46	0.84	0.40
15.0	1.50	0.78	0.43
17.5	1.48	0.79	0.40
20.0	1.48	0.86	0.37
22.5	1.65	0.89	0.50
25.0	1.97	1.04	1.18
27.5	2.10	2.66	1.20
30.0	1.65	3.20	1.25

Table 4.1

The flow exhibits the following behaviour:

- the perturbation is rapidly amplified to form vortices around the strip.
- then, these vortices grow relatively slowly compared to the initial small perturbation and develop from the strip to the side walls.
- when they reach the side layers, some new vortices are created and develop from the side layers to the strip
- the vortices occurring from the side walls become stronger than the initial vortices that arose from the strip. At this time the maximum z- velocity changes rapidly from 0.4 to 1.3
- then the whole domain is strongly unstable and the resolution of the simulation becomes too weak.

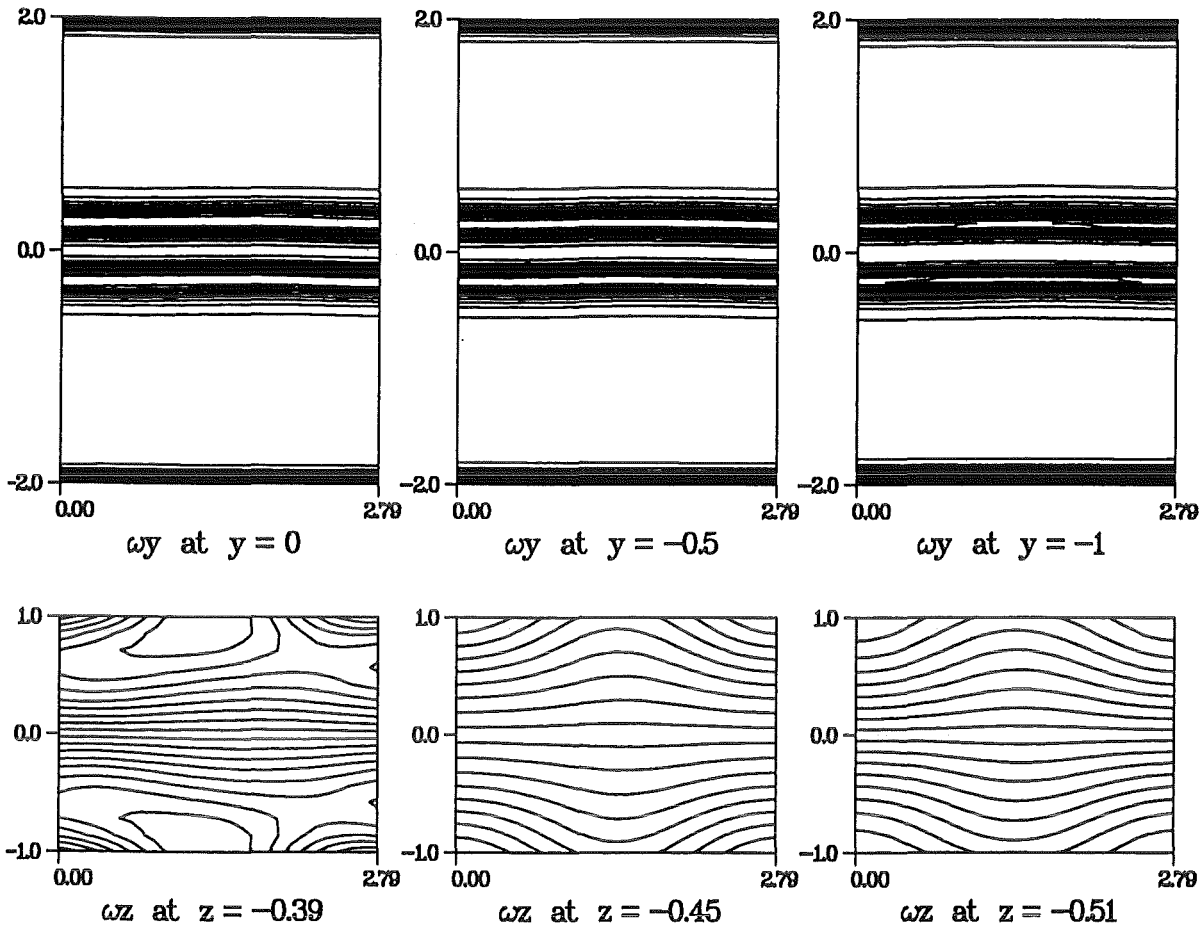
Next to the plot of vorticity are represented some statistics. The 3-D plots on the left represent the evolution of the mean velocity $\langle vx \rangle$. The 3-D plots on the right represent the evolution of the mean value of the x- and z-perturbations product $\langle vx' \times vz' \rangle$. The quantities vx' and vz' are defined as

$$vx = \langle vx \rangle + vx', \quad vz = \langle vz \rangle + vz'$$

The mean value can be considered either as an average in time or as an average in the x-direction of space since the flow is periodic in that direction. One can see that the thickness of the shear layer between the strips is first widened. Then it remains about the same until the perturbation reaches the side layers. From that time, both quantities $\langle vx \rangle$ and $\langle vx' \times vz' \rangle$ change rapidly.

time = 2.5

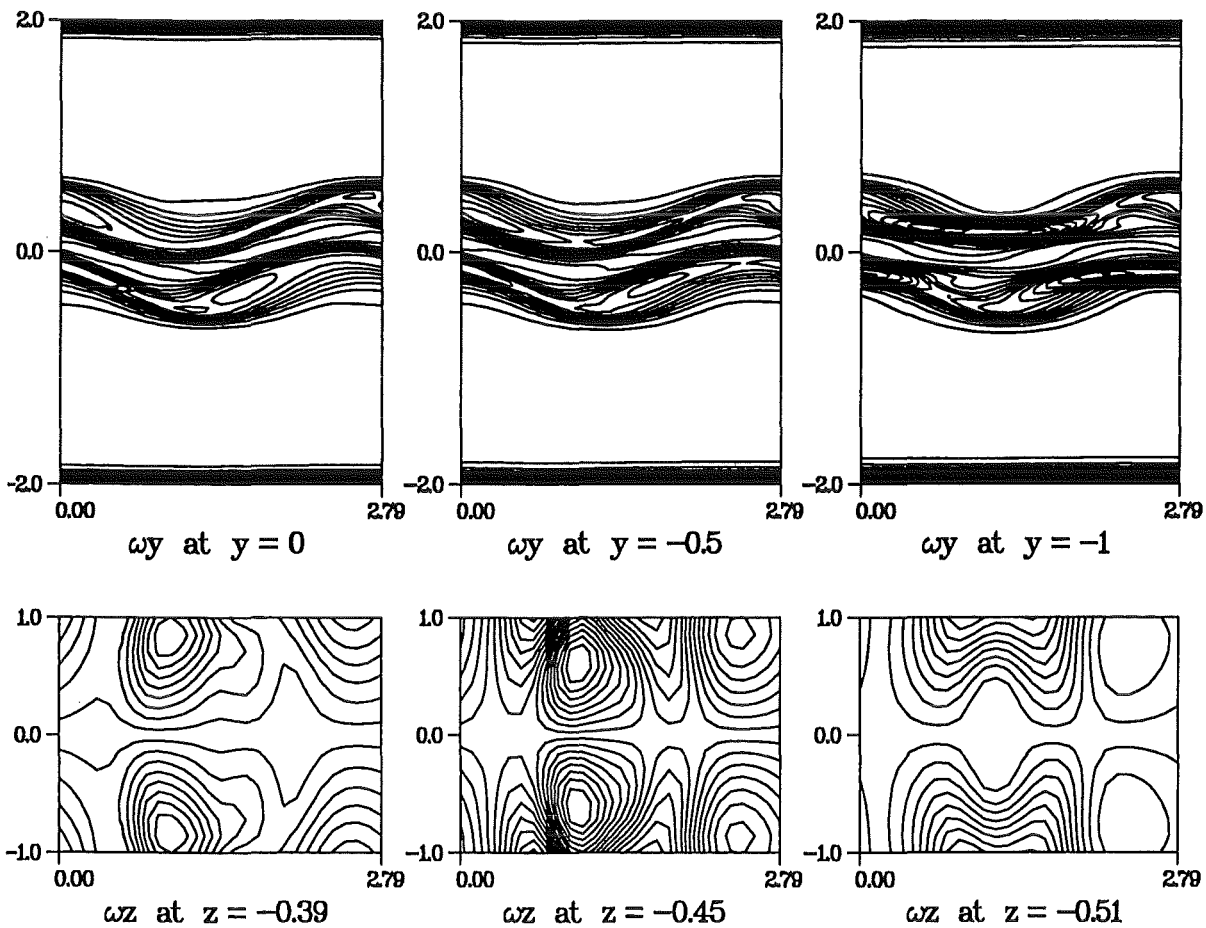
50 ωy -isolines and 18 ωz -isolines



AUG 1985 11:04 PM BY ATF328

time = 5.0

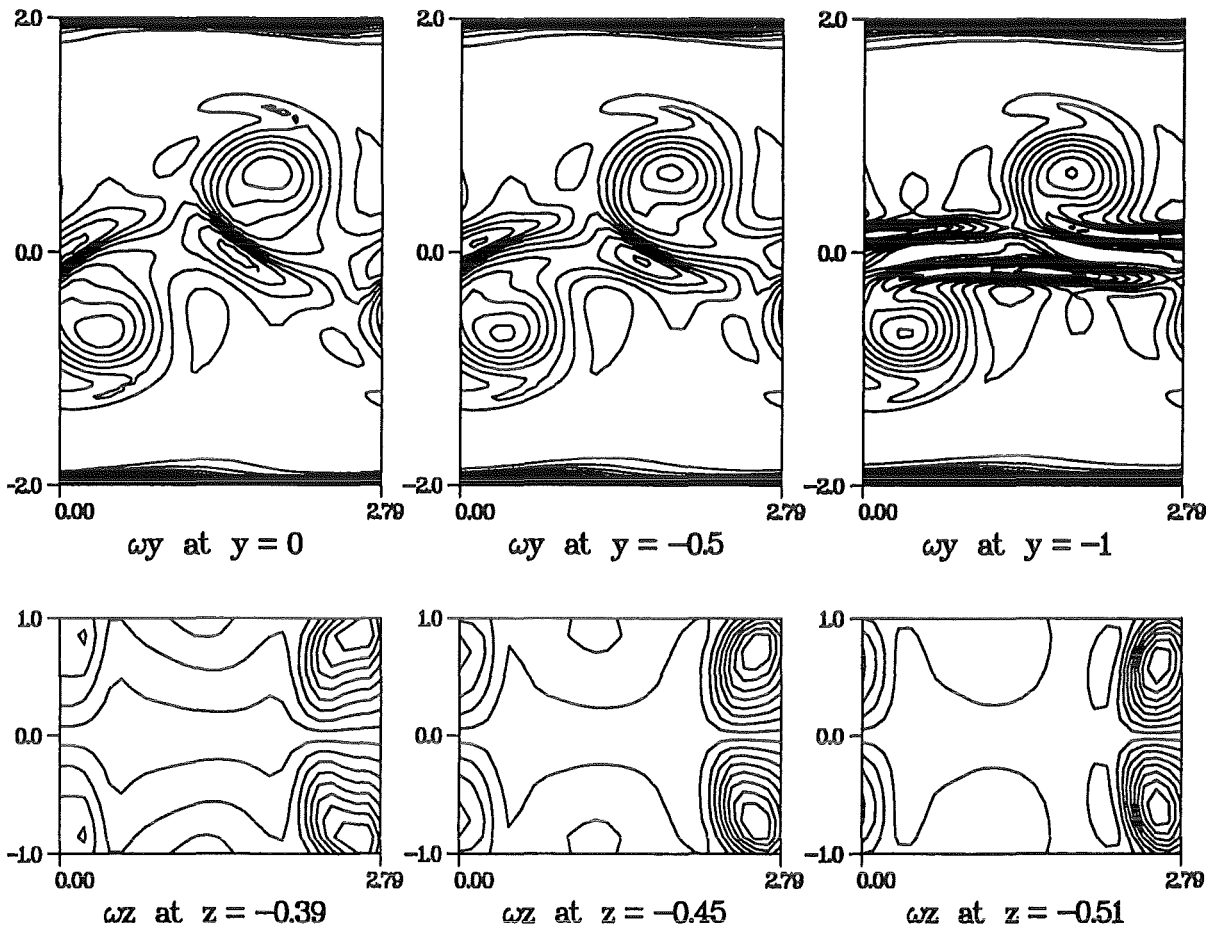
50 ωy -isolines and 18 ωz -isolines



AUG 1985 11:38 PM BY ATF328

time = 7.5

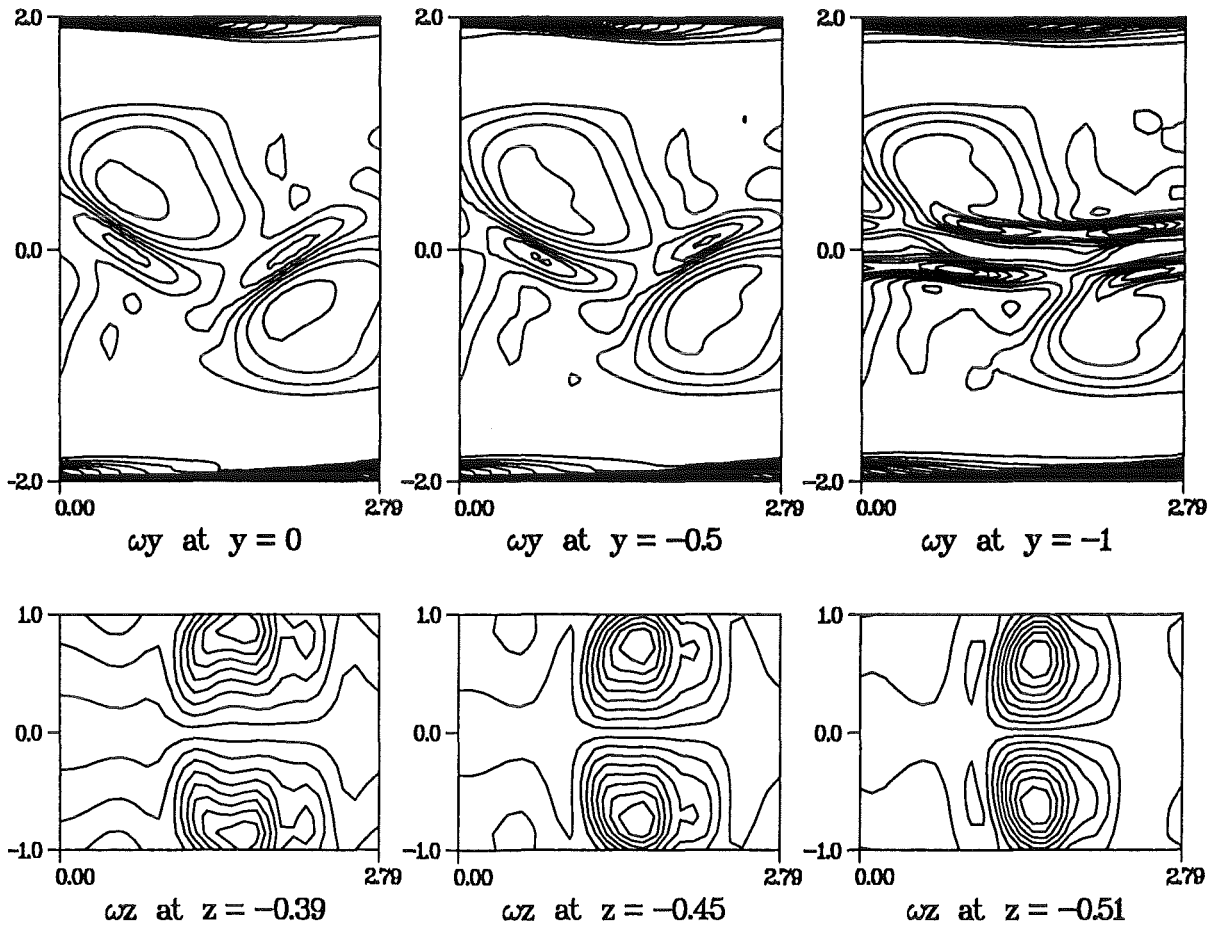
50 ωy -isolines and 18 ωz -isolines



83 AUG 1985 11:14 PM BY ATF3Z8

time = 10.0

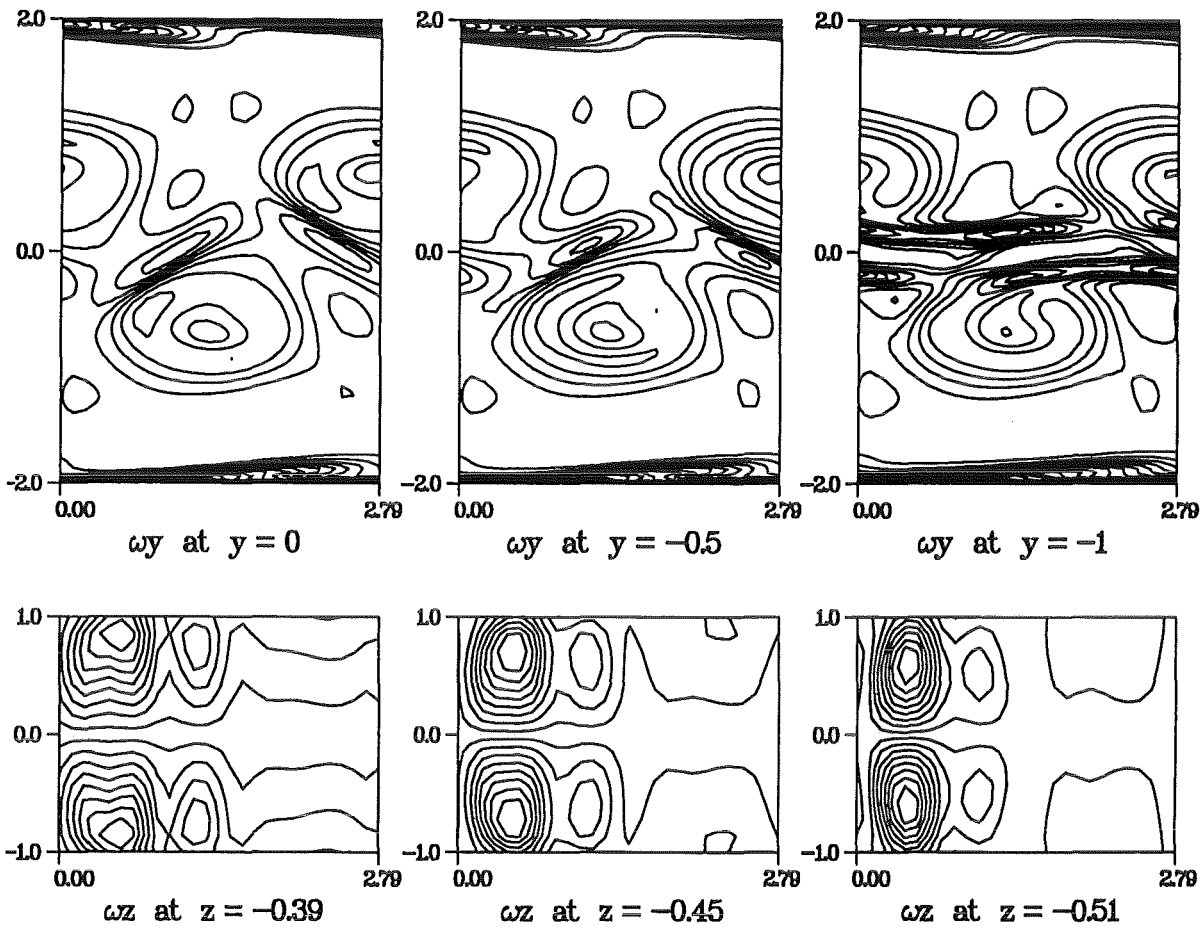
50 ωy -isolines and 18 ωz -isolines



83 AUG 1985 11:12 PM BY ATF3Z8

time = 12.5

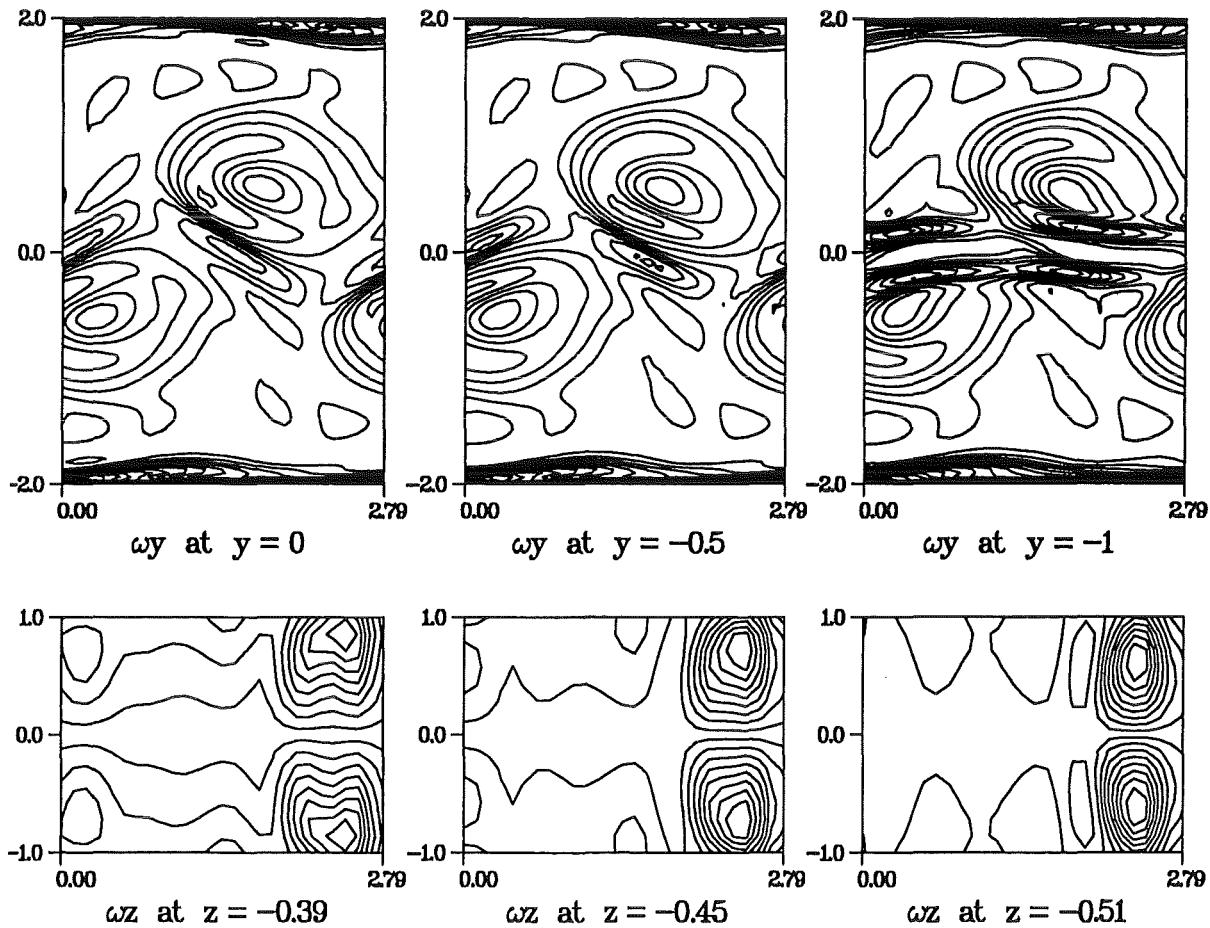
50 ω_y -isolines and 18 ω_z -isolines



AUG 1985 11:02 PM BY ATF328

time = 15.0

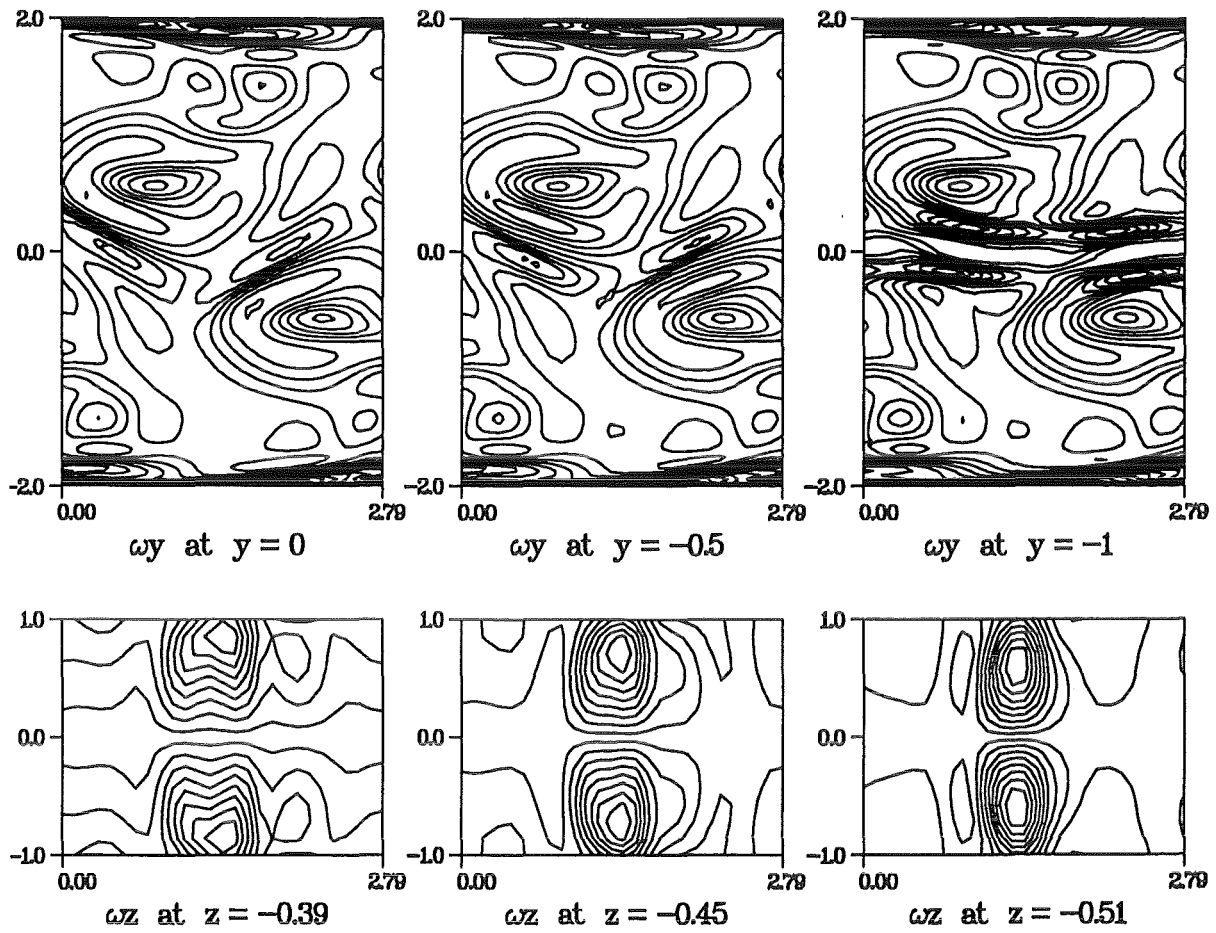
50 ω_y -isolines and 18 ω_z -isolines



AUG 1985 11:41 PM BY ATF328

time = 17.5

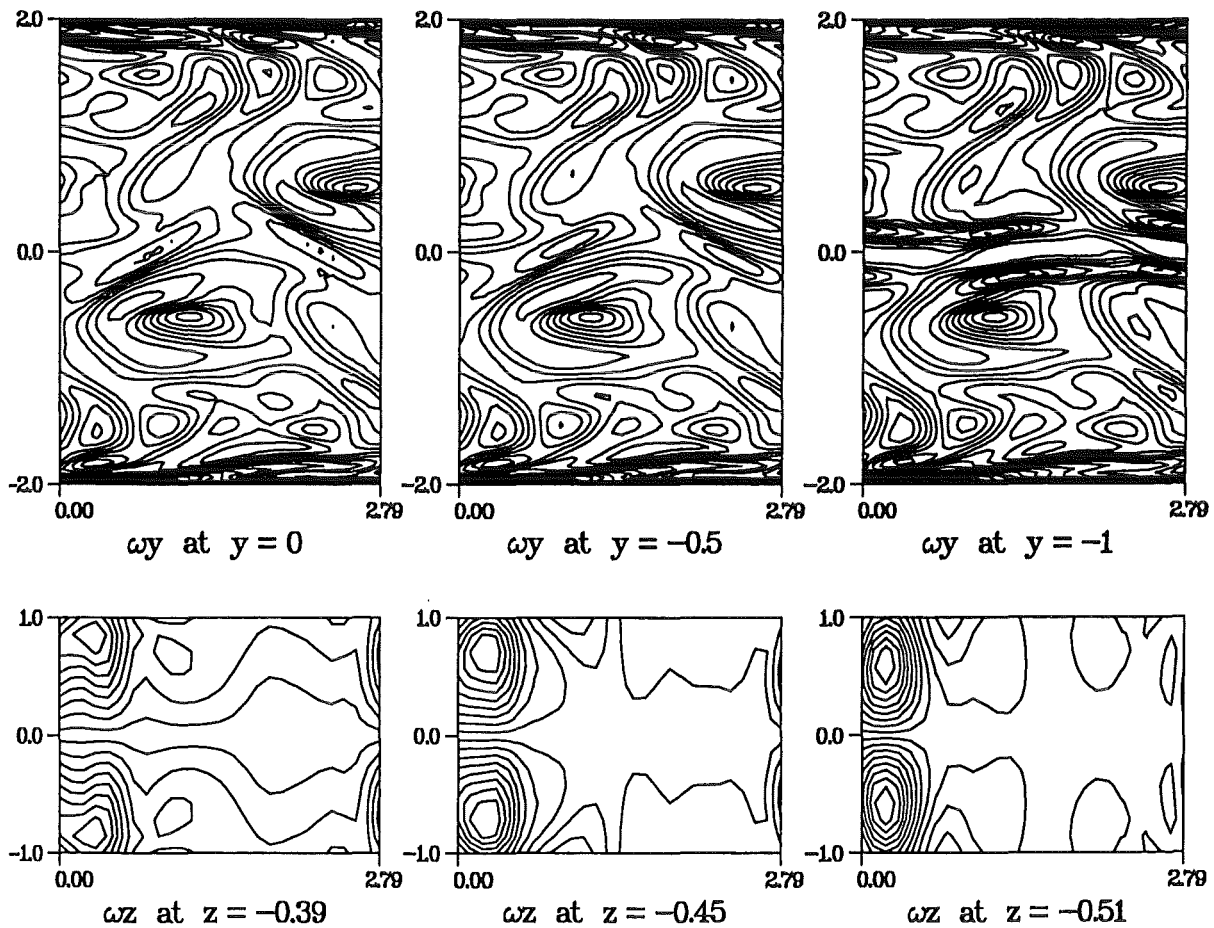
50 ωy -isolines and 18 ωz -isolines



83 AUG 1985 11:55 PM BY ATF328

time = 20.0

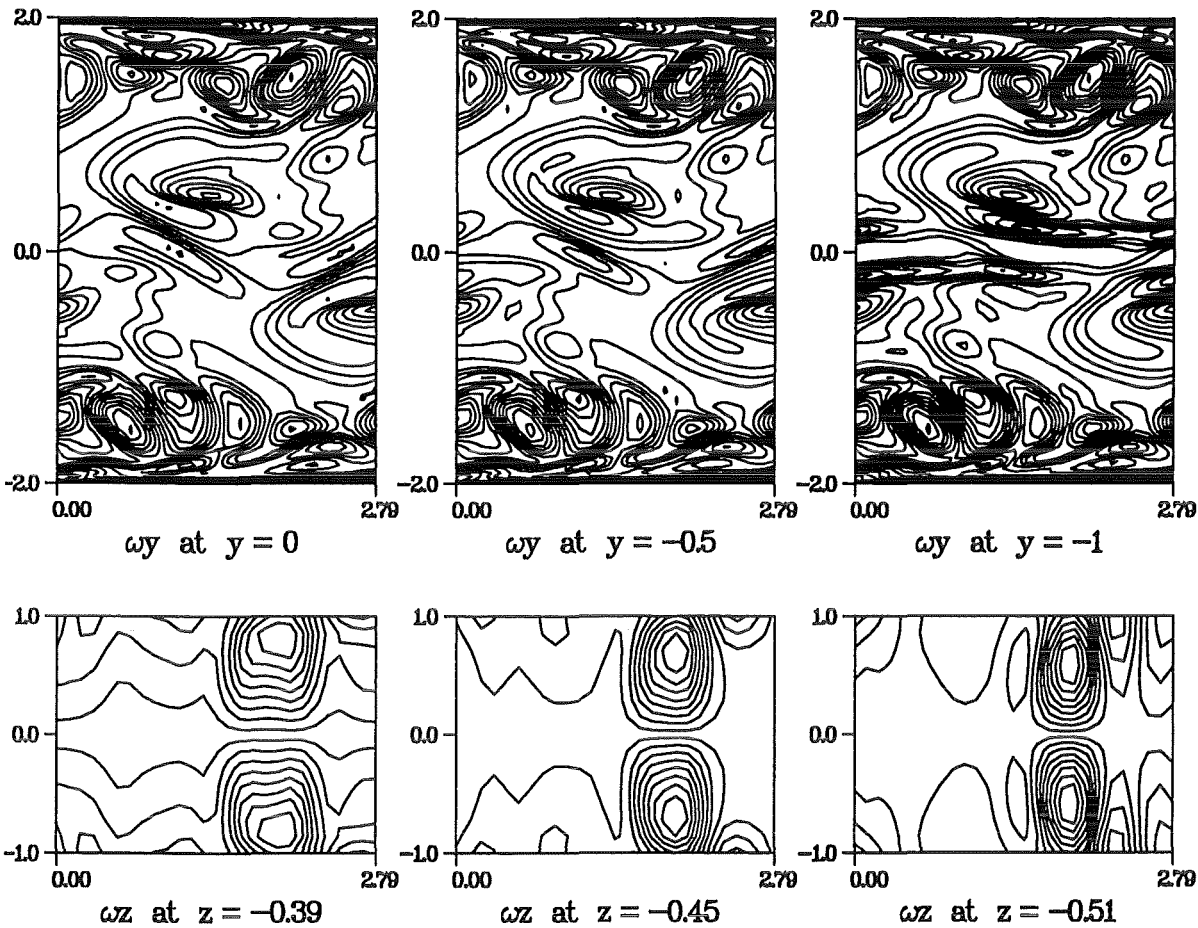
50 ωy -isolines and 18 ωz -isolines



83 AUG 1985 18:48 PM BY ATF328

time = 22.5

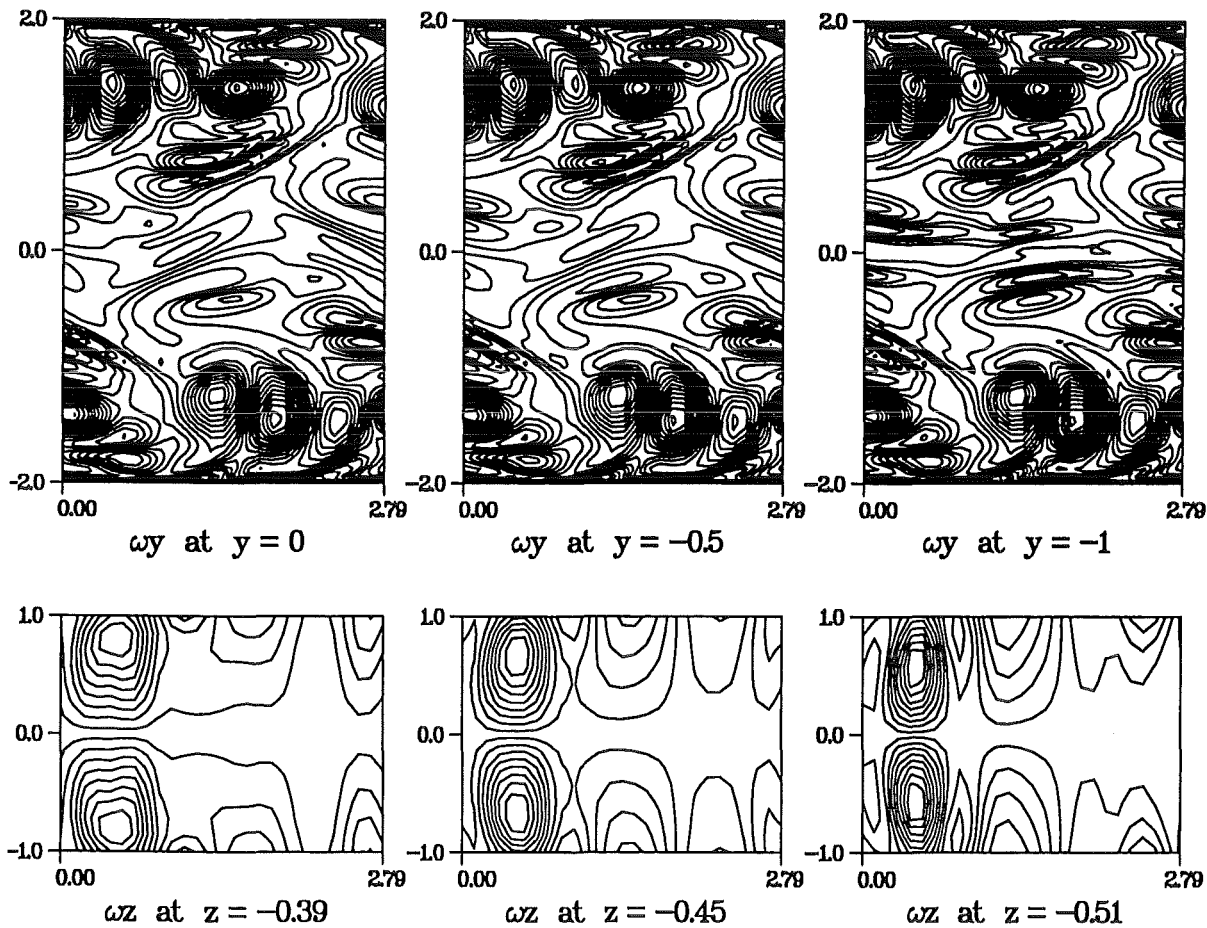
40 ωy -isolines and 18 ωz -isolines



AUG 1985 11:48 PM BY ATF328

time = 25.0

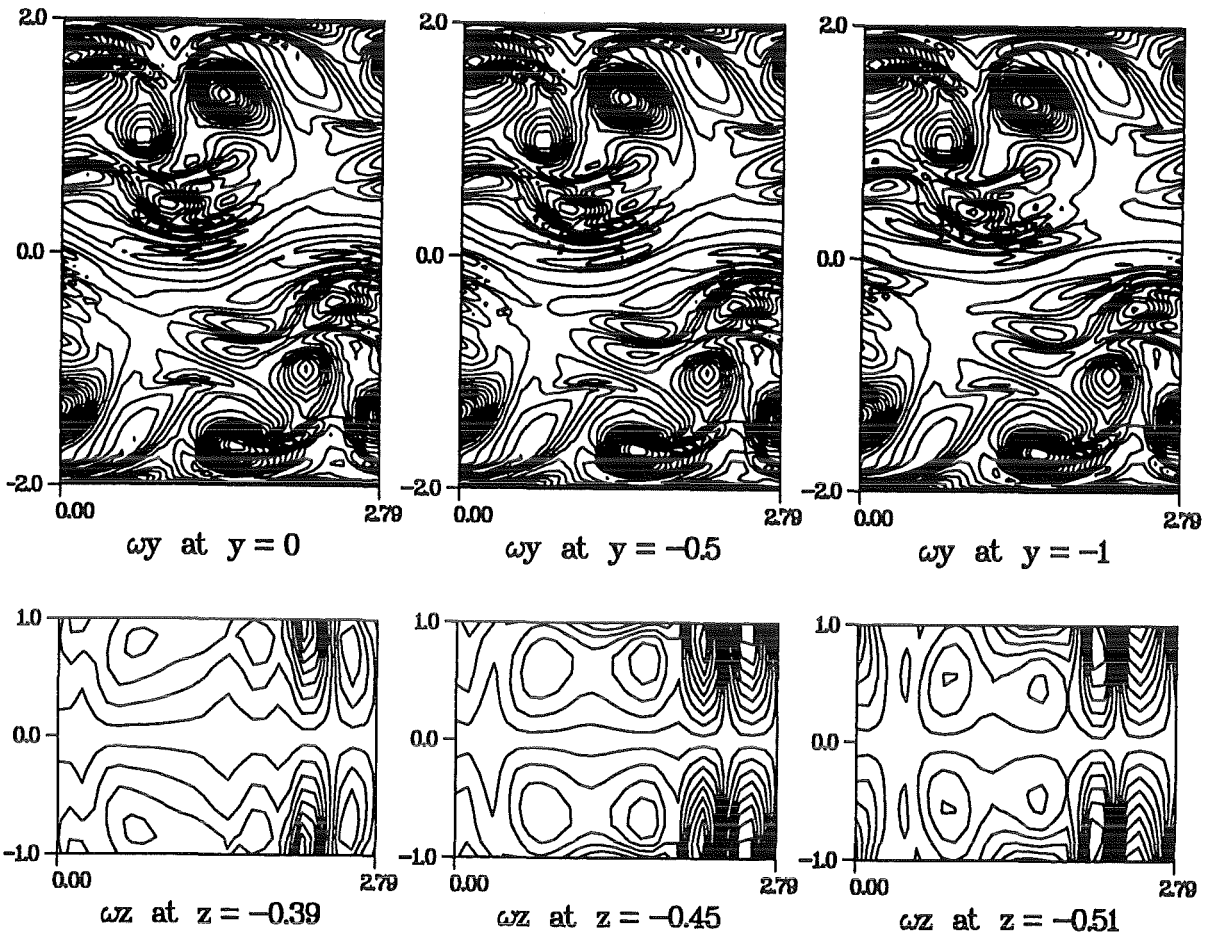
30 ωy -isolines and 18 ωz -isolines



AUG 1985 10:52 PM BY ATF328

time = 27.5

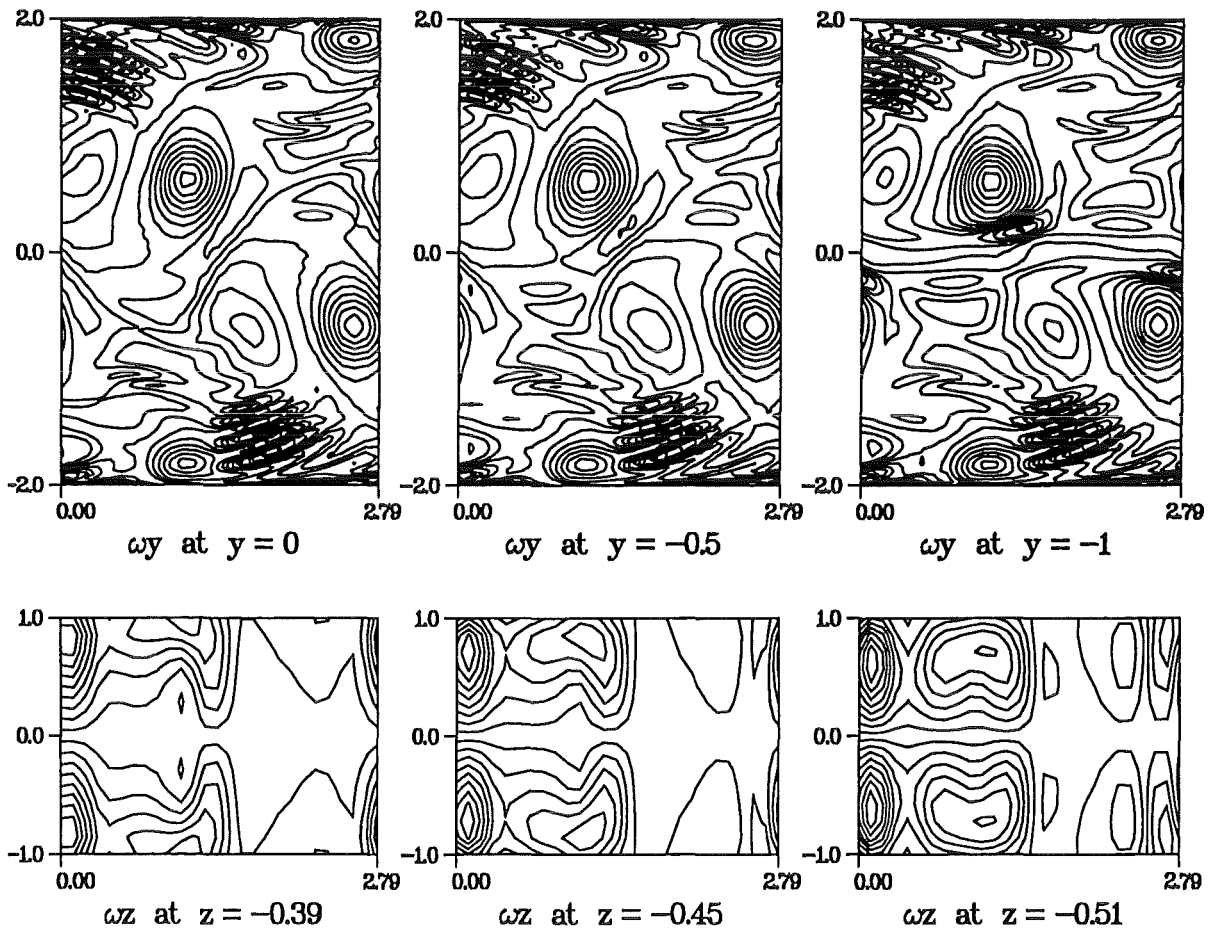
30 ω_y -isolines and 18 ω_z -isolines



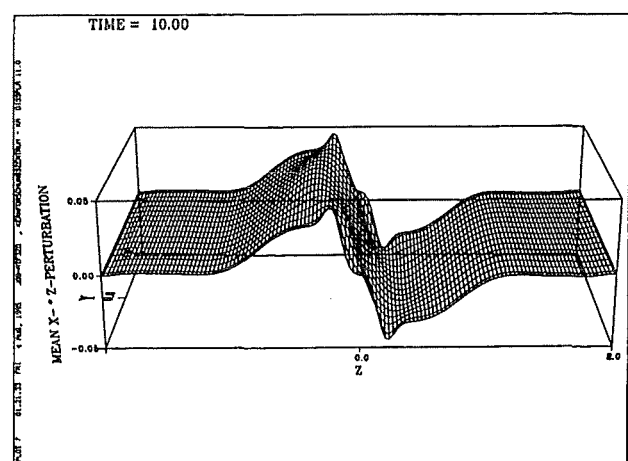
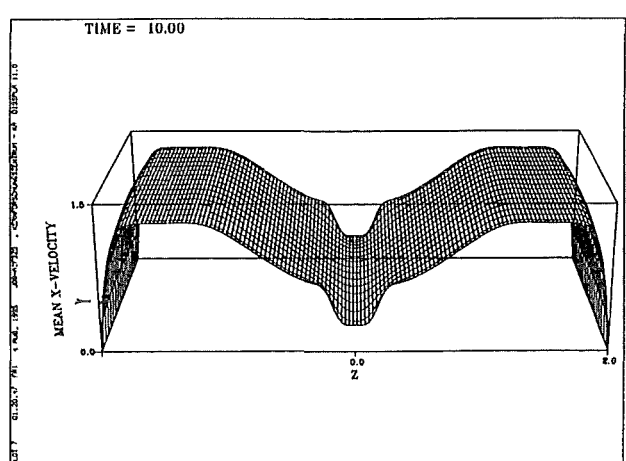
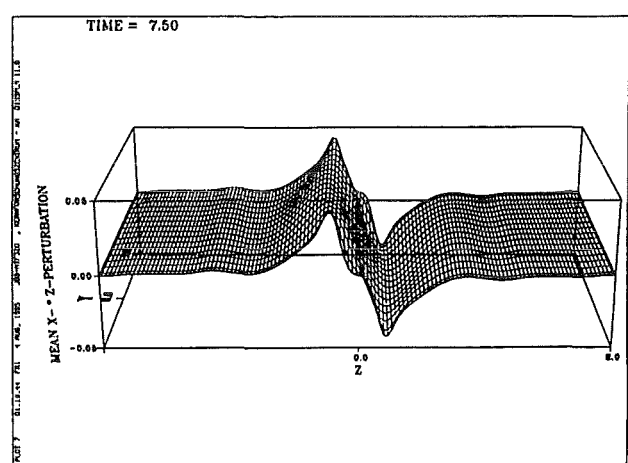
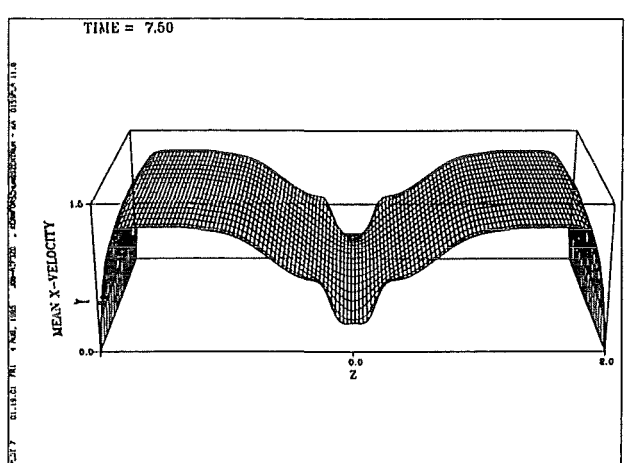
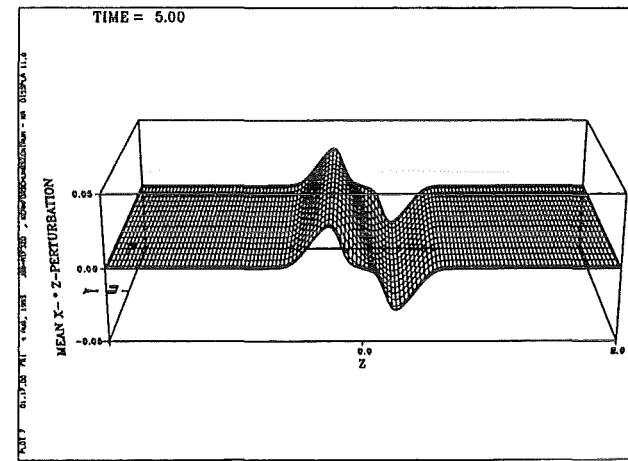
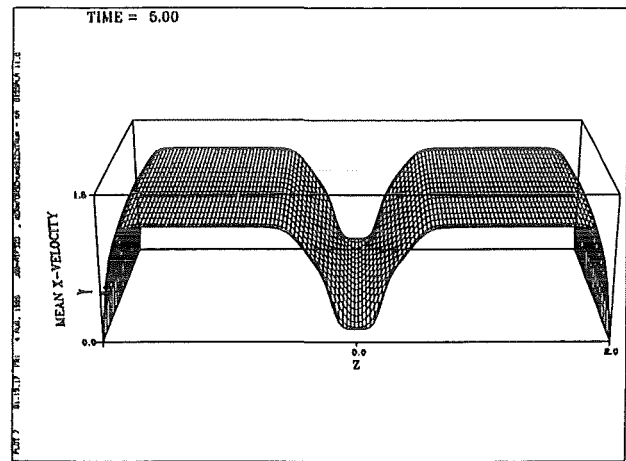
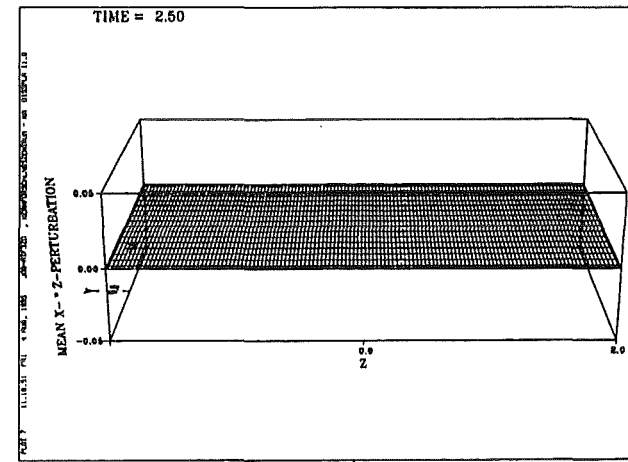
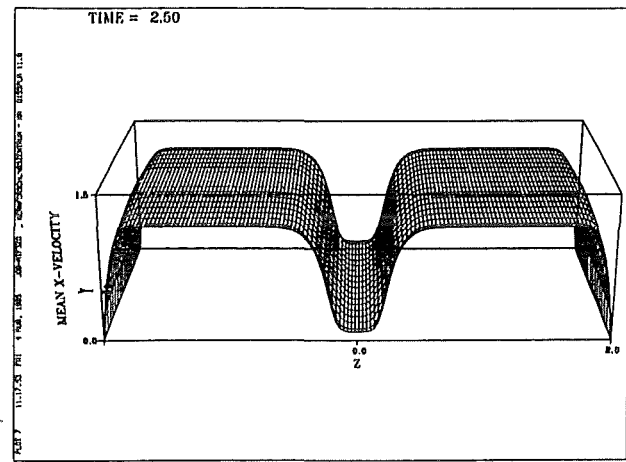
03 AUG 1985 11:52 PM BY ATF3ZB

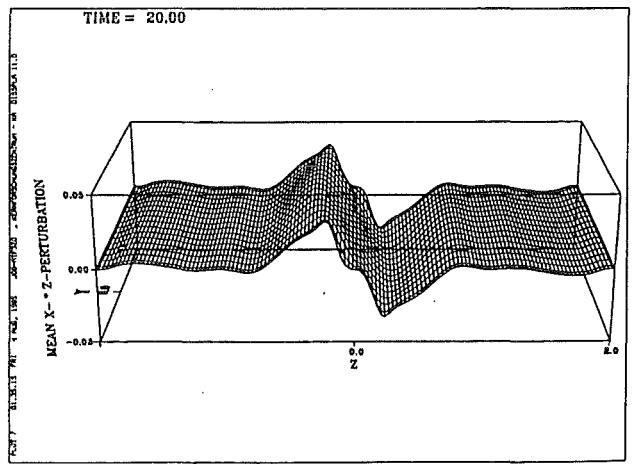
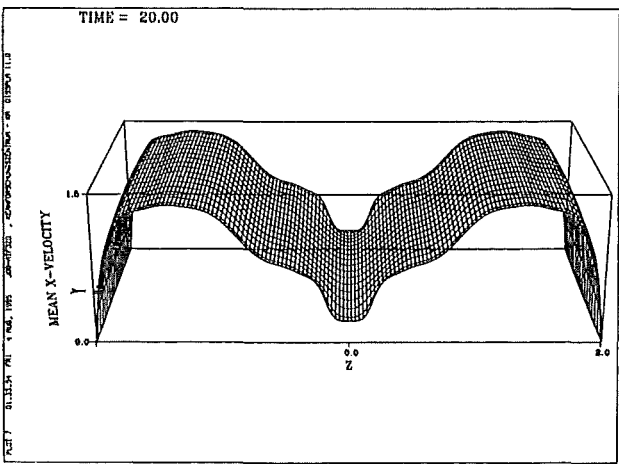
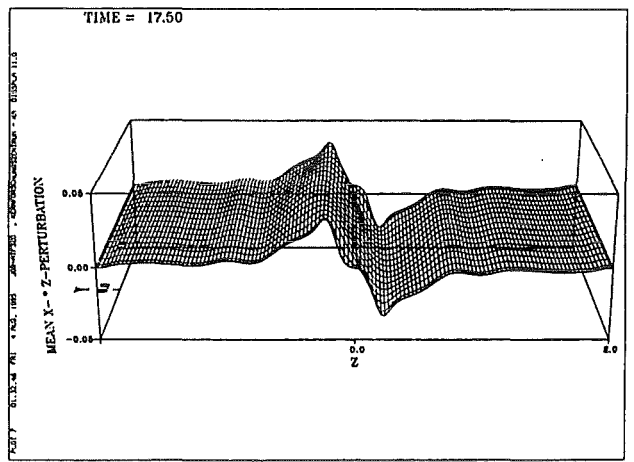
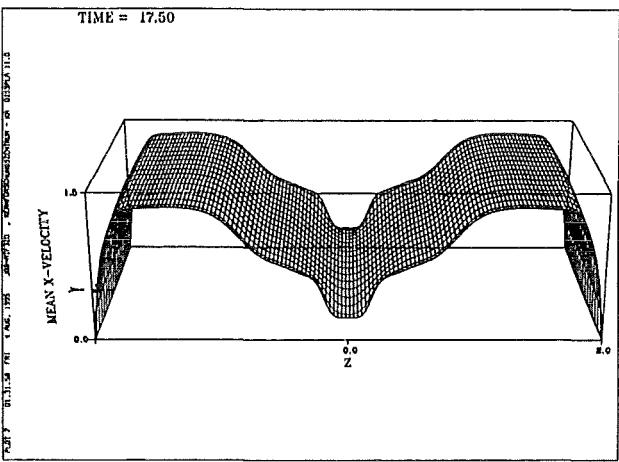
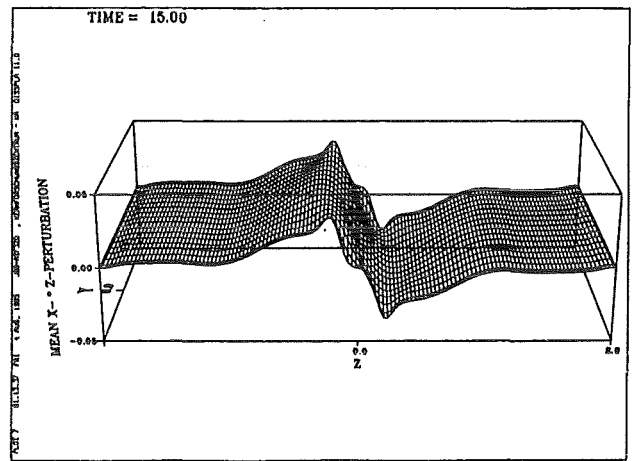
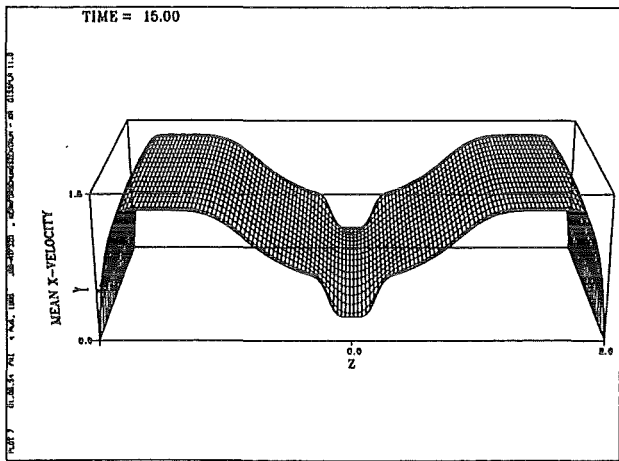
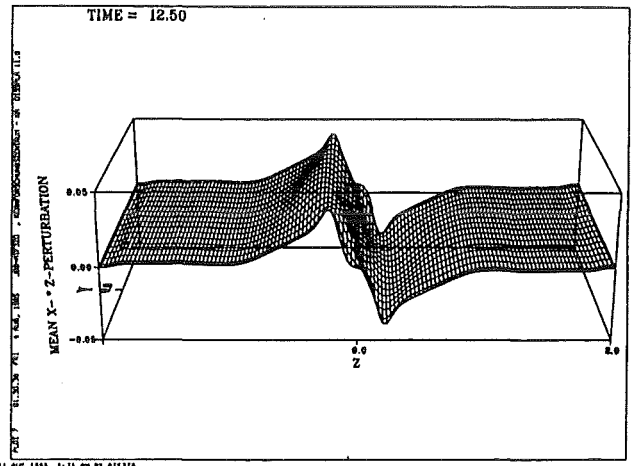
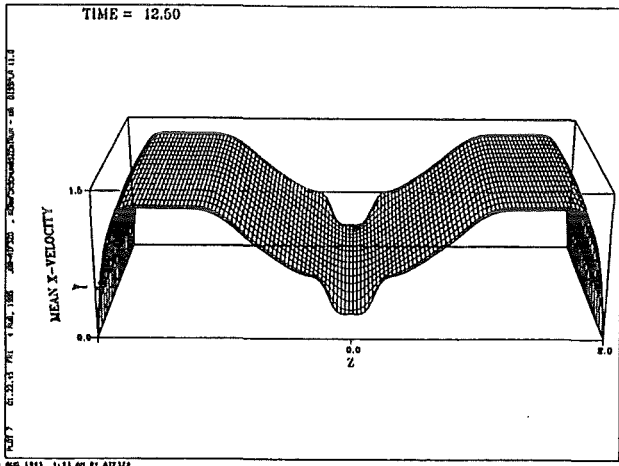
time = 30.0

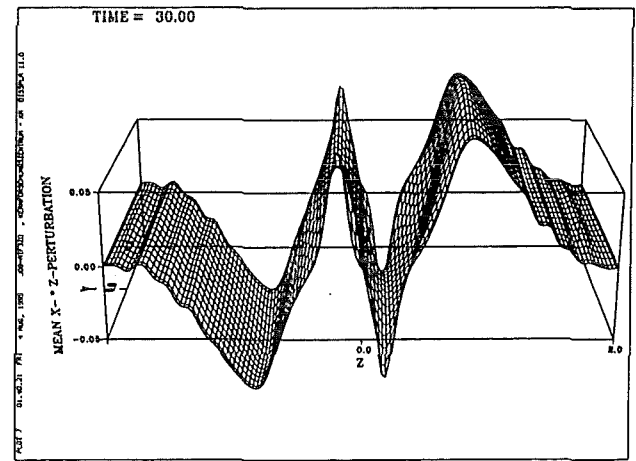
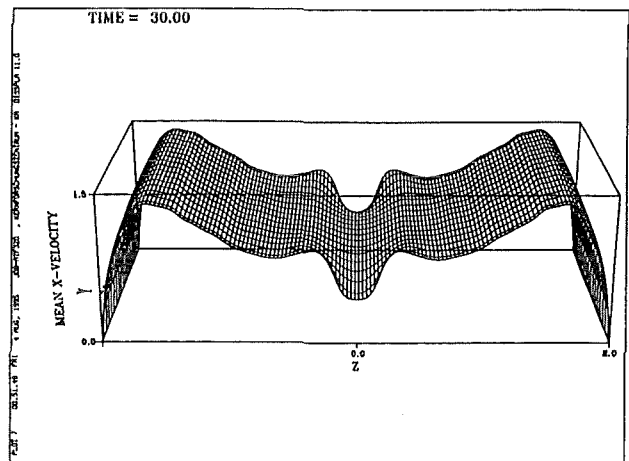
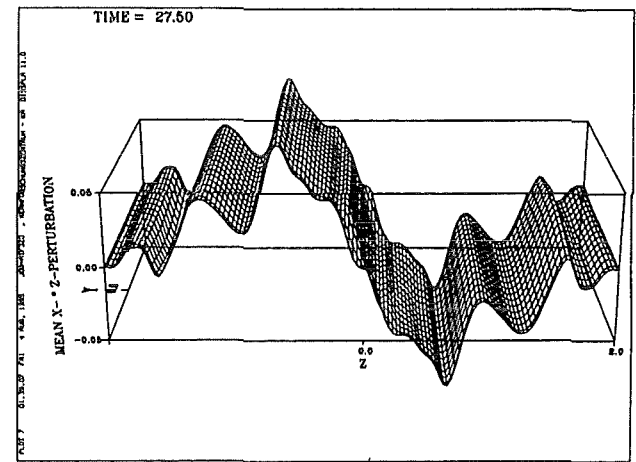
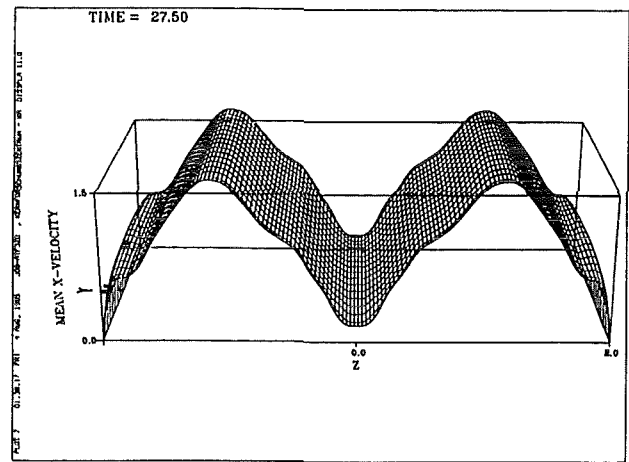
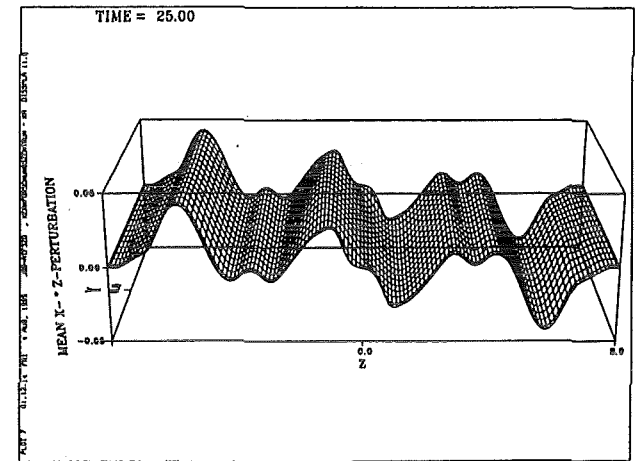
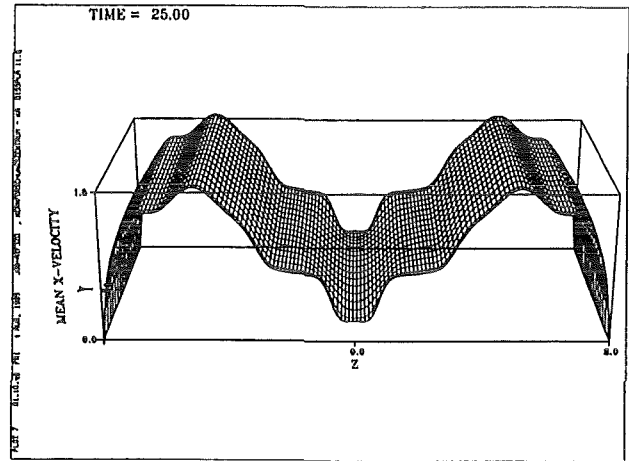
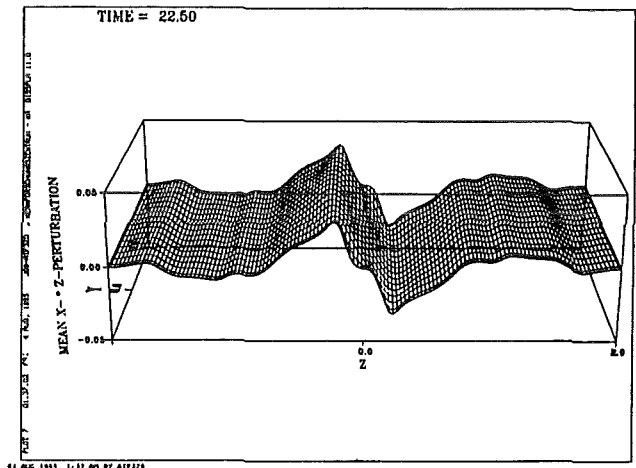
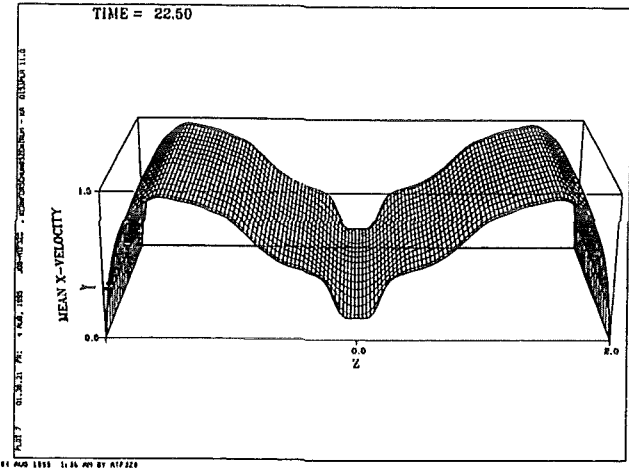
30 ω_y -isolines and 18 ω_z -isolines



03 AUG 1985 10:57 PM BY ATF3ZB







4.5—Unstable flow in a duct with all walls insulating

An important point is that in the simulation presented in the last section, the side layers are unstable very soon and that the vortices coming from the strip enhance the instability of the side layers. It would be interesting to know if the flow is still unstable in case where there are no conducting strips. In order to answer this question, the same simulation is run without the conducting strips. The problem of this run is to choose the length of the domain. This length fixes the wave length and there is no experimental data in that case. Although this parameter is unknown, the run has nevertheless been performed with the wave length of the previous simulation, as first attempt to model this flow.

- Hartmann number based on the channel's half height: 300
- Interaction parameter based on the channel's half height: 28.96
- Reynolds number based on the channel's half height: 3108
- computational domain: $0 < x < (\lambda = 2.79)$

The initial perturbation is again composed of a sine wave of z-velocity extending to the whole domain. It also contains a 'Dirac' of vortex in each shear layer, but the shear layers are now located at the side walls. The two vorticities have 3 components. Both sine wave and vorticities have a maximum velocity of of 10^3 . The perturbation needs a much longer time than in the previous section, in order to be amplified as indicated on the next plots, and on the table below.

The following figures show the evolution in time of the flow. The y-vorticity is plotted again at $y=0$, $y=-0.5$, $y=-1$. The z-vorticity is plotted in the region of strong shear which are now the side layers. This z-vorticity is plotted at $z=-1.77$, $z=-1.83$, $z=-1.89$. It is again smaller than the y-vorticity. There is now almost no 3-D effect since nothing special happens at the Hartmann walls where the conducting strips have been removed.

time	vx max.	vy max. $\times 10^2$	vz max.
52.5	1.07	0.03	0.133
55.0	1.09	0.06	0.217
57.5	1.18	0.12	0.330
60.0	1.40	0.10	0.505
62.5	1.60	0.31	0.620
65.0	1.66	0.79	0.641
67.5	1.61	0.33	0.536
70.0	1.66	0.51	0.524

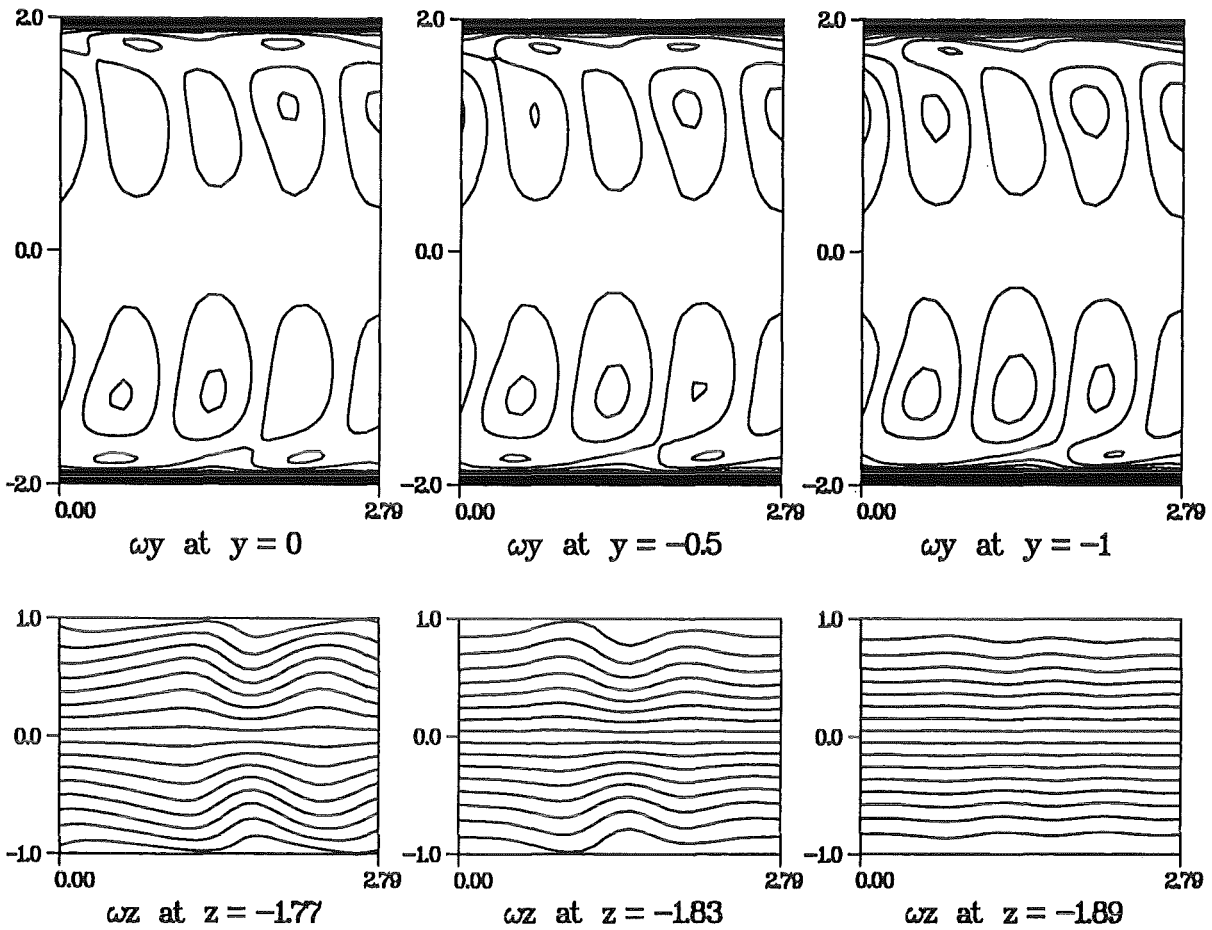
Table 4.2

As shown on the following plots of vorticity and statistics, the flow exhibits the following behaviour:

- at the beginning, the vortices are located close to the side walls, and extend to the bulk of the flow, but there is a quiet region in the middle of the duct.
- the wave length of the perturbation is half the length of the computation domain in the axial direction.
- later, the vortices coming from a side wall meet the vortices coming from the opposite side wall.
- at this stage, the vortices mix together and form a larger structure with a wave length equal to the length of the domain.
- at the end of the run, the flow has not reached a final state, but the amplitude of the oscillation seems to decrease as shown on table 4.2.

time = 52.5

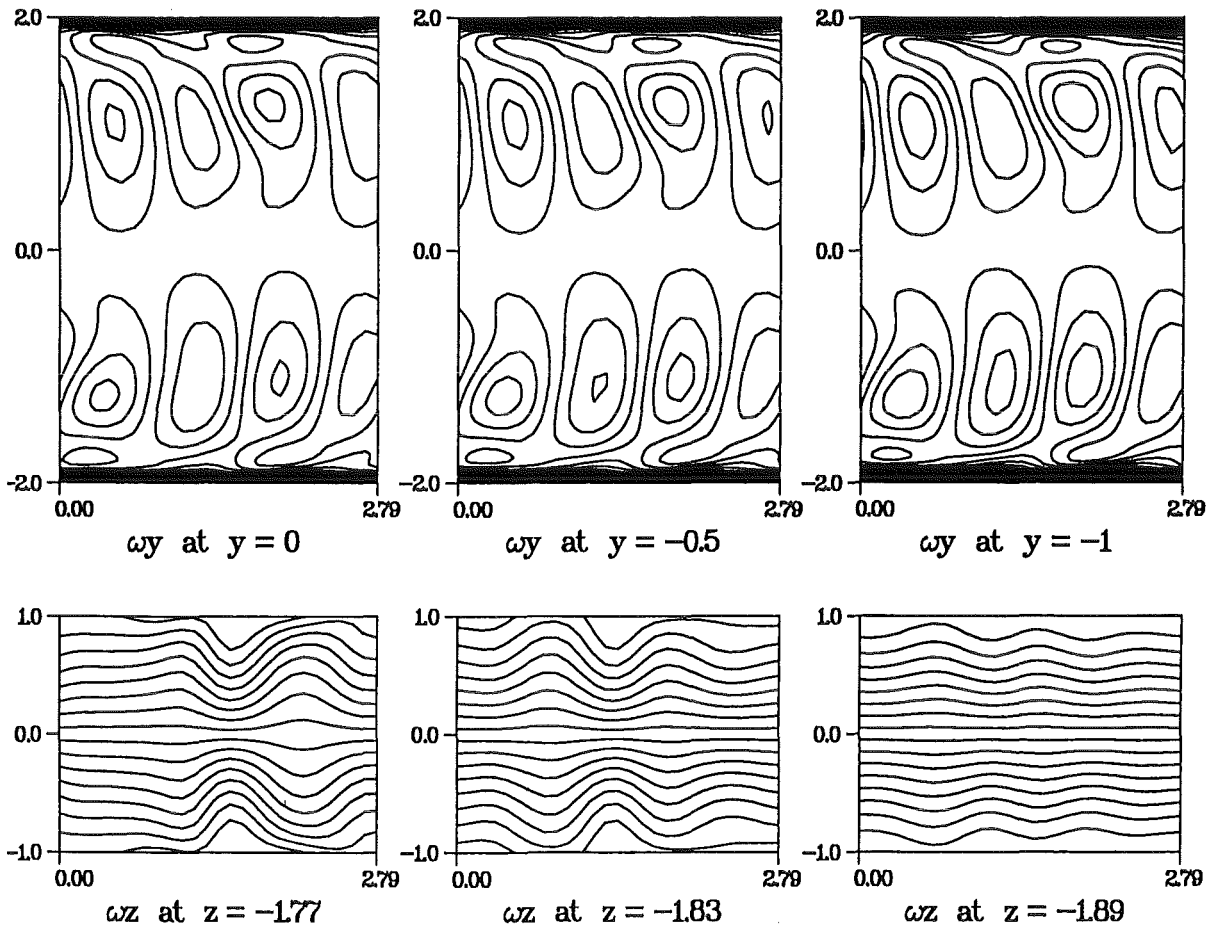
50 ωy -isolines and 18 ωz -isolines



01 SEP 1985 12:06 PM BY ATF3Z8

time = 55.0

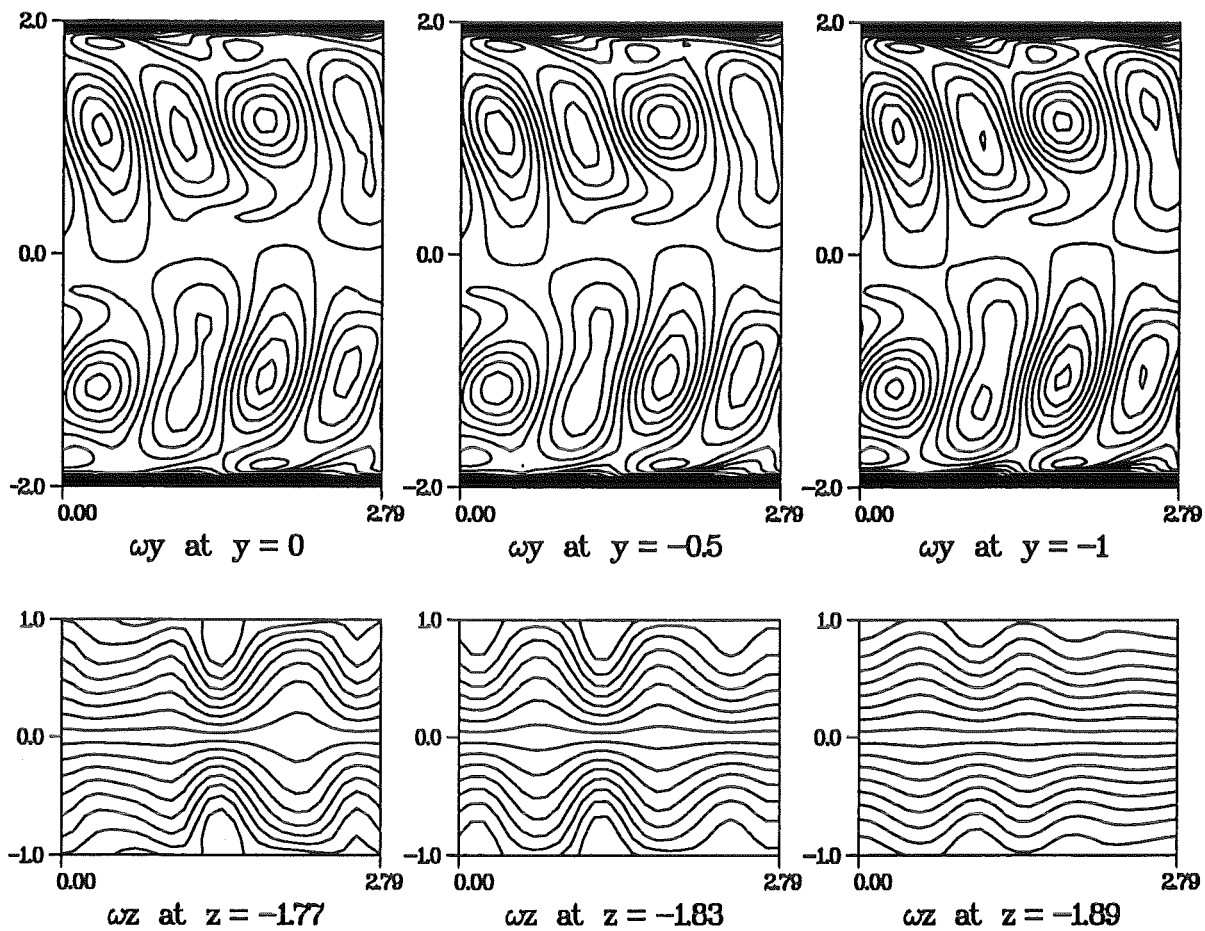
50 ωy -isolines and 18 ωz -isolines



01 SEP 1985 12:16 PM BY ATF3Z8

time = 57.5

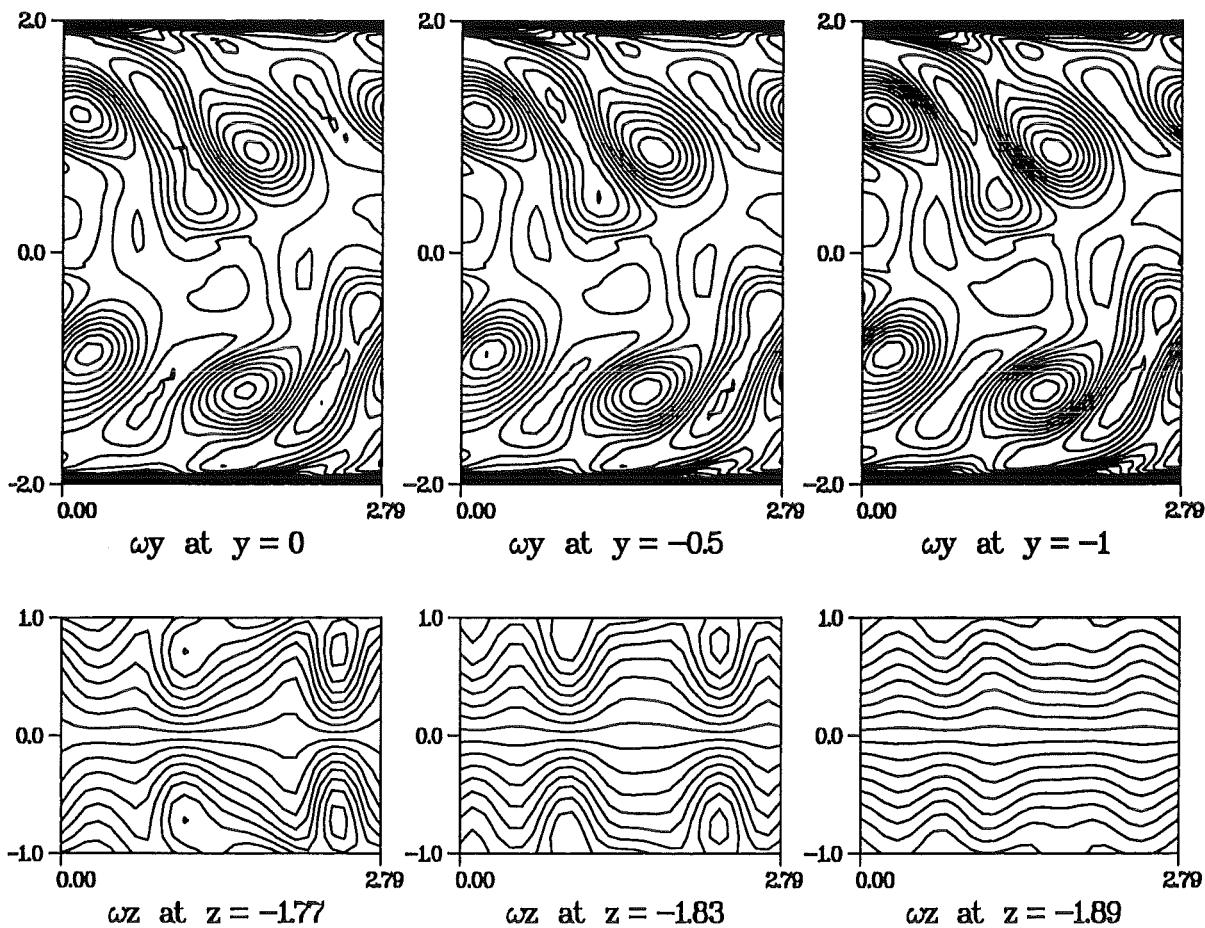
50 ωy -isolines and 18 ωz -isolines



SEP 1995 12:19 PM BY ATF328

time = 60.0

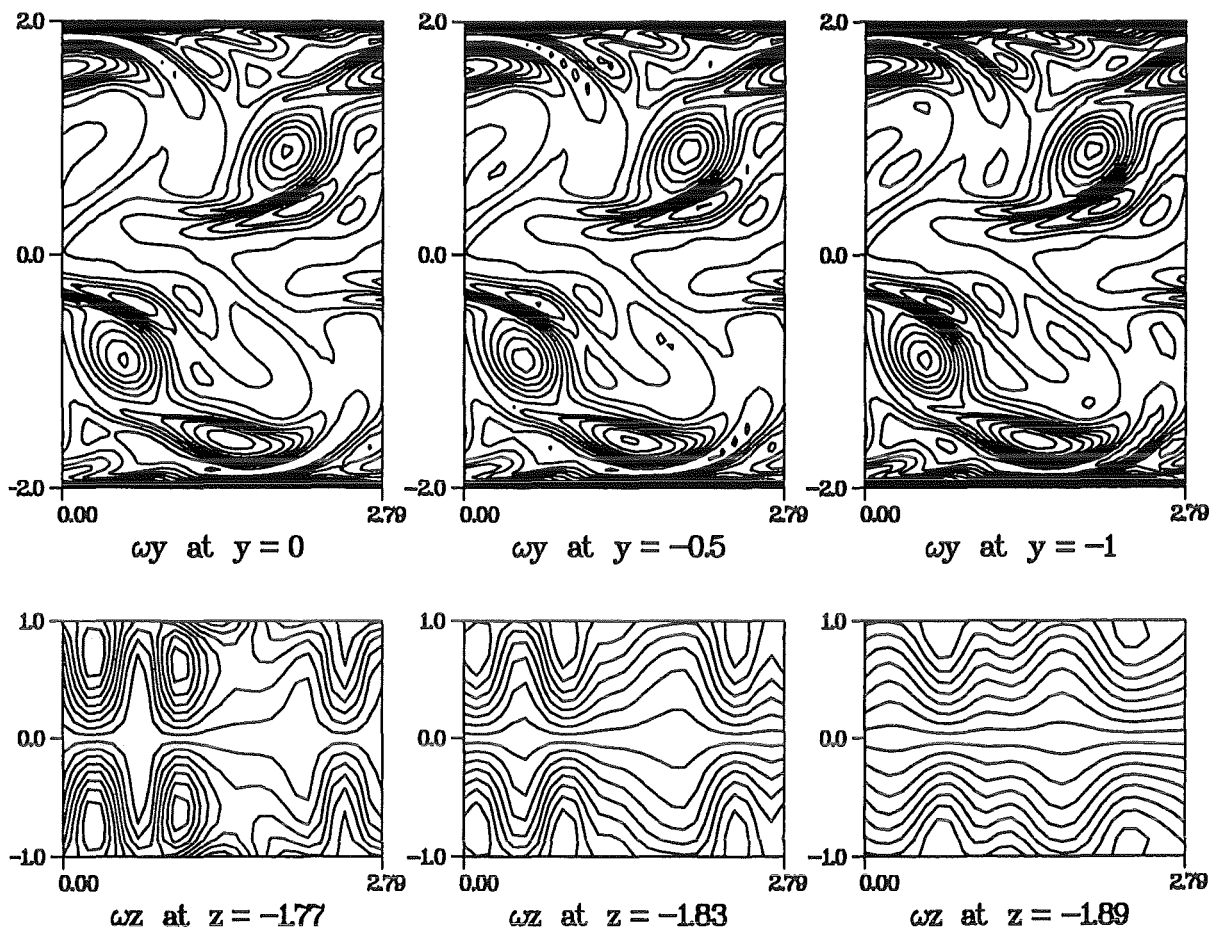
40 ωy -isolines and 18 ωz -isolines



SEP 1995 12:22 PM BY ATF328

time = 62.5

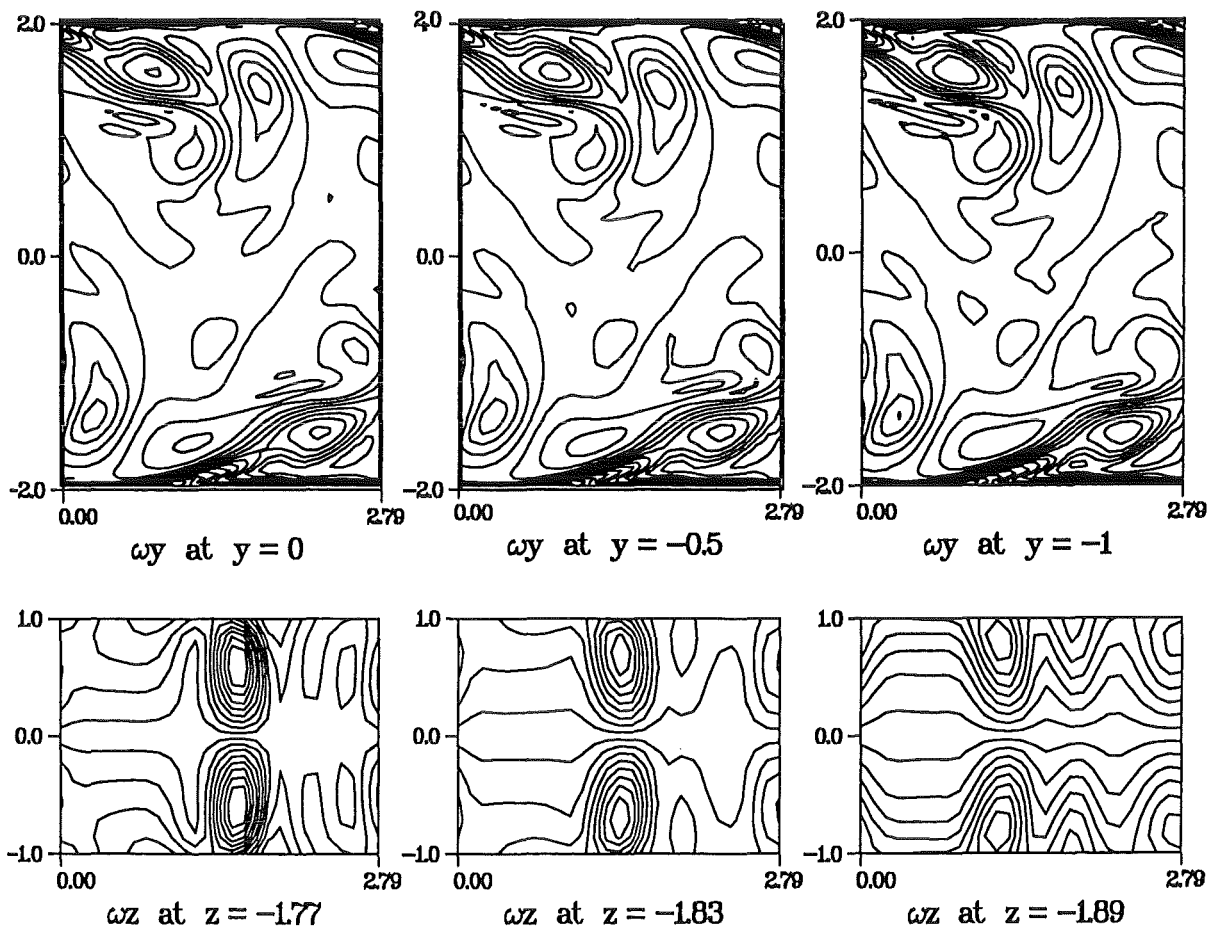
30 ωy -isolines and 18 ωz -isolines



01 SEP 1995 3:56 PM BY ATF320

time = 65.0

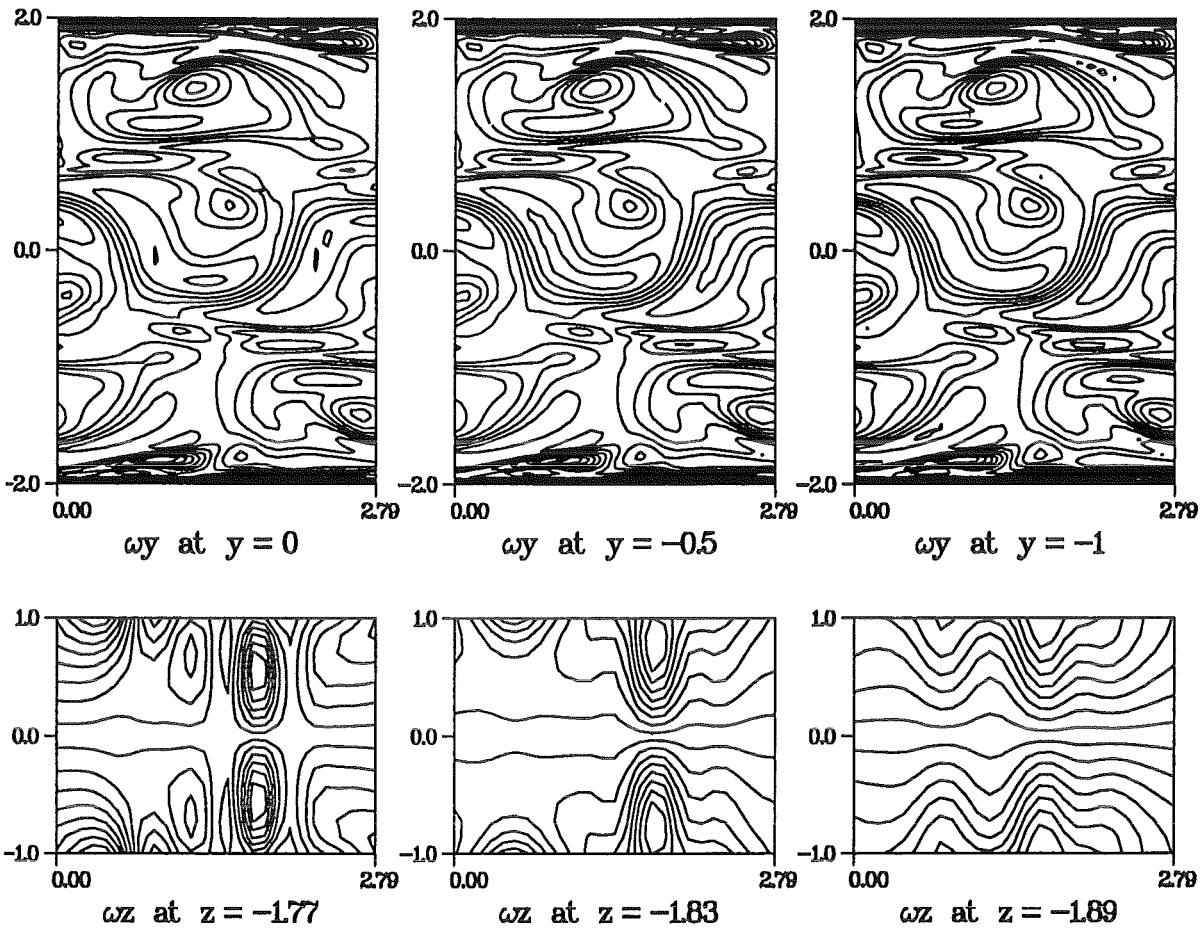
30 ωy -isolines and 18 ωz -isolines



01 SEP 1995 3:51 PM BY ATF320

time = 67.5

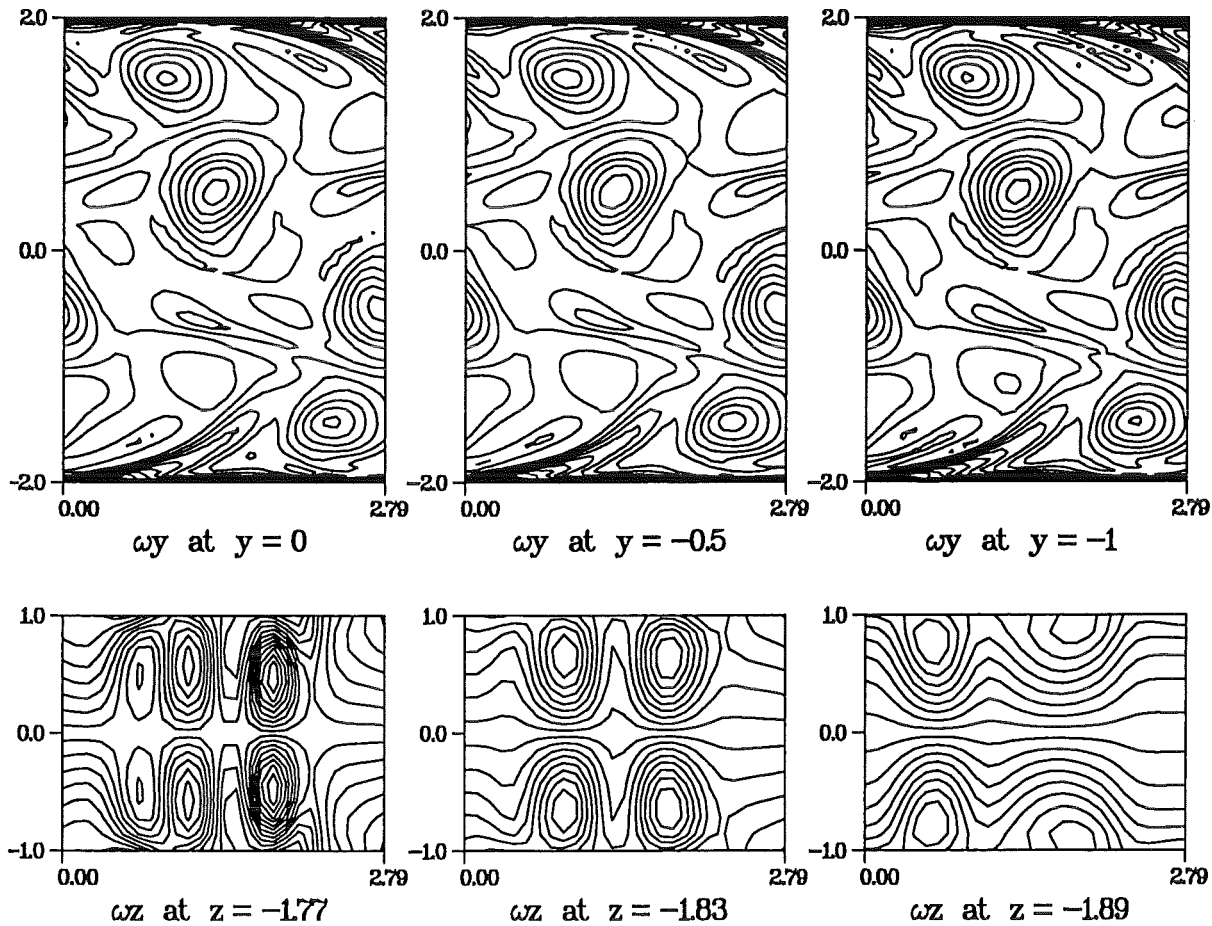
30 ωy -isolines and 18 ωz -isolines



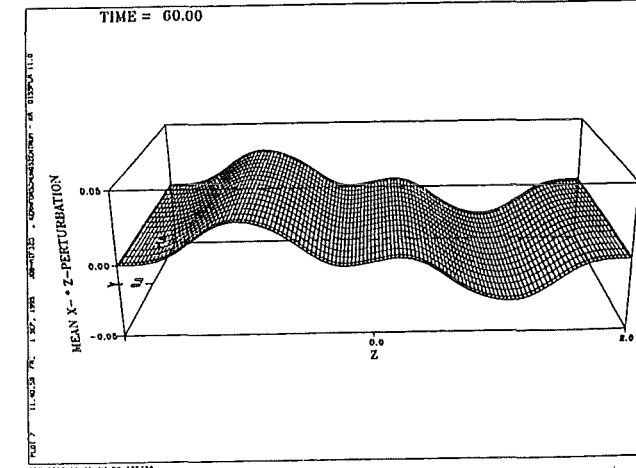
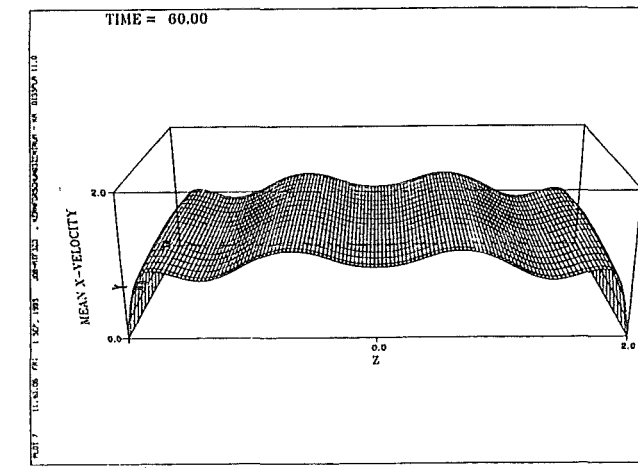
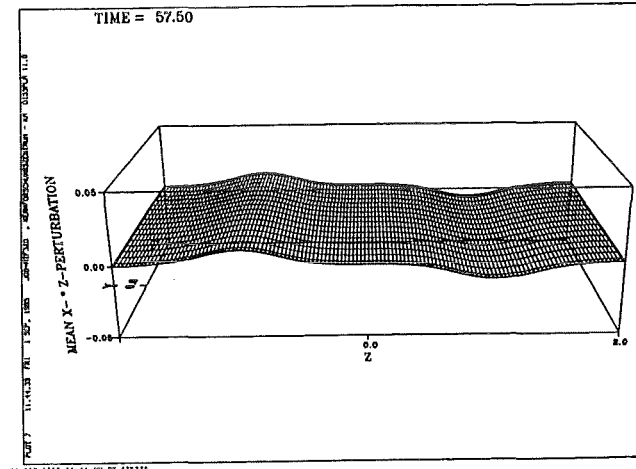
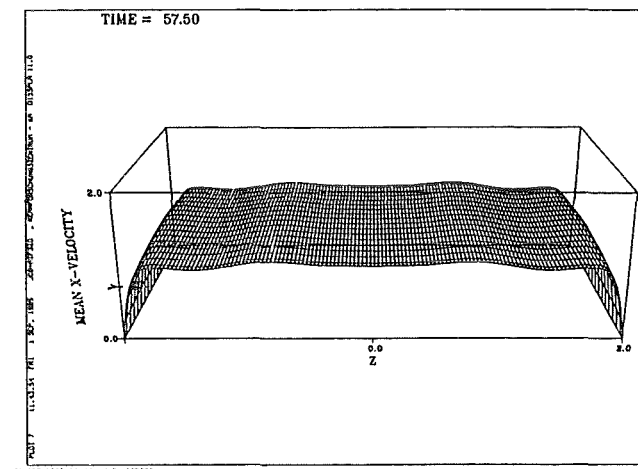
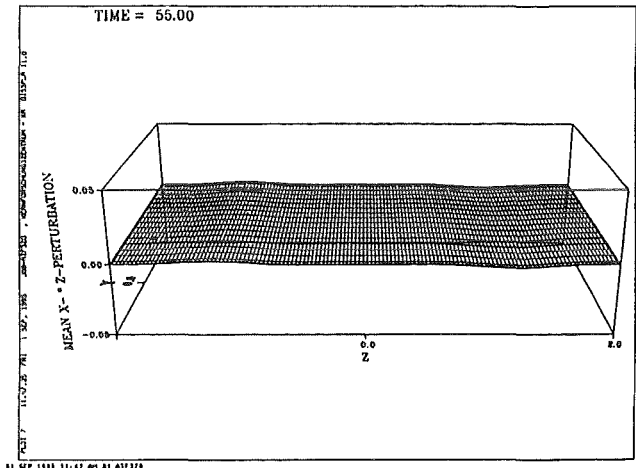
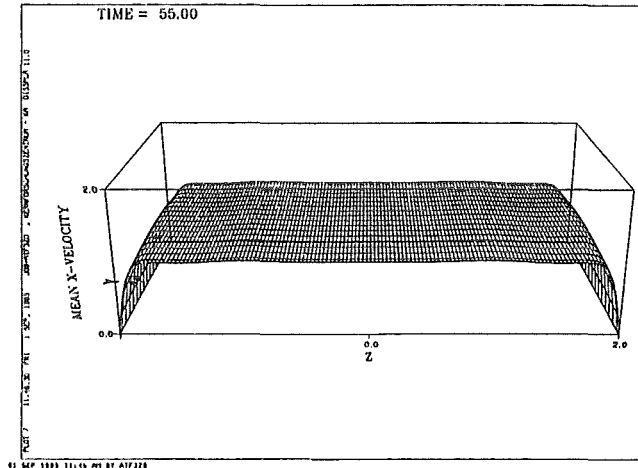
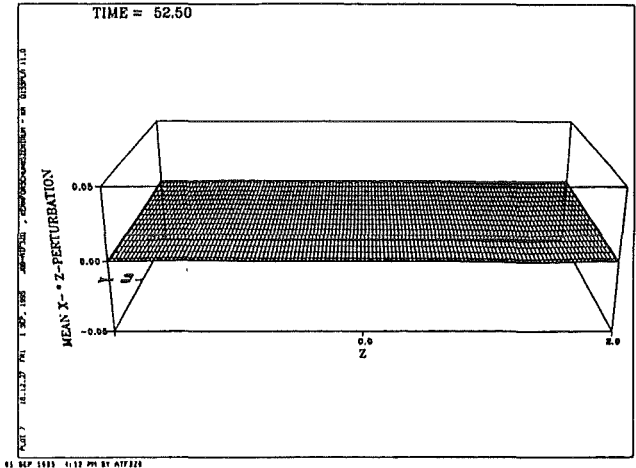
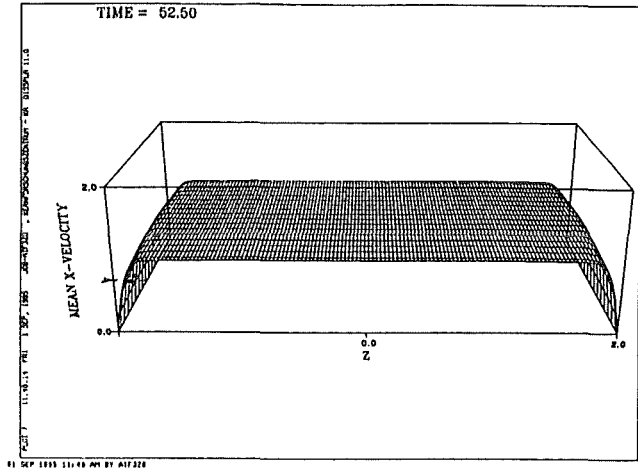
SEP 1985 3:48 PM BY ATF3ZB

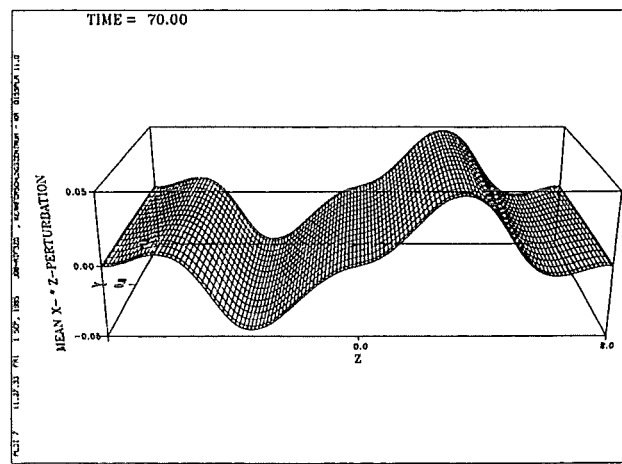
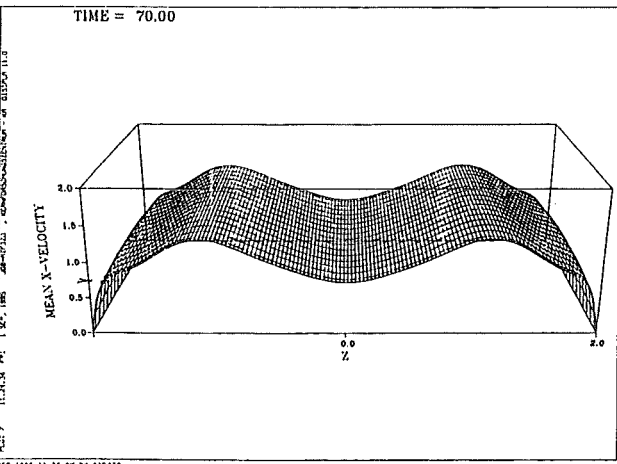
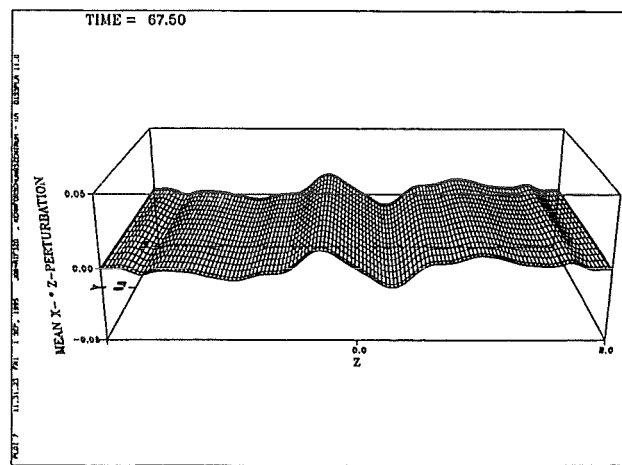
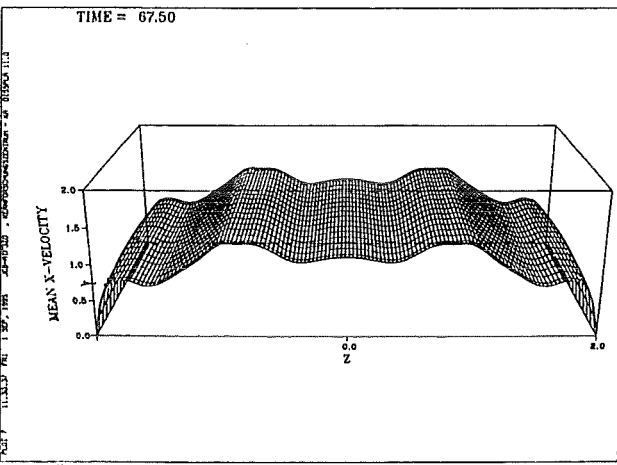
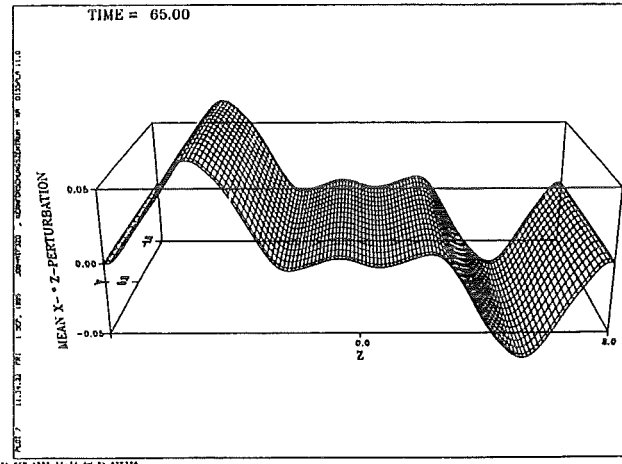
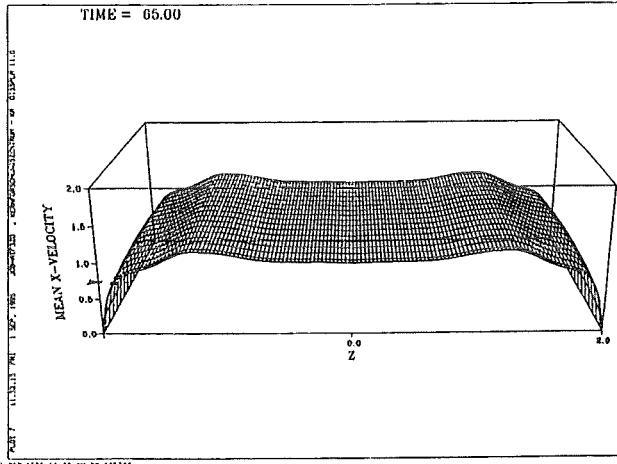
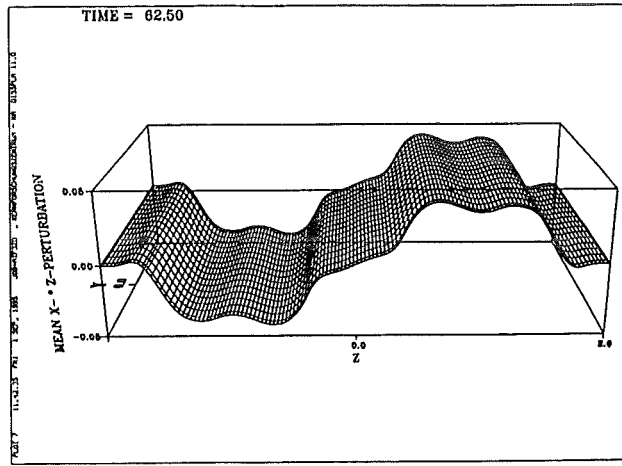
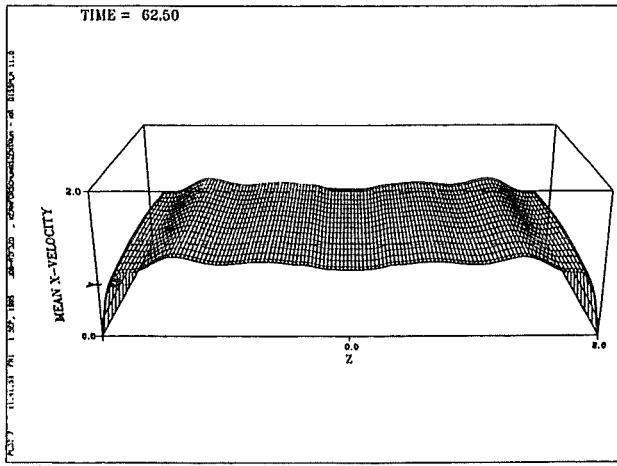
time = 70.0

30 ωy -isolines and 18 ωz -isolines



SEP 1985 11:08 AM BY ATF3ZB





5—PRACTICAL INFORMATIONS ON THE CODE

5.1—Summary of the code

Declarations & initialisations	
READ	Reading of the input parameter via 3 namelists: INPUT, INALL, INFC. ⚠ the half-width of the duct a should be equal to 1, otherwise the Hartmann number and interaction parameter would be false by a factor $1/a$.
CALL CHECK	checking compatibility of input parameter. Only in the new version of the code.
CALL INUNF	In case of restart reading of unformatted old intermediate results by the subroutine.
CALL GRID	otherwise initialisation of grid points magnetic field velocity and pressure by the subroutine.
label 1	Start of time iteration.
CALL RPOT	computation of the right hand side of the Poisson equation for electric potential.
CALL RAND	computation of the wall potential Φ_{WND} with a 2-D Poisson solver.
CALL FCYW CALL FCZW	computation of the wall potential without 2-D Poisson solver.
CALL SHIBO3	modification of this right hand side of the potential equation with respect to the boundary conditions stored in the arrays $FX0, FXM, FY0, \dots$
CALL SHAFT3	fast Poisson solver using Fourier transform, developed at the University of Karlsruhe. Solves the poisson equation for potential.
CALL DBX, NBX, DBY, ...	the boundary values of the potential are affected by these special subroutines since the SHAFT3 solver only returns the potential inside the volume and not at the boundaries.
CALL CUR	computation of the current density, once the potential is known.
CALL TVEL	affectation of the temporary velocity including all terms of the Navier-Stokes eq., pressure gradient excepted.
CALL BVXPYZ, ... CALL BCTVEL	subroutines for affectation of the boundary values of the temporary velocity. call in one statement all theses subroutines of the old version. Only in the new version of the code.
CALL RPRE	computation of the right hand side of the Poisson equation for pressure, i.e. the divergence of the temporary velocity. ⚠ The coefficient $1/N\Delta t$ of eq. (1.7) is omitted as well as the coefficient $N\Delta t$ of eq. (1.8) in subroutine FVEL.

CALL SHIBO3	modification of this right hand side of the pressure equation with respect to the boundary conditions stored again in the arrays FX0, FXM, FY0, ... that were previously used for the potential The boundary cond. include a factor $N\Delta t$ (see below) so that a restart with a different time step would produce a discontinuity at the first time step.
CALL SHAFT3	Solves the poisson equation for pressure. It returns $N\Delta t$ times the pressure instead of the actual pressure.
CALL DBX, NBX, DBY, ...	affectation of the boundary values for the electric potential with Dirichlet or Neumann boundary conditions .
CALL FVEL	computation of the final velocity as defined by eq. (1.8). ▲ The coefficient of eq. (1.8) is omitted as well as the coefficient $1/N\Delta t$ of eq. (1.7) in subroutine RPRE. It returns the actual velocity since the factor $N\Delta t$ is omitted twice: once in a division, once in a multiplication
CALL FVELBC	subroutines for affectation of the boundary values of the actual velocity.
CALL COMPAR	comparison of old and new velocity for testing the convergence of a steady expected solution.
CALL NORMV	normalisation of the velocity in order to achieve the exact Hartmann and interaction parameter defined in the input namelist.
CALL DIVV	test of the divergence of the velocity.
back to label 1	end of time iteration.
CALL OUTUNF	unformatted output of results.

5.2—Input parameters

```
/** NAMELIST INNEW
/** CYL   = WALL CONDUCTANCE RATIO AT (Y=YL)
/** CYH   = WALL CONDUCTANCE RATIO AT (Y=YH)
/** CZL   = WALL CONDUCTANCE RATIO AT (Z=ZL)
/** CZH   = WALL CONDUCTANCE RATIO AT (Z=ZH)
/** IRAND = 0 FOR PERFECTLY CONDUCTING OR INSULATING WALLS
/** IRAND = 2 FOR FINITE WALL CONDUCTIVITY
/** ISUPR = 0 FOR NO SPECIAL TREATMENT OF THE HARTMANN LAYERS
/** ISUPR = 1 FOR INTEGRAL TREATMENT OF THE HARTMANN LAYERS
/** ISYMS = 0 FOR NO SYMETRY PLANE
/** ISYMS = 1 FOR SYMETRY PLANE AT (Z=ZL=0)
/** IADBA = 0 FOR SCHEME OF FIRST ORDER IN TIME
/** IADBA = 1 FOR SECOND ORDER ADAMS-BASHFORT SCHEME
/** ICYCL = 1 FOR CYCLIC BOUNDARY COND. AT X = XL & XH. = 0 OTHERWISE
/** IJBLF = 0 ORDINARY STAGGERED GRID, AVERAGED CROSS PRODUCTS VXBXB
/** IJBLF = 1 ORDINARY STAGGERED GRID, VXBXB = -V NORMAL TO B
/** IJBLF = 2 FULLY STAGGERED GRID, VXBXB = -V NORMAL TO B
/** IMPLIC = 0 FOR EXPLICIT SCHEME FOR THE VXBXB-PART OF LORENTZ FORCE
/** IMPLIC = 1 FOR IMPLICIT SCHEME FOR THE VXBXB-PART OF LORENTZ FORCE
/** I2DIM  = 1 FOR THE CREATION OF AN OUTPUT FILE OF RESULTS AT X=CST
/** I2DIM  = 2 FOR COPYING THIS FILE OVER THE WHOLE RANGE XL<X<XH
/** I2DIM  = 0 FOR NO USE OF THIS FILE
/** ISLIP  = 1 FOR SLIP CONDITION AT Z=ZL & Z=ZH. ISLIP = 0 OTHERWISE
/** ICMHD  = 1 FOR COMPUTATION OF MHD FLOW
/** ICMHD  = 1 TO COMPUTE THE LORENTZ FORCE AND ICMHD = 0 TO CANCEL IT
/** MINUTE = MAXIMUM EXECUTION TIME
/** ISECON = MAXIMUM EXECUTION TIME
/** VXLO   = DESIRED VALUE OF VX AT Z=ZL, ONLY EFFECTIVE IF ISLIP=1
/** VXHI   = DESIRED VALUE OF VX AT Z=ZH, ONLY EFFECTIVE IF ISLIP=1
/** IPOIS  = 1 FOR A FIXED POISEUILLE-LIKE FLOW IPOIS = 0 OTHERWISE
/** TOLEL  = TOLERANCE FOR THE CONVERGENCE OF THE POTENTIAL AT THE WALLS
/** VXCURL = X-VELOCITY AT THE LOCAL VORTEX INITIAL PERTURBATION
/** VXCURL = Y-VELOCITY AT THE LOCAL VORTEX INITIAL PERTURBATION
/** VXCURL = Z-VELOCITY AT THE LOCAL VORTEX INITIAL PERTURBATION
/** IOUTP  = 1 STORE THE OUTPUT IN A DATA SET IOUTP = 0 NO OUTPUT
/** INORM  = 1 NORMALISE THE VELOCITY AT EACH TIME INORM = 1 OTHERWISE
/** IPERT  = 1 FOR AN INITIAL PERTURBATION IPERT = 0 OTHERWISE
/** COEFF  = RELAXATION COEFFICIENT FOR THE CONVERGENCE OF WALL POTENTIAL
/** ISTRIP = 1 FOR A CONDUCTING STRIP ISTRIP = 0 OTHERWISE
/** CST    = COEFFICIENT CHANGING THE PRESSURE DROP FOR CST FLOW RATE
/** A      = ASPECT RATIO: (YH-YL)/(WIDTH OF THE STRIP)
/**
/** NAMELIST INALL
/** HA     = HARTMANN NUMBER
/** ST     = STEWART NUMBER OR INTERACTION PARAMETER
/** DT     = TIME STEP
/** ALFA   = ANGLE OF MAGNETIC FIELD, INEFFECTIVE ON FULLY STAGGERED GRID
/** X0     = COEFFICIENT FOR EXPONENTIAL VARIATION OF MAGNETIC FIELD
/** TOL    = TOLERANCE (MAXIMUM DIFFERENCE BETWEEN OLD AND NEW VELOCITY)
/** IM     = NUMBER OF CELLS IN THE X-DIRECTION
/** JM     = NUMBER OF CELLS IN THE Y-DIRECTION
/** KM     = NUMBER OF CELLS IN THE Z-DIRECTION
/** MSTP   = MAXIMUM NUBER OF TIME STEPS
/** ICOMP  = COMPARISON OF OLD AND NEW VELOCITY EVERY ICOMP-TIME STEPS
/** IPRINT = PRINTING RESULTS EVERY IPRINT TIME STEPS
/** START  = 'Y' FOR A RESTART FROM THE LAST RESULTS
/** START  = 'N' FOR A COMPLETELY NEW RUN
/** INFO   = 'STRING OF 40 CHARACTERS TO BE DISPLAYED'
/**
/** NAMELIST INPUT
/** XL     = LOWER X LIMIT OF THE COMPUTING DOMAIN
/** XH     = HIGHER X LIMIT OF THE COMPUTING DOMAIN
/** YL     = LOWER Y LIMIT OF THE COMPUTING DOMAIN
/** YH     = HIGHER Y LIMIT OF THE COMPUTING DOMAIN
/** ZL     = LOWER Z LIMIT OF THE COMPUTING DOMAIN
/** ZH     = HIGHER Z LIMIT OF THE COMPUTING DOMAIN
/** ICROSS = VELOCITY NORMALISATION AT CROSS SECTION X=X(ICROSS)
/** VXWERT = INITIAL UNIFORM VALUE OF THE VELOCITY IN X-DIRECTION
/** VYWERT = INITIAL UNIFORM VALUE OF THE VELOCITY IN Y-DIRECTION
/** VZWERT = INITIAL UNIFORM VALUE OF THE VELOCITY IN Z-DIRECTION
```

5.3—Where to find & how to run the code

Old version of the code

Flow in straight ducts: the old code is located on the main frame IBM scalar computer of KfK in the data set 'ATF3Z0.TEST.FORT'. The main program is PROGRAM FLIB. The code is compiled, linked and executed by the single job card named SCJCLX on the scalar computer.

New version of the code

The new code is located in the data set 'ATF3Z0.UMHD.FORT' on the main frame IBM computer of KfK only. The code can be recompiled and linked with the job card JCC@LINK. It can be run with the job card JCGOSTEP which includes the namelists with all input parameters.

5.4—Restrictions of the new version of the code

- The new code does not allow to split the duct into pieces. It cannot use the matching parts of the old code. The domain decomposition used in the old code is not suitable for unsteady flow computation. Apart from that, it allows all the possibilities of the old code.

Some restrictions occur when using the new features of the new code.

- If the fully staggered grid is used (input parameter IJBLF set to 2), the **B**-field can only have a component in the y-direction ($B_x=B_z=0$).

References

Blair Perot, J (1992)

An Analysis of the Fractional Step Method.
Journal of Computational Physics, vol 108, pp. 51-58, 1993.

Bühler, L. (1993)

Magneto hydrodynamische Strömungen flüssiger Metalle in allgemeinen dreidimensionalen Geometrien unter der Einwirkung starker, lokal variabler Magnetfelder.
KfK-report No 5095, Kernforschungszentrum Karlsruhe, Februar 1993.

Bühler, L. (1994)

Instabilities in 2D MHD Flows
Proceeding of the 2nd international conference on Energy Transfer in MagnetoHydroDynamic Flows, September 1994, Aussois, France, pp. 463-472.

Bühler, L. (1994)

Private communication.

Debray, F. (1995)

Unpublished.

Günther, C. (1992)

Conservative versions of the Locally Exact Consistent Upwind Scheme of Second Order.
International Journal for numerical methods in Engineering, vol. 34, 3, pp 793-804

Günther, C. (1994)

Private communication.

Lenhart, L. (1994)

Magneto hydrodynamik in Rechteckgeometrien.
Volle numerische Simulation.
KfK-report No 5317, Kernforschungszentrum Karlsruhe, April 1994.

Moreau, R. (1990)

Magneto hydrodynamics
Kluwer Academic Publishers, ISBN 0-7923-0937-5.

Mößner, R. (1994)

Private communication.

Shimomura, Y. (1991)

Large eddy simulation of magneto hydrodynamic turbulent channel flows under a uniform magnetic field.
Physics of Fluids A, vol.3, No 12, pp. 3098-3106, December 1991.

Sterl, A. (1989)

Numerische Simulation magnetohydrodynamischer Flüssigmetall-Strömungen in rechteckigen Rohren bei großen Hartmann Zahlen.
KfK-report No 4504, Kernforschungszentrum Karlsruhe, January 1989.

Sterl, A. (1989)

Numerical Simulation of liquid-metal MHD flows in rectangular ducts.
Journal of Fluid Mechanics, vol. 216, pp. 161-191, 1990.